Západočeská univerzita v Plzni
Fakulta aplikovaných věd

Modelování vysokovýkonových pulzních magnetronových výbojů pro depozici vrstev

Ing. Tomáš Kozák

disertační práce
k získání akademického titulu doktor
v oboru Fyzika plazmatu a tenkých vrstev

Školitel: prof. RNDr. Jaroslav Vlček, CSc.
katedra fyziky

Plzeň 2012

University of West Bohemia
Faculty of Applied Sciences

Modelling of high-power impulse magnetron discharges for thin film deposition

Ing. Tomáš Kozák

A thesis submitted for the degree of Doctor of Philosophy in the field of Plasma Physics and Physics of Thin Films

Supervisor: Prof. RNDr. Jaroslav Vlček, CSc.
Department of Physics

Plzeň 2012

Předkládám tímto k posouzení a obhajobě disertační práci zpracovanou na Fakultě aplikovaných věd Západočeské univerzity v Plzni. Prohlašuji, že jsem předloženou práci vypracoval samostatně s použitím odborné literatury a pramenů, jejichž seznam je její součástí.

Při této příležitosti bych chtěl poděkovat svému školiteli prof. RNDr. Jaroslavu Vlčkovi, CSc. za vedení mého doktorského studia a za jeho cenné rady a podněty při zpracovávání a publikaci výsledků. Dále bych chtěl poděkovat Mgr. Andree Dagmar Pajdarové, Ph.D., která mě uvedla do problematiky modelování výbojového plazmatu a byla mi v této oblasti cenným rádcem i kritikem. Děkuji všem svým kolegům z katedry fyziky za vytvoření přátelského a motivujícího pracovního prostředí a za všechny znalosti a zkušenosti, které jsem díky nim mohl získat. Děkuji také prof. Annemie Bogaerts (University of Antwerp) a Dr. Tomáši Kubartovi (Uppsala University) za to, že mi umožnili strávit několik týdnů na jejich pracovištích. Na závěr bych chtěl poděkovat své rodině a přítelkyni Veronice za vytrvalou podporu po dobu mého studia.

V Plzni dne 26.11.2012

Contents

1 Introduction **6**

2 Status of knowledge **7**
2.1 High-power impulse magnetron sputtering 7
2.1.1 Target current waveforms 8
2.1.2 Properties of the discharge plasma 11
2.1.3 Deposition rate 15
2.2 Modelling of magnetron discharges 17
2.2.1 Plasma modelling techniques 17
2.2.2 Modelling of high-power impulse magnetron sputtering 22

3 Aims of the thesis **27**

4 Non-stationary two-zone model **28**
4.1 Model geometry and spatial approximations 29
4.2 Conservation equations 34
4.2.1 Particle transport 36
4.2.2 Plasma reactions 41
4.3 Parameters of the model 44
4.4 Implementation and numerical solution 45
4.5 Discharge and deposition characteristics 47
4.6 Material parameters for argon and copper 49

5 Results and discussion **53**
5.1 Validation of the model results for copper 53
5.1.1 Discharge current 54
5.1.2 Electron density and temperature 56
5.1.3 Conclusions 60
5.2 Effect of the target power density 61
5.2.1 Target current – voltage dependences 61
5.2.2 Densities of the sputtered material and the discharge gas particles 63
5.2.3 Discharge and deposition characteristics 66
5.2.4 Conclusions 70

5.3 Effect of the voltage pulse characteristics . . . 71
5.3.1 Constant-target-voltage pulses . . . 71
5.3.2 Stepwise-target-voltage pulses . . . 74
5.3.3 Influence of the repetition frequency . . . 77
5.3.4 Influence of the target power density in a pulse . . . 78
5.3.5 Conclusions . . . 80
5.4 Transport and ionization of the sputtered material . . . 82
5.4.1 Conclusions . . . 85

6 Conclusions 87

7 Bibliography 89
7.1 References . . . 89
7.2 Publications of the candidate . . . 98
7.3 Abstract . . . 100

1 Introduction

Modern technologies are closely related to advances in material research. Thin-film materials have become part of our everyday life. They are the functional components of microelectronic devices, solar cells or optical coatings and filters. Moreover, thin-film coatings are used in many applications to improve surface properties of bulk materials such as appearance, hardness, wear resistance, friction, wettability, oxidation resistance and chemical or biological activity.

Magnetron sputtering is one of the widely used methods for thin film deposition. Its main advantages are easy operation and up-scaling. From its introduction in the 1970s, the process has undergone several improvements which continue until today. One of the most recent developments is the high-power impulse magnetron sputtering (HiPIMS) which provides highly ionized fluxes of the deposited material which can be used for the control of microstructure, growth and purity of thin films and of deposition directionality into complex structures. The properties of the discharge, relations between the process parameters and the properties of the resulting films and the underlying physical processes related to high density magnetized plasmas have been intensively studied experimentally in recent years.

Computer simulations are used in many technological processes to calculate parameters of the process which are difficult to measure, to optimize the process or to gain a better understanding of underlying physical mechanisms. Computer simulations of magnetron sputtering discharges as well as specific phenomena related to this process have been presented in the last two decades. The recent expansion in the use of HiPIMS discharges stimulate a need for new computer simulations which would take into account the non-stationary character of these discharges and the high target power densities used.

This thesis focuses on modelling of high-power impulse magnetron sputtering discharges. The main aim is to develop a relatively simple model of HiPIMS discharges which simulates the sputtering, ionization and transport of the target material and which takes into account recent experimental findings about this process. The result is a non-stationary two-zone model which is based on preceding global plasma models of low-temperature plasma discharges and steady-state analytical models of HiPIMS. This model is used to gain better understanding of the critical processes influencing the evolution of the discharge during the pulse and the relations between the process parameters and the deposition characteristics.

This work was done at the Department of Physics of the Faculty of Applied Sciences at the University of West Bohemia as a part of the research projects MSM 4977751302 and COST OC 10045.

2 Status of knowledge

2.1 High-power impulse magnetron sputtering

High-power impulse magnetron sputtering (HiPIMS) is a recent development of a well established magnetron sputtering technique. Magnetron sputtering is a PVD process used for deposition of various coatings, including hard, wear-resistant, tribological and corrosion-resistant coatings, as well as coatings with suitable optical and electrical properties (Kelly and Arnell, 2000).

In conventional dc magnetron sputtering (DCMS), a constant target voltage is applied continuously. The typical discharge voltage, U_d, is in the range of 300 to 600 V and the typical discharge current density, J_d, reaches up to 0.1 $\mathrm{Acm^{-2}}$. The applied target power density $S_\mathrm{d} = U_\mathrm{d} J_\mathrm{d}$, ranges typically from several $\mathrm{Wcm^{-2}}$ up to about 30 $\mathrm{Wcm^{-2}}$ (Musil, 1998; Kelly and Arnell, 2000). The applied target power density is limited by the maximum allowable heat load of the target. A disadvantage of the conventional magnetron sputtering is the relatively low ion current density onto the substrate (less than 1 $\mathrm{mAcm^{-2}}$). The low energy delivered to the substrate by neutral atoms (with average energy of several eV) results in low-density films. This can be overcome by unbalanced magnetron sputtering, where the magnetic field configuration allows for higher ion currents onto the substrate, or by HiPIMS, which significantly increases the degree of ionization of the sputtered target material atoms in the flux onto the substrate.

Recent advances in the field of HiPIMS can be found in the review articles of Sarakinos et al. (2010), Anders (2011), Gudmundsson et al. (2012) and Lundin and Sarakinos (2012). Here, the most important characteristics of HiPIMS discharges will be summarized .

In HiPIMS, the target voltage is applied only during a relatively short pulse, see figure 2.1. The duty cycle $\delta = t_1/T$, where t_1 is the pulse duration and T is the pulse period, is typically up to 10 %. The average target power density in a period

$$\overline{S}_\mathrm{d} = \frac{1}{T}\int_0^T U_\mathrm{d} J_\mathrm{d} \mathrm{d}t \tag{2.1}$$

is comparable to the target power densities used in DCMS, since it is limited by the overheating of the target. However, the average target power density in a pulse

$$S_\mathrm{da} = \frac{1}{t_1}\int_0^{t_1} U_\mathrm{d} J_\mathrm{d} \mathrm{d}t \tag{2.2}$$

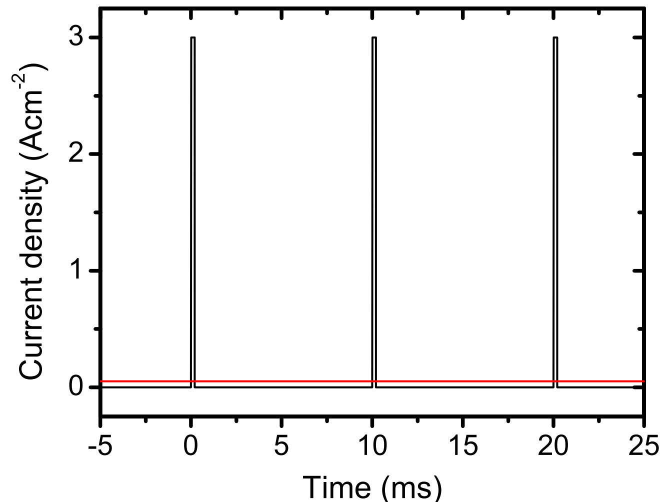

Figure 2.1: Illustration of typical direct current magnetron sputtering (red line) and high-power impulse magnetron sputtering (black line) current density waveforms. The HiPIMS discharge is represented by a peak target current of 3 Acm^{-2}, the pulse length of 200 μs and the repetition frequency of 100 Hz. The DCMS discharge is repesented by a continuous target current density of 0.05 Acm^{-2}.

is significantly higher. Assuming the target current in the pulse-off time is zero, it can be written as $S_{\mathrm{da}} \approx \delta \overline{S}_{\mathrm{d}}$. The average target power density in a pulse can reach up to several kWcm^{-2}. The typical operating voltages are in the range of 500 to 2000 V and the current densities reach up to 4 Acm^{-2}.

In comparison to DCMS, the high average target power density in a pulse leads to a significant increase in plasma density during the pulse and thus to an increase in the degree of ionization of the sputtered target material atoms. Consequently, film deposition can be carried out at highly ionized fluxes of the target material. This facilitates deposition of dense and defect-free coatings and also directional deposition into high aspect ratio trench and via structures. Moreover, the control of substrate–coating interface and the growth of films is improved.

2.1.1 Target current waveforms

The shape of the target current waveform is influenced by many process parameters, such as the target voltage, the process gas pressure, the target material, the magnetic field distribution and the geometry of the sputtering system. When the target power input into the discharge is close to the limit of the power supply, the target voltage decreases during the pulse as the capacitor banks of the power supply are discharged. Naturally, such decrease of the target voltage is a prime factor influencing the evolution of the discharge plasma. Therefore, for the studying of the plasma physics of HiPIMS, power supplies which are able to provide rectangular voltage pulses are advantageous.

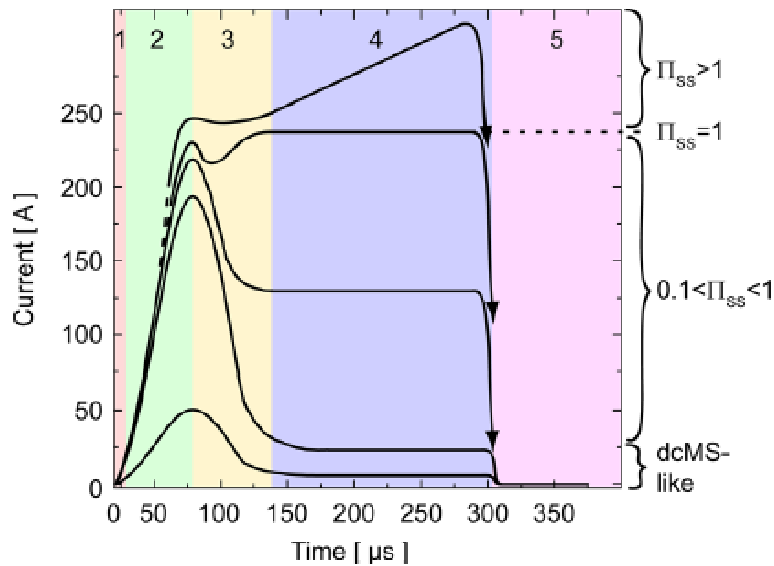

Figure 2.2: Schematic illustration of typical target current waveforms in HiPIMS discharges. The time-evolution of the target current is described in 5 phases – discharge ignition, plasma build-up, gas rarefaction, target self-sputtering, plasma decay, respectively. Taken from Gudmundsson et al. (2012).

In general, the evolution of the target current can be divided into several phases, see figure 2.2. Phase 1 corresponds to the discharge ignition. When a sufficient amount of secondary electrons is trapped in the magnetic field above the target to sustain the discharge, the target current increases (phase 2). At this point, the target current is dominated by the process gas ions. After 50 to 100 μs, the process gas atoms become depleted by the intensive ionization and by collisions with the sputtered target material atoms, the so-called *gas rarefaction* (phase 3). Simultaneously, the target material atoms fill the ionization region in front of the target. This leads to a significant change in the composition of the plasma. Indications of this were shown by optical emission spectroscopy (Ehiasarian et al., 2002; Vlček et al., 2004; Alami et al., 2006; Hala et al., 2010). The target material ions are also ionized and the target is sputtered by a mixture of process gas and target material ions (phase 4). Depending on the actual discharge conditions and the kind of the target material used, the target current can either reach a steady state with a low or a high target current or can rise unbounded until the end of the pulse. After the end of the pulse, the target current rapidly drops as the plasma species are lost through recombination and diffusion to chamber walls (phase 5).

The sputtering of the target by the ions of the same kind is called *self-sputtering*. Depending on the sputtering yield of the target material, a regime of *sustained self-sputtering* can be reached, in which the discharge can be sustained without the process gas. The necessary condition for sustained self-sputtering can be written as

$$\Pi_{\mathrm{ss}} = \beta \sigma S_{\mathrm{mm}} \geq 1\,, \tag{2.3}$$

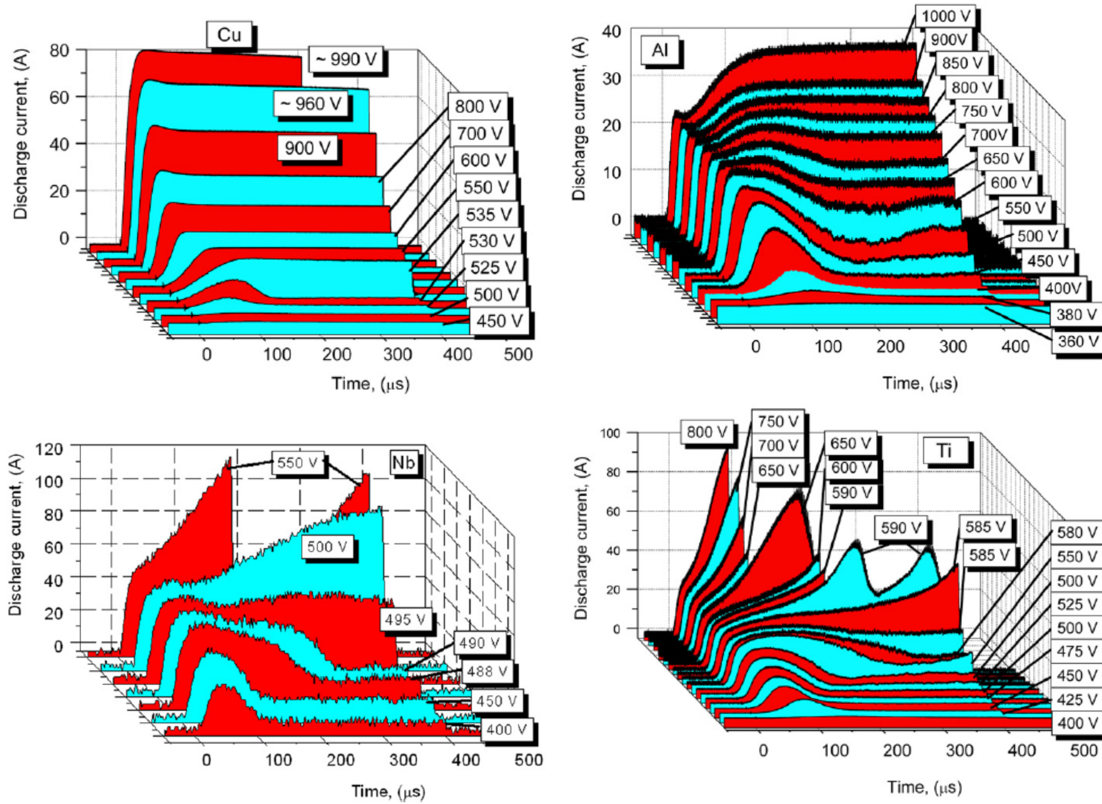

Figure 2.3: Target current waveforms for HiPIMS discharges in argon ($p = 1.8\,\mathrm{Pa}$) with various metal targets. Taken from Anders et al. (2007).

where β is the probability of ionization of the sputtered atom, σ is the probability that the generated ion returns back onto the target and S_{mm} is the sputtering yield due to the impact of the target material ion (Hosokawa et al., 1980). Anders et al. (2007) measured the voltage–current waveforms for several target materials, see figure 2.3. If $\Pi_{\mathrm{ss}} \ll 1$, we can expect the target current to drop once the process gas is rarefied. For higher target voltages, a transition to a higher target current state can occur (*self-sputtering runaway*), suggesting that $\Pi_{\mathrm{ss}} = 1$. However, the reason for the stabilization of the target current for some materials, e.g. copper, and the unbounded rise of the target current above a certain voltage threshold for other materials, e.g. titanium, is not perfectly understood yet.

A strong indication that high-target-current discharges are dominated by the target material atoms and ions can be seen in figure 2.4. There, only the initial target current peak is dependent on the argon pressure, while the steady-state target current reached after $100\,\mu\mathrm{s}$ of the pulse is practically independent of the argon pressure.

The change of plasma composition during the voltage pulse influence the secondary electron emission from the target and thus it is also very significant for the evolution of the target current. Assuming the Auger emission is the dominant process for the secondary electron emission from the target, the coefficient can be

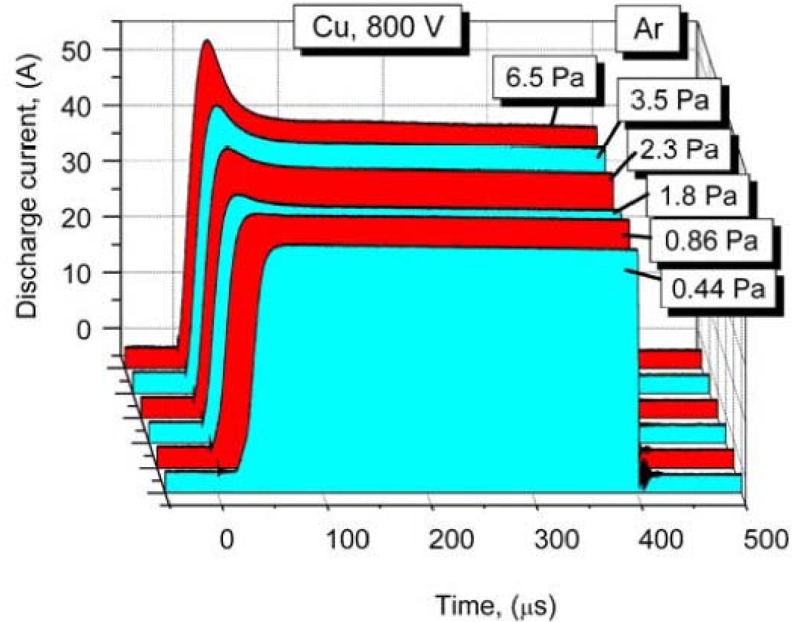

Figure 2.4: Target current waveforms for HiPIMS discharges in argon with a copper target. Taken from Anders et al. (2007).

calculated as

$$\gamma_{\mathrm{se}} \approx 0.016(\varepsilon_{\mathrm{iz}} - 2\varepsilon_{\phi}) \,, \tag{2.4}$$

where $\varepsilon_{\mathrm{iz}}$ is the ionization energy of the incident ion and ε_{ϕ} is the work function of the target material (Lieberman and Lichtenberg, 2005, eq. 9.3.4). The typical metals used as sputtering targets have the work function in the range between 4 eV and 5 eV. For argon ions, having the ionization energy of 15.82 eV, the secondary-electron emission coefficient is thus about 0.1. However, metals have the ionization energy in the range between 6.5 and 8.0 eV which yields the secondary-electron emission coefficient of zero according to (2.4). However, this is contradiction with the observed high target currents dominated by the target material ions, see figure 2.4. An increase in the secondary-electron emission coefficient can be ensured by multiply charged ions, excited singly charged ion or UV light incident on the target (Anders, 2008, 2011). However, it can be deduced that the determination of the secondary-electron emission coefficient in certain conditions is highly problematic. Anders (2011) suggests that the evolution of the secondary-electron emission coefficient during the pulse can be the cause for the stabilization of target current after the self-sputtering runaway.

2.1.2 Properties of the discharge plasma

The high target power density applied during pulses leads to a generation of a very dense plasma. It can be expected that the maximum plasma density is obtained in front of the target, where the magnetically confined secondary electrons ionize

Authors	S_{da} (Wcm^{-2})	d(mm)	n_e (m^{-3})
Gudmundsson et al. (2002)	340	90 − 170	$3 \times 10^{18} - 8 \times 10^{17}$
Gudmundsson et al. (2009)	340	80	3×10^{18}
Bohlmark et al. (2005)	510	0 − 200	$10^{19} - 10^{17}$
Pajdarová et al. (2009)	650	100	2×10^{18}
Poolcharuansin and Bradley (2010)	500	100	2×10^{18}

Table 2.1: Electron densities measured in HiPIMS discharges. Here, S_{da} is the average target power density in a pulse, d is the distance of the measuring point from the target and n_e is the maximum measured value of the electron density.

neutral atoms. The distribution of secondary-electron ionization was calculated for example by Miranda et al. (1990) or Goeckner et al. (1991). The high-plasma-density region can be seen by naked eye due to its intensive optical emission (Bradley et al., 2006).

The maximum plasma (electron) density in front of the target, n_e, can be estimated from the target current density, J_d, by the relation

$$n_e = \frac{J_d}{0.61 e u_B}\,, \tag{2.5}$$

where $u_B = \sqrt{kT_e/m_i}$ is the ion Bohm velocity (Lieberman and Lichtenberg, 2005, eq. 14.5.14). This relation neglects the electron current due to the secondary electron emission which is less than 10%. For a typical electron energy of 2 eV, the Bohm velocity is about 2000 ms^{-1}. Then, the electron density can be estimated as

$$n_e(\mathrm{m}^{-3}) \approx 5.1 \times 10^{19} J_d(\mathrm{Acm}^{-2})\,. \tag{2.6}$$

Thus, for the target current density exceeding 1 Acm^{-2}, which is often obtained in HiPIMS discharges, the corresponding maximum electron density exceeds 5×10^{19} m^{-3}.

The plasma density in the distance of several centimetres from the target can be measured by a Langmuir probe. Table 2.1 summarizes plasma densities measured experimentally by various authors. As can be seen, a typical maximum density around 10^{18} m^{-3} is achieved at the distance of 100 mm from the target. This is roughly 2 orders of magnitude higher than the typical plasma density reported for DCMS discharges.

The time-evolution of the electron temperature in HiPIMS is characterized by an initial increase to values between 2 eV and 7 eV and a decrease to much lower values below 1 eV after several tens of microseconds (Vetushka and Ehiasarian, 2008; Gudmundsson et al., 2009; Pajdarová et al., 2009), which then remains practically constant during the pulse and decreases slowly after the pulse. These low values of the electron energy can be explained by a cooling of the electrons by inelastic

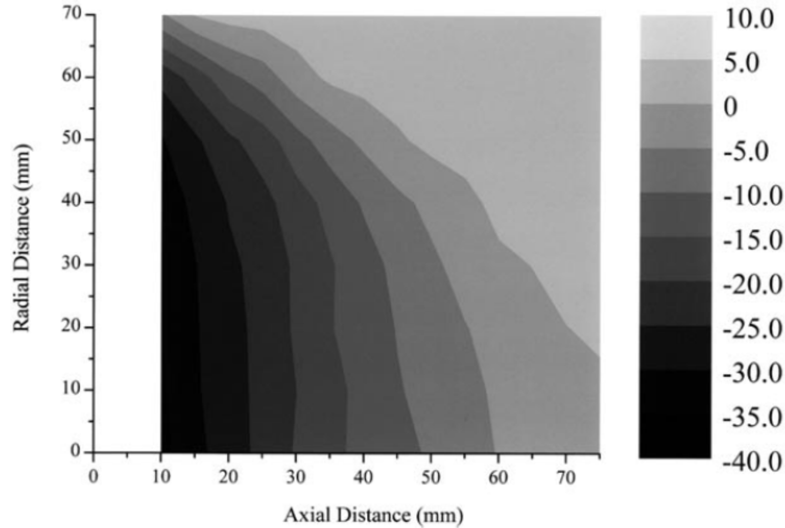

Figure 2.5: Distribution of plasma potential (V) in a typical cylindrically symmetric magnetron discharge. Taken from Bradley et al. (2001).

collisions with sputtered target material atoms, which have much lower ionization and excitations energies than the process gas.

The spatial distribution of plasma potential has been measured by an emissive probe technique (with an exception of the high-density plasma region in front of the target). First, Bradley et al. (2001) measured the plasma potential distribution in a DCMS discharge, see figure 2.5. The figure shows that a region of negative plasma potential, so called *magnetic presheath*, extends from the target sheath to a distance of several centimetres from the target, where the plasma potential becomes positive, as in a diode discharge. The potential drop over the magnetic presheath is several tens of volts. The resulting electric field pulls and guides the generated ions towards the target and, at the same time, it pushes the electrons away from the target. This potential distribution is formed as a consequence of the different mobility of electrons and ions in the magnetic field. During the pulse, the less mobile (magnetically confined) electrons must be pushed from the region of maximum plasma density to balance the flux of ions onto the target.

A similar potential distribution was obtained also by a computer simulation (Kolev and Bogaerts, 2006). Moreover, Bultinck and Bogaerts (2008) showed that a stronger magnetic field results in the formation of a potential distribution with a larger potential drop over the presheath, and thus a higher electric field. This is in perfect agreement with the above mentioned explanation.

In recent years, several authors measured the distribution of the plasma potential in HiPIMS (Mishra et al., 2010, 2011; Rauch et al., 2012). Although the potential drop over the presheath changes in time during the voltage pulse, the general shape of the potential distribution remains the same, see figure 2.6.

The energy and composition of the ionized fluxes onto the substrate has been analysed by mass spectroscopy (Bohlmark, Lattemann, Gudmundsson, Ehiasarian,

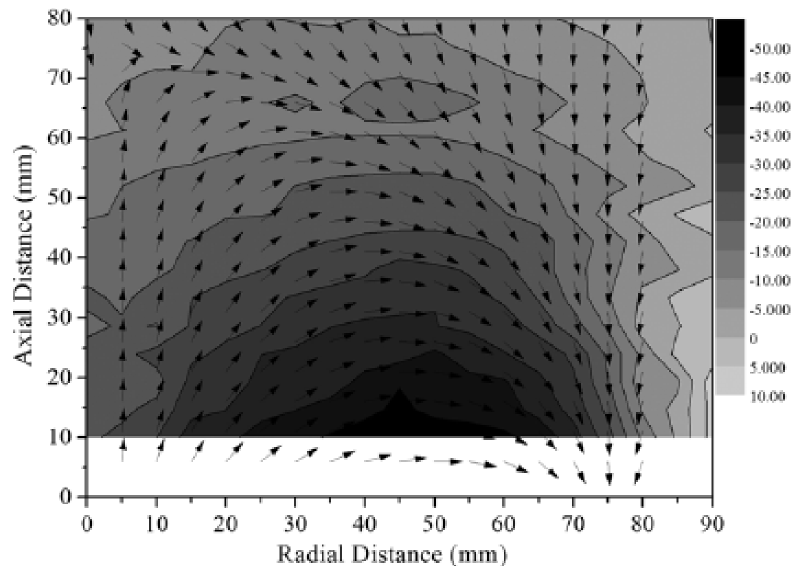

Figure 2.6: Distribution of plasma potential (V) in a cylindrically symmetric HiPIMS discharge at time of maximum target current. Taken from Mishra et al. (2011).

Gonzalvo, Brenning and Helmersson, 2006; Vlček et al., 2007a; Kudláček et al., 2008; Lazar et al., 2010; Hecimovic and Ehiasarian, 2009, 2010). A significant increase in the population of high-energy ions (energies larger than 50 eV) was observed at high target power densities. This is caused mainly by the energy distribution of the sputtered target material atoms, which is described by the Thompson energy distribution (Betz and Wien, 1994) written in a normalized form as (Lu and Kushner, 2000)

$$f(E) = \begin{cases} 2\left(1+\frac{E_\mathrm{b}}{\Lambda E_\mathrm{i}}\right)^2 \frac{E_\mathrm{b}E}{(E_\mathrm{b}+E)^3}\,, & \text{for} \quad E < \Lambda E_\mathrm{b} \\ 0\,, \quad \text{for} \quad E > \lambda E_\mathrm{b}\,, \end{cases} \tag{2.7}$$

where E_i is the kinetic energy of the incident ion, E_b is the surface binding energy of the target material, E is the kinetic energy of the sputtered atom and $\Lambda = 4M_\mathrm{i}M_\mathrm{b}/(M_\mathrm{i}+M_\mathrm{b})^2$ (where M_i and M_b are the masses of the incident ion and target material atom, respectively) is the energy transfer factor in an elastic binary collision between the incident ion and the target material atom. This energy distribution function has a maximum at $E_\mathrm{b}/2$. Due to the collisions of the sputtered target material atoms with the process gas atoms and ions, the energy of the process gas ions is also increased.

The high energy delivered into the discharge also lead to the generation of doubly charged ions of both the process gas and the target material. In the case of copper, the fraction of Cu^{2+} ions in the total ion flux onto the substrate is very low (2.0 % in the distance of 100 mm at the average target power density in a pulse of 540 $\mathrm{Wcm^{-2}}$) due to the high second ionization energy of copper (Vlček et al., 2007a). On the contrary, in the case of zirconium, the fraction of Zr^{2+} ions in the total ion flux onto the substrate in the distance of 100 mm reached 14.4 % and 21.3 % at the average

target power density in a pulse of 450 $\mathrm{Wcm^{-2}}$ and 970 $\mathrm{Wcm^{-2}}$, respectively, (Lazar et al., 2010).

Recently, plasma oscillations and density fluctuations have been observed in the high-density plasma of HiPIMS discharges. Martines et al. (2004) and Lundin, Helmersson, Kirkpatrick, Rohde and Brenning (2008) have measured oscillations of the azimuthal electric field above the target racetrack. These oscillations in the MHz range are suggested to be caused by the charge perturbations originating from the mutual movement of electrons and ions in the crossed electric and magnetic field (*modified two-stream instability*). This could explain the high mobility of electrons across the magnetic field lines (*anomalous electron transport*) which has been observed in HiPIMS discharges as well as in other magnetized plasma discharges (Rossnagel and Kaufman, 1987; Bohlmark et al., 2004; Brenning et al., 2009; Levchenko et al., 2009). The electric field fluctuations also exert a force on the ions in the direction of the $\boldsymbol{E} \times \boldsymbol{B}$ electron drift (Lundin, Larsson, Wallin, Lattemann, Brenning and Helmersson, 2008; Poolcharuansin et al., 2012). Ehiasarian et al. (2012) and Anders et al. (2012) showed plasma density fluctuations which are travelling in the direction of the $\boldsymbol{E} \times \boldsymbol{B}$ drift.

2.1.3 Deposition rate

The deposition rate, a_{D}, is an important quantity determining the film thickness deposited in a given time. It depends on two main factors: the sputtering rate of atoms from the target and the effectiveness of their transport onto the substrate. The flux of sputtered particles from the target, Γ_{st}, can be expressed as

$$\Gamma_{\mathrm{st}} = \Gamma_{\mathrm{it}} S_{\mathrm{m}} \propto J_{\mathrm{d}} U_{\mathrm{d}}^{0.5} \,, \tag{2.8}$$

where Γ_{it} is the ion flux incident onto the target and S_{m} is the effective sputtering yield, which takes into account the composition of the incident ion flux. The proportionality follows from the fact that the sputtering yield scales approximately with the square root of target voltage in the energy range from 300 to 1500 eV (Behrish and Eckstein, 2007) and the flux of ions is proportional to the target current density. Therefore, the deposition rate increases with an increasing target power density delivered into the discharge. In order to compare the efficiency of film deposition in pulsed and continuous discharges under various target power densities, it is useful to define an average *normalized deposition rate* as $\overline{a}_{\mathrm{d}}/\overline{S}_{\mathrm{d}}$, where $\overline{a}_{\mathrm{D}}$ is the average deposition rate in a period and $\overline{S}_{\mathrm{d}}$ is the average target power density in a period.

Generally, HiPIMS exhibit lower normalized deposition rates when compared to DCMS. During sputtering of copper, a decrease in the normalized deposition rate by about 50 % compared to a discharge with a DCMS-like power has been reported (Vlček et al., 2007a). During sputtering of titanium, the decrease was even more than 75 % (Vlček and Burcalová, 2010). A comparison of deposition rates between DCMS and HiPIMS dischages for several target materials has been reported by Samuelsson et al. (2010), see figure 2.7. They showed that the decrease

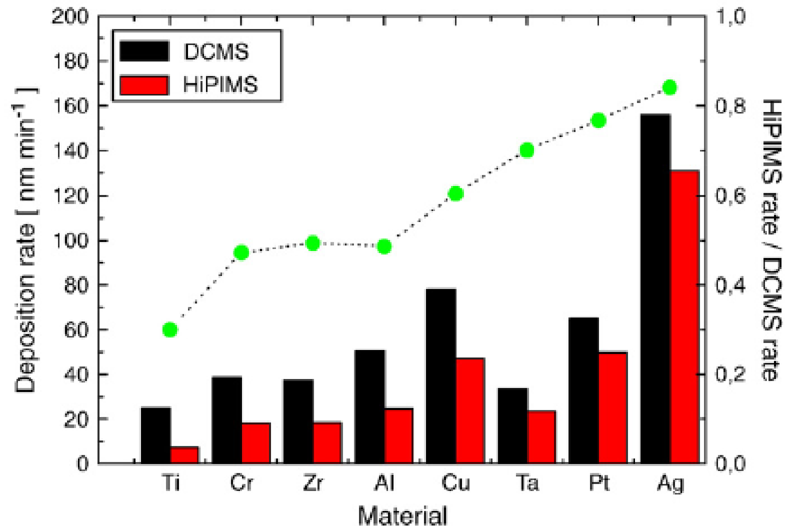

Figure 2.7: Comparison of deposition rates during direct current magnetron sputtering (DCMS) and high-power impulse magnetron sputtering (HiPIMS) of various target materials at the same average power. Taken from Samuelsson et al. (2010).

of the normalized deposition rate is a general trend which occur for all the target materials studied.

One of the reasons for the observed decrease of the normalized deposition is connected with the scaling of the sputtering yield with the target voltage. If the same target power density as in a reference DCMS is applied only during the short high-power pulse, the target voltage must be increased. As the sputtering yield is roughly proportional to $U_{\mathrm{d}}^{0.5}$, the normalized deposition rate then scales with the target voltage as $U_{\mathrm{d}}^{-0.5}$, which leads to a decrease of the normalized deposition rate with an increasing voltage.

Another important reason is the return of the target material ions back onto the target. It was mentioned before, that as the sputtered target material atoms are ionized near the target, some of them return back and contribute to the sputtering of the target. These ions are used for the sustaining of the high-power discharge and are not available for the deposition onto the substrate. This effect was quantitatively described in the models of Christie (2005) and Vlček and Burcalová (2010). It was concluded that this effect is very important since the return probability of the target material ions is high (in the range of $40 - 80\,\%$, see Vlček and Burcalová (2010), depending on the target material and discharge conditions).

Another decrease of the normalized deposition rate in HiPIMS can be related to the change of the sputtering yield (due to the change of the incident ion species or due to the change of the target sheath voltage). On the other hand, a modified magnetic field may by used to focus the target material ions onto the substrate and thus to increase the deposition rate (Bohlmark, Östbye, Lattemann, Ljungcrantz, Rosell and Helmersson, 2006; Vlček et al., 2007a). Other effects that can influence the deposition rate in HiPIMS are summarized in the paper of Anders (2010).

2.2 Modelling of magnetron discharges

With the great advance in information technology over recent years, computer modelling has become an important tool in many areas of physics. The motivation is to develop realistic models of complex technological processes that would lead to improved performance and cost reduction of the resulting products.

The modelling of low-temperature plasmas is in general less developed than computational fluid dynamics (CFD) or high temperature plasmas (Samukawa et al., 2012). In CFD, fluid equations are used to describe the macroscopic physics, where the microscopic properties enter in the form of transport and reaction coefficients. The solution of the arising set of partial differential equations is then mainly a numerical problem, though not trivial. The CFD community has now a large base of ready-to-use techniques and computer programs allowing to solve a wide area of problems. However, this is not the case for low-temperature plasmas, where the physics is more complicated. First, there is the effect of electromagnetic interaction between external fields and charged particles, but also among the charged particles leading to the so called *collective behaviour of plasma.* Moreover, the fluid approximation is not generally valid for low pressures and the kinetics of plasma particles must be resolved. There are different processes running on various time-scales, e.g., the electron plasma frequency is on the order of GHz, ion plasma frequency on the order of MHz and in the case of pulsed discharges, the power source pulsing frequency is on the order of kHz or less. Therefore, various simulation techniques must be used for different plasma species and plasma phenomena. The simulation techniques suitable for individual processes are usually developed independently with the aims to provide at least partial understanding of the overall process. The building of a complex simulation which, if to be effective, must be a combination of several modules, is a complicated task (Kushner, 2009). In the next sections the modelling techniques and the achievements made so far in magnetron modelling will be summarized, with a special section devoted to high-power impulse magnetron sputtering discharges.

2.2.1 Plasma modelling techniques

The techniques used in plasma modelling for the description of the particle dynamics can be divided into several groups based on the level of simplification.

Kinetic model

The most fundamental is the kinetic approach, where the particles of type s are described by their distribution function in phase space, $f_\mathrm{s}(t, \boldsymbol{r}, \boldsymbol{v})$. Then the evolution of the distribution function is given by the Boltzmann equation(Lieberman and Lichtenberg, 2005, sec. 2.3)

$$\frac{\partial f_\mathrm{s}}{\partial t} + \boldsymbol{v} \cdot \partial f_\mathrm{s} \boldsymbol{r} + \frac{\boldsymbol{F}_\mathrm{s}}{m_\mathrm{s}} \cdot \partial f_\mathrm{s} \boldsymbol{v} = \sum_{\mathrm{p,r}} C_\mathrm{pr}(t, \boldsymbol{r}, \boldsymbol{v})) \,, \tag{2.9}$$

where $\boldsymbol{F}_\mathrm{s}$ is the external force, m_s is the mass of the particle, C_pr is the collision integral describing the rate of change of s-type particles by collision of p-type and r-type particles.

The solution of the Boltzmann equation in this form is used for example in theory for analytical calculations of the effect of specific collisions on the transport coefficients and distribution functions of particles (Callen, 2006; Lieberman and Lichtenberg, 2005). Applications with an analytical or numerical solution of the Boltzmann equation include problems with lower dimensionality, e.g., one-dimensional studies of plasma sheaths (Vasenkov and Shizgal, 2002; Riemann, 1995) or specific symmetrical discharges (Porokhova et al., 2001). In other cases the Boltzmann equation is used to calculate the velocity distribution function of electrons in specific plasma conditions (Bretagne et al., 1981, 1982; Guerra et al., 2004; Hagelaar and Pitchford, 2005).

From the point of numerical solution, it is suitable to express the distribution function as a sum of N super-particles

$$f(t,\boldsymbol{r},\boldsymbol{v}) = \sum_{i=1}^{N} w_i \delta(\boldsymbol{r}_i - \boldsymbol{r}) \delta(\boldsymbol{v}_i - \boldsymbol{v})\,, \qquad (2.10)$$

where w_i, $\boldsymbol{r}_i$ and $\boldsymbol{v}_i$ are the weights, positions and velocities of individual super-particles, respectively. Then, all macroscopic quantities can be calculated by averaging over this set of super-particles. This approach is very straightforward, since it mimics the actual building of physics from the fundamental laws governing individual particles while the collective behaviour is obtained by means of statistical physics. Obviously, the number of super-particles is limited by our computational capacity and it is far from the real number of particles of 6×10^{23} per mole. This brings the possibility of numerical errors resulting from the particle discretization which must be carefully watched (Birdsall and Langdon, 1991). On the other hand, in many cases only a few thousand test particles are enough for a representation of the distribution function with a suitable accuracy. The simulation of the time-evolution of the Boltzmann equation is then usually done in two steps which separate the transport (left hand side of (2.9)) and the collisional processes (right hand side of (2.9)). This is possible if the time of interaction in collisions is much smaller than the time between two successive collisions which is true in low-pressure plasmas. During the transport step the equations of motion

$$\frac{\mathrm{d}\boldsymbol{r}_i}{\mathrm{d}t} = \boldsymbol{v}_i\,, \qquad \frac{\mathrm{d}\boldsymbol{v}_i}{\mathrm{d}t} = \frac{\boldsymbol{F}_i}{m} \qquad (2.11)$$

are solved for each particle. Then the properties of particle collisions are determined by the Monte Carlo method based on the target particle densities and interaction cross section and the effect of collisions is applied to the particle velocities. The cycle of transport and collision steps is repeated until the end of the simulation.

The advantages of this particle approach is that it is algorithmically simple, it can be easily implemented in three dimensions and it is easily parallelizable. However,

this method becomes very time-demanding when a large number of particles must be tracked simultaneously, for instance in self-consistent simulations of large volumes.

The kinetic method was used frequently for simulations of high-energy secondary-electron trajectories and collisions in the magnetic trap above the magnetron target (Miranda et al., 1990; Sheridan et al., 1990) and for simulations of the transport of sputtered target material atoms (Petrov et al., 1999; Kadlec, 2007; Sobbia et al., 2008). In these papers, the electrostatic field is assumed constant and must be given as an input. Such simulations are therefore not self-consistent. On the other hand, the well-known particle-in-cell (PIC) method is a kinetic (particle) simulation algorithm where a large number of particles is advanced simultaneously in time so that after each time-step the electric field in the whole simulation region can be calculated self-consistently from the charge distribution in space. This makes it the most realistic method for low-pressure low-temperature discharges so far. PIC simulations of magnetron discharges were published in the works of Kondo and Nanbu (1999) and Kolev and Bogaerts (2006). Other papers about PIC simulations of low-temperature plasmas include RF discharges (Longo, 2000; Matyash et al., 2007) or cylindrical magnetrons (van der Straaten et al., 1998). However, due to the coupling of charged particles and the electric field, several numerical stability conditions must be fulfilled: the time step, Δt, is constrained by the relation $\Delta t \omega_{\mathrm{pe}} \ll 1$ and the cell dimension Δz is constrained by the relation $\Delta z \leq \lambda_{\mathrm{D}}$, where ω_{pe} is the electron plasma frequency and λ_{D} is the Debye length (Birdsall and Langdon, 1991; Kolev, 2007). These conditions become significant constraints for the applicability of this method to high-density plasma conditions. In the above mentioned references, magnetron discharges were simulated for the maximum time of several tens of microseconds and with the maximum plasma density on the order of $10^{17}\,\mathrm{m}^{-3}$.

Fluid model

A fluid model represents a macroscopic description of the simulated system in terms of statistical physics. Rather than looking at the trajectories of individual particles, it may be sufficient and much faster to describe only the macroscopic transport of the fluid which results from the collective behaviour of many particles. The fluid model approach is strictly speaking valid only for sufficiently low value of the Knudsen number (Kolev, 2007)

$$\mathrm{Kn} = \frac{\lambda}{L} < 0.01, \qquad (2.12)$$

where λ is the particles mean free path and L is the characteristics length scale of the system. This condition ensures that the collisions between particles are sufficiently frequent to cause local relaxation of the velocity distribution function towards equilibrium. Then the velocity distribution function can be characterized by

its moments, i.e. density, flux and energy density,

$$n_s(t, \boldsymbol{r}) = \int f_s(t, \boldsymbol{r}, \boldsymbol{v}) d^3v \,, \tag{2.13}$$

$$\Gamma_s(t, \boldsymbol{r}) = n_s \boldsymbol{u}_s = \int \boldsymbol{v} f_s(t, \boldsymbol{r}, \boldsymbol{v}) d^3v \,, \tag{2.14}$$

$$\varepsilon_s(t, \boldsymbol{r}) = \frac{1}{2} m_s \int v^2 f_s(t, \boldsymbol{r}, \boldsymbol{v}) d^3v \,, \tag{2.15}$$

respectively, where $\boldsymbol{u}_s$ is the mean velocity (Lieberman and Lichtenberg, 2005, sec. 2.3).

The velocity moments of the Boltzmann equation (2.9) lead to the well-known conservation equations of particles, momentum and energy. The particle conservation equation can be written in the form

$$\frac{dn_s}{dt} + \nabla \cdot (n \boldsymbol{u}_s) = \sum_{pr} R_{pr} \,, \tag{2.16}$$

where R is the particle generation and loss rates due to collisions. They can be expressed as

$$R_{pr} = \pm n_p n_r K_{pr} = \pm n_p n_r \int_{pr} \int_{\Omega} f_p(\boldsymbol{v}) f_r(\boldsymbol{w}) |\boldsymbol{v} - \boldsymbol{w}| \, I(\Omega, |\boldsymbol{v} - \boldsymbol{w}|) d\Omega d^3v d^3w \,, \tag{2.17}$$

where K_{pr} is the collision rate integral depending only on the velocity distribution functions of the colliding species, f_p and f_r, and the cross section for the collision, I, depending on the scattering angle Ω and the relative particle velocity before collision, $|\boldsymbol{v} - \boldsymbol{w}|$. Since the velocity distribution functions are assumed constant in a fluid model, K_{pr} is also constant and thus it is called a *collision rate constant.*

The momentum conservation equation takes the form

$$m_s n_s \left[\frac{\partial \boldsymbol{u}_s}{\partial t} + (\boldsymbol{u}_s \cdot \nabla) \boldsymbol{u}_s \right] = n_s \boldsymbol{F}_s - \nabla p + \boldsymbol{f}_c \,, \tag{2.18}$$

where $p = n_s k T_s$ is the pressure, k is Boltzmann constant, T_s is the temperature of the particles and $\boldsymbol{f}_c$ is the rate of momentum transfer per unit volume due to collisions with other species.

Finally, the energy conservation equation can be written in the form

$$\frac{d}{dt} \left(\frac{3}{2} p_s \right) + \nabla \cdot \frac{3}{2} (p_s \boldsymbol{u}_s) + p \nabla \cdot \boldsymbol{u}_s + \nabla \cdot \boldsymbol{q} = n_s \boldsymbol{u}_s \cdot \boldsymbol{F}_s + \frac{d}{dt} \left(\frac{3}{2} p_s \right) \bigg|_c \,, \tag{2.19}$$

where $\boldsymbol{q}$ is the heat flow, the first right-hand-side term is the power input by the external force and the second right-hand-side term accounts for all collisions that change the energy density.

The implementation of a fluid model is not as straightforward as that of a kinetic particle model. The set of partial differential equations must be discretized

on a mesh filling the simulation region. The details of the discretization and the coupling between the equations of different species and the electromagnetic field has a significant effect on the stability and accuracy of the resulting solution algorithm.

Compared to the kinetic particle model, the degrees of freedom are significantly reduced which results in a much faster solution. However, as mentioned at the beginning of this section, the correctness of the transport terms of the fluid model in low-pressure discharges should be a concern.

Costin et al. (2005) made a fully fluid model of a magnetron discharge. They used a special algorithm which decomposes the electron flux term into a classical drift-diffusion part and a contribution of the drift across the magnetic field. Another approach is to use the fluid model only for certain plasma species as a part of a hybrid model. A suitable compromise is to combine a particle model for fast electrons with a fluid model for ions and slow electrons, as was done by Shidoji et al. (1999) and Kolev and Bogaerts (2004). In the latter work, it was mentioned that for high magnetic field strengths ($B_{\mathrm{max}} > 400\,\mathrm{G}$) the electric plasma potential becomes unrealistically negative. This is related to the limitation of the description of transport of electrons across magnetic field lines by classical diffusion. Shidoji and Makabe (2003) simulated all electrons as particles and they used the fluid model only for unmagnetized ions.

Global model

A global model is a further simplification of the fluid model. While the fluid model equations are local conservation laws, in a global model, the conservation equations are applied to a macroscopic volume. Integrating the particle conservation equation (2.16) over a volume V leads to

$$\frac{\mathrm{d}}{\mathrm{d}t}\int_V n_{\mathrm{s}}\mathrm{d}\boldsymbol{x} + \int_{\partial V} n_{\mathrm{s}}\boldsymbol{u}_{\mathrm{s}}\cdot\hat{\boldsymbol{n}}\mathrm{d}\boldsymbol{x} = \sum_{\mathrm{pr}}\int_V R_{\mathrm{pr}}\mathrm{d}\boldsymbol{x}\,, \tag{2.20}$$

where $\hat{\boldsymbol{n}}$ is the outer normal of the boundary surface of volume V. The integrals represent the total number of particles in the volume, the total flux of particles across the volume boundary and the total number of particles generated or lost during collisions, respectively. Therefore, by using a global model, the information about spatial dependence of particle densities inside the simulation volume is lost. Only the time-evolution of total number of particles in the volume is calculated. In order to calculate the fluxes of particles across the boundaries which depend on the particle density at the volume boundary, the distribution of the particle density must be specified. The particle density is assumed to be decomposable as $n_{\mathrm{s}}(t,\boldsymbol{x}) = n_{\mathrm{s}}(t)\tilde{n}_{\mathrm{s}}(\boldsymbol{x})$, where $\tilde{n}_{\mathrm{s}}(\boldsymbol{x})$ represents a fixed spatial distribution part and $n_{\mathrm{s}}(t)$ represents the time-dependent magnitude part. Then the integrals of the fixed spatial distribution part can be calculated and the resulting equation becomes an ordinary differential equation for the time-dependent magnitude of the particle density in the simulated volume.

Particle velocities must be specified at the volume boundaries to calculate the flux $\mathbf{\Gamma}_\mathrm{s}$. Since the volume boundaries usually correspond to physical boundaries of the simulated system, the particle velocities are defined by the boundary conditions, so the momentum conservation equation is not necessary.

Similarly to the particle conservation equation, the global energy conservation equation can be written in the form

$$\frac{\mathrm{d}}{\mathrm{d}t}\int_V \frac{3}{2}p_\mathrm{s}\mathrm{d}\boldsymbol{x} + \int_{\partial V}\frac{3}{2}p_\mathrm{s}\boldsymbol{u}_\mathrm{s}\cdot\hat{\boldsymbol{n}}\mathrm{d}\boldsymbol{x} = \int_V \mathbf{\Gamma}_\mathrm{s}\cdot\boldsymbol{F}_\mathrm{s}\mathrm{d}\boldsymbol{x} + \sum_\mathrm{pr}\int_V R_\mathrm{pr}^\mathrm{en}\mathrm{d}\boldsymbol{x}\,, \tag{2.21}$$

where $R_\mathrm{pr}^\mathrm{en}$ is the rate of energy density change due to particle collisions. The third and fourth term of (2.19), representing the heating due to fluid volume change and microscopic heat transfer, respectively, were neglected. The second term in (2.21) represents the total macroscopic flux of energy across the volume boundaries.

The main advantage of global models is their mathematical simplicity resulting in a very short computational time, compared to fluid and kinetic models. The time-evolution of particle densities can be calculated over the time-scales on the order of seconds. This approach is beneficial to determine the composition of reactive plasmas with many possible reaction species (Hjartarson et al., 2010; Thorsteinsson and Gudmundsson, 2010). A time-dependent global model of argon plasma was presented by Ashida et al. (1995). Hollow cathode discharge models with the inclusion of the sputtered atoms were presented by Warner et al. (1979) and Lichtenberg and Lieberman (2000). Kim et al. (2006) published a global model for an electronegative oxygen discharge. The above mentioned papers deal either with a hollow cathode discharge or a RF discharge, whose advantage is that the plasma is distributed symmetrically in a cylindrical vacuum chamber. Therefore it can be easily described by a global model. To my best knowledge, there was no attempt to use a global model to simulate a magnetron discharge, where the effect of the magnetic field would be included.

However, also other models, usually called *analytical*, should be mentioned in this section. They are in fact close to global models, because the unifying mathematical description of physical processes are the basic conservation equations. Buyle et al. (2004) presented a simplified model of a magnetron discharge, where the distribution of secondary electrons in front of the target is built from arches representing trajectories of individual electrons along the magnetic field lines. The transport of secondary electrons in the magnetic field is described algebraically which allows much faster calculation of their ionization distribution than in the case of a Monte Carlo particle simulation. This model makes it possible to calculate the current–voltage characteristics of a magnetron discharge.

2.2.2 Modelling of high-power impulse magnetron sputtering

There are two main difficulties in the simulation of high-power impulse magnetron sputtering discharges when compared to conventional magnetron discharges: the

high plasma densities reached and the very long times that have to be calculated. The classical explicit PIC method cannot be used to simulate HiPIMS discharges due to the stability restrictions mentioned in section 2.2.1. A hybrid model must be used in order to calculate the discharge effectively.

Due to the complexity of the process, only several global and analytic models of HiPIMS or non-self-consistent models focusing on specific processes related to HiPIMS have been published until today. Christie (2005) presented a *target material pathways model*. This is a global model describing the possible processes influencing the transport of sputtered target material atoms in the discharge. The processes of ionization of the sputtered target material atoms, their return onto the target and their losses to chamber walls are described by probabilistic parameters . This model explains the observed decrease in the normalized deposition rate, when compared to DCMS, by the return of target material ions onto the target.

Vlček and Burcalová (2010) presented a steady-state phenomenological model for high-power dc magnetron sputtering (figure 2.8), based on that developed by Christie (2005). The original model was modified and supplemented by a balance equation for secondary electrons leaving the target surface. This makes it possible to evaluate the fraction of ionized sputtered atoms directed back to the target, which act, together with process gas ions, to sustain the magnetron discharge under various experimental conditions. These authors derived the formulas for $a_{\mathrm{D}}/S_{\mathrm{d}}$ and the ionized fraction of the target material atoms in the flux onto the substrate, Θ, in a steady-state high-power magnetron sputtering discharge as functions of the magnetron voltage, U_{d}, the fraction of target material ions in the total ion flux onto the target, m_{t}, the relative ion-to-atom transport factor, $\xi_{\mathrm{i}}/\xi_{\mathrm{n}}$, describing the relative losses of target material ions and neutrals to chamber walls during their transfer to the substrate, and the probability of additional ionization of sputtered atoms, γ, in the plasma bulk, from where the arising ions are not directed back to the target.

For $a_{\mathrm{D}}/S_{\mathrm{d}}$, they obtained

$$\frac{a_{\mathrm{D}}}{S_{\mathrm{d}}} = k\alpha(U_{\mathrm{d}})\frac{U_{\mathrm{d}}^{-0.5}}{1+\gamma_{\mathrm{ef}}}\,, \tag{2.22}$$

where k is a constant under the assumption that the mass density of deposited films and the probability for the sputtered atoms to reach the substrate do not change for a magnetron sputtering system of the given geometry and the magnetic field configuration in the range of U_{d}, and hence S_{d}, investigated at the same argon pressure; $\alpha(U_{\mathrm{d}})$ is the normalized rate coefficient referring the transfer of sputtered target material atoms and ions to the substrate for a high-power dc magnetron sputtering to the transfer of the sputtered atoms for a hypothetical conventional dc sputtering at the same magnetron voltage U_{d} and no ionization of the sputtered atoms; γ_{ef} is the effective secondary electron emission coefficient of the target material. The normalized rate coefficient $\alpha(U_{\mathrm{d}})$ is given by the relation

$$\alpha(U_{\mathrm{d}}) = \frac{S_{\mathrm{m}}}{S_{\mathrm{mg}}}\left[(1-\beta)\Big(1-\gamma+\gamma\frac{\xi_{\mathrm{i}}}{\xi_{\mathrm{n}}}\Big)+\beta(1-\sigma)\frac{\xi_{\mathrm{i}}}{\xi_{\mathrm{n}}}\right], \tag{2.23}$$

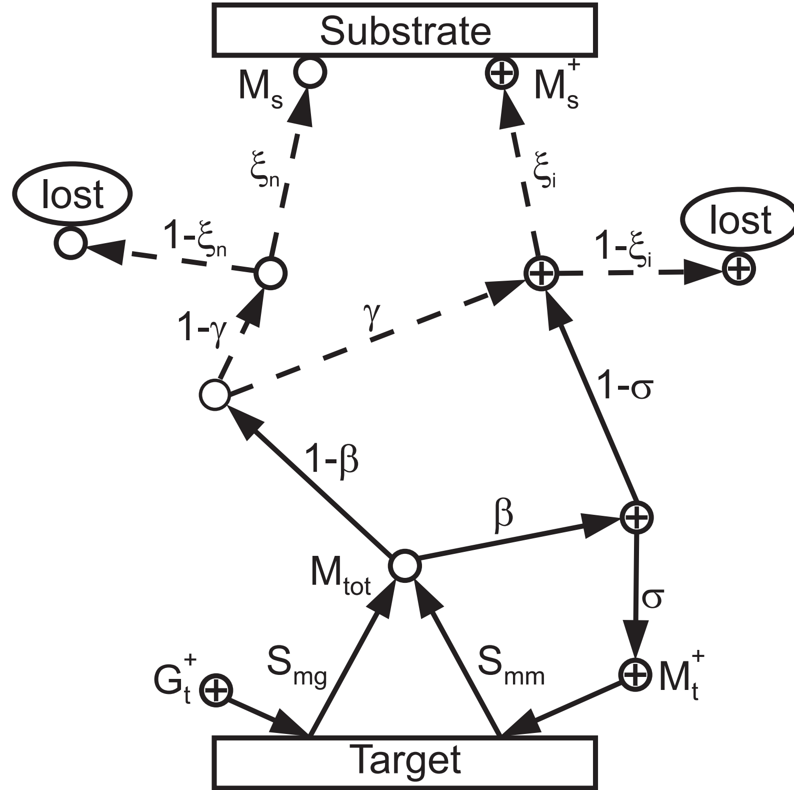

Figure 2.8: Schematic illustration of the steady-state phenomenological model (Vlček and Burcalová, 2010). Here, G_{t}^{+} and M_{t}^{+} are the total fluxes of the process gas and target material ions incident on the target, respectively; S_{mg} and S_{mm} are the process gas-ion and self-sputtering yields of the target material, respectively; M_{tot} is the total flux of target material atoms sputtered from the target; β is the probability of ionization of sputtered atoms in front of the target; σ is the probability of return of ionized sputtered atoms to the target; γ is the probability of additional ionization of sputtered atoms in the plasma bulk, from where the arising ions are not directed back to the target; ξ_{n} and ξ_{i} are the probabilities for the target material neutrals and ions to reach the substrate, respectively. Modifications of the original model, developed (Christie, 2005), are denoted by dashed lines.

where S_{m} is the effective sputtering yield of the target material defined as

$$S_{\mathrm{m}} = S_{\mathrm{mg}}(1 - m_{\mathrm{t}}) + S_{\mathrm{mm}} m_{\mathrm{t}}\,. \tag{2.24}$$

Here, S_{mg} and S_{mm} are the process gas-ion and self-sputtering yields of the target material, respectively.

The probability of return of ionized sputtered atoms to the target, σ, assumed to be the same as the probability of backward motion of ionized process gas atoms to the target, has been determined using a balance equation for secondary electrons leaving the target

$$\gamma_{\mathrm{ef}}(1 - d_{\mathrm{e}})\sigma \frac{eU_{\mathrm{d}}}{E_{\mathrm{ef}}} = 1\,, \tag{2.25}$$

where e is the elementary charge, E_{ef} is the effective energy lost per electron-ion pair produced by a secondary electron in a mixture of process gas atoms and sputtered target material atoms in front of the target, and d_{e} is the fraction of secondary electrons lost by diffusive transport before producing the electron-ion pairs. The coefficient γ_{ef} has been written in the form

$$\gamma_{\mathrm{ef}} = (1 - r)\left[\gamma_{\mathrm{mg}}(1 - m_{\mathrm{t}}) + \gamma_{\mathrm{mm}} m_{\mathrm{t}}\right]\,, \tag{2.26}$$

where r is the recapture probability of secondary electrons at the target; γ_{mg} and γ_{mm} are the secondary electron emission coefficients of the target material related to the incident process gas ions and the target material ions, respectively. The effective energy E_{ef} has been expressed as

$$E_{\mathrm{ef}} = E_{\mathrm{g}}(1 - m_{\mathrm{t}}) + E_{\mathrm{m}} m_{\mathrm{t}}\,, \tag{2.27}$$

where E_{g} and E_{m} are the energies lost per electron-ion pair produced by a secondary electron in collisions with the process gas atoms and the target material atoms, respectively.

The probability of ionization of sputtered atoms in front of the target, β, has been calculated using the relation

$$m_{\mathrm{t}} = \beta\sigma S_{\mathrm{m}}\,. \tag{2.28}$$

For Θ, they obtained

$$\Theta = \frac{\left[\beta(1-\sigma) + \gamma(1-\beta)\right]\frac{\xi_{\mathrm{i}}}{\xi_{\mathrm{n}}}}{(1-\beta)(1-\gamma) + \left[\beta(1-\sigma) + \gamma(1-\beta)\right]\frac{\xi_{\mathrm{i}}}{\xi_{\mathrm{n}}}}\,. \tag{2.29}$$

Kadlec (2007) simulated the rarefaction of the process gas in front of the target by a Direct simulation Monte Carlo method. The simulation revealed that the characteristic time for the process gas rarefaction in front of the target is around 50 μs. The decrease of the process gas density is significant and cannot be neglected in HiPIMS discharges, although the results of this simulation might be influenced

by the relatively small simulation volume and by the fact that only neutral atoms were simulated.

Brenning et al. (2008) presented a bulk plasma model which calculated the plasma potential distribution in a magnetron discharge based on the distribution of the magnetic field strength and the target current. The model uses the generalized Ohm's law in the form

$$\mu \boldsymbol{J} + \frac{\boldsymbol{J} \times \boldsymbol{B}}{e n_{\mathrm{e}}} = \boldsymbol{E} + \frac{\nabla p_{\mathrm{e}}}{e n_{\mathrm{e}}}\,, \tag{2.30}$$

where ν is the plasma resistivity, $\boldsymbol{J}$ is the current density, n_{e} is the electron density and p_{e} is the electron pressure. For a given distribution of the electron density, magnetic field and current density, which gives the total current measured at the target, the electric field distribution $\boldsymbol{E}$ was calculated. The plasma resistivity perpendicular to the magnetic field lines can be expressed as

$$\mu_{\perp} = \frac{B}{\omega_{\mathrm{ge}} \tau_{\mathrm{c}} e n_{\mathrm{e}}}\,, \tag{2.31}$$

where the gyration-to-collision frequency ratio $\omega_{\mathrm{ge}} \tau_{\mathrm{c}}$ can be regarded as an input parameter determining the character of the cross-field electron diffusion. The results of this model shows that a region with a negative plasma potential and an electric field directed towards the target is formed in front of the target for $8 < \omega_{\mathrm{ge}} \tau_{\mathrm{c}} < 50$ which is the typical range of the parameter associated with magnetron discharges. For $\omega_{\mathrm{ge}} \tau_{\mathrm{c}} < 4$, which corresponds to an anomalous cross-field electron diffusion (Brenning et al., 2009; Lundin, Helmersson, Kirkpatrick, Rohde and Brenning, 2008), the plasma potential has a positive maximum near the target.

3 Aims of the thesis

The main motivation of this thesis is to develop a mathematical model of high-power impulse magnetron sputtering discharges. It was discussed in the previous section that a particle model of the whole process would be complicated and its solution very time-demanding. Up-to-date HiPIMS models are either steady-state analytical models or non-self-consistent simulations of specific processes. Therefore our aim was to develop a relatively simple time-dependent global model which would, however, describe the time evolution of the whole discharge in a self-consistent way. Such model calculations could be carried out very quickly and thus they could be used to analyse the effects of various input parameters on the discharge and deposition characteristics of HiPIMS.

The aims of the thesis has been set as follows:

1. Develop a non-stationary model of high-power impulse magnetron sputtering discharges. The model must include the process gas and the target material atoms and ions and their reactions in the discharge plasma relevant for HiPIMS discharges. The model must be able to simulate the sputtering of target material atoms and their transport towards the substrate.

2. Prepare necessary material data of argon gas and copper target for model calculations.

3. Compare the target current waveforms, plasma densities and electron temperatures calculated by the model with experimental results for two different HiPIMS systems.

4. Use the model to investigate the effects of input parameters (target voltage, target power, magnetic field strength, pulse length and shape) on the discharge and deposition characteristics (composition of the discharge plasma, deposition rate and ionized fraction of the target material atoms in the flux onto the substrate) under typical conditions used in real HiPIMS discharges and explain the results.

5. Compare the results of the non-stationary two-zone model with the predictions of the steady-state phenomenological model (Vlček and Burcalová, 2010).

4 Non-stationary two-zone model

In this chapter, a non-stationary two-zone model for HiPIMS discharges will be presented. The model is based on a global-model description of plasma. Therefore, the spatial resolution of the model is reduced, but the equations describing the time-evolution of plasma characteristics can be solved over the whole period of the voltage pulse. The aim of the model is to provide fundamental understanding of the role of the process gas and the target material atoms in the target sputtering and film deposition in HiPIMS.

The main advantages of the model are (1) self-consistency, allowing to calculate the target current as well as the deposition rate based on the process input parameters and material parameters, (2) very fast solution, allowing to perform many series of calculations for various input parameters and thus to discover general relations between them. The new features of this model, with respect to previous global plasma models, are (1) the division of the simulated volume into two zones, which reflect the spatial structure of a magnetron discharge, (2) an incorporation of fast (secondary) electrons and fast sputtered target material atoms apart from the thermalized electrons and atoms, (3) an introduction of a calculated potential drop (magnetic presheath) near the target and (4) a self-consistent calculation of the target current.

The development of the model from the first idea towards the present state lasted over two years. In the beginning, a concept of the global model was implemented and material data for model calculations were prepared. By validating the model results with experimental results it was found that some experimental trends are not well resolved by the model. Based on recent papers, several key physical processes that should be included in the model were identified, e.g., the magnetic presheath potential in Zone I and the velocity distribution of the sputtered target material atoms. The evolution of the model was not straightforward, several difficulties had to be solved, some ideas were discarded after some effort due to their complexity or little benefit. After a repeating validation of the model, we believe the present-state model describes the discharge physics optimally in the sense that a significant improvement of the model would require its extensive modification. The following sections will describe the details of the model.

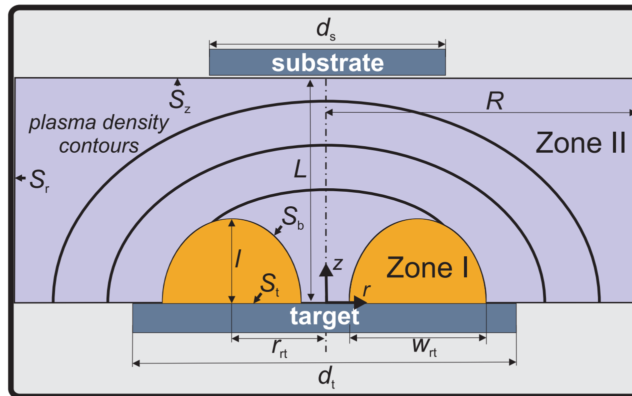

Figure 4.1: Schematic illustration of the model geometry. The cylindrically symmetric discharge plasma between the planar target and the planar substrate is divided into two zones: the high density plasma confined in a ring-shaped region above the target racetrack (Zone I) and the bulk plasma filling the space between Zone I and the substrate (Zone II).

4.1 Model geometry and spatial approximations

The model describes a cylindrically symmetric planar magnetron. A cylindrical (r, z) coordinate system with the zero point in the centre of the target is used. A complication for the application of a global model, used before for other types of discharges (Ashida et al., 1995; Lichtenberg and Lieberman, 2000; Kim et al., 2006; Hjartarson et al., 2010), onto HiPIMS discharges is the high inhomogeneity of plasma in a magnetron discharge. The magnetron's magnetic field causes formation of a high-density plasma a few centimetres above the target racetrack (Gu and Lieberman, 1988; Miranda et al., 1990). This region, where the ions used for the sputtering of the target are generated, is the core of the discharge. Its importance was emphasized by several authors (Bretagne et al., 1997; Buyle et al., 2004; Olsson and Macák, 2000; Brenning et al., 2008; Samuelsson et al., 2010). Therefore, a key idea was to divide the discharge plasma into two zones as shown in figure 4.1. Zone I represents the high-density plasma above the target racetrack of a planar target, where the electrons are confined by a strong magnetic field. Zone II covers the rest of the discharge volume between Zone I and the planar substrate. There, the effect of the magnetic field on the plasma can be neglected and transport of plasma from Zone I towards chamber walls dominates over plasma generation. Consequently, a decreasing plasma density in the direction towards the chamber walls can be expected, as indicated also by optical emission from the plasma (Gu and Lieberman, 1988).

The dimensions of the simulation volume are given by the target-to-substrate distance L and the vacuum chamber radius R. An expansion of plasma behind the substrate is neglected in the model.

	Electrons	**Gas atoms**	**Metal atoms**
Thermalized	n_e, w_e	n_g	n_m
Fast	n_ef	n_gf	n_mf
Singly ionized		n_gi	n_mi

Table 4.1: List of species included in the model with their associated physical quantities that are the time-dependent variables. Particle densities are denoted by n and kinetic energy densities by w.

The region of high-density plasma (Zone I) is given by the distribution of ionization of neutral atoms realized mainly by secondary electrons, and thus it is depending predominantly on the distribution of the magnetic field above the target. However, even for a known distribution of the magnetic field, there is a freedom in determining an exact boundary between Zone I and Zone II. For the sake of the model, the dimensions of Zone I are specified by the racetrack radius r_rt, its width w_rt and the height l, see figure 4.1. In the first approximation, these are tied to the target diameter, d_t, by setting $r_\mathrm{rt} = w_\mathrm{rt} = d_\mathrm{t}/4$ and $l = w_\mathrm{rt}/2$. The Zone II is given by the complement of Zone I to the whole simulation volume. The target diameter, the substrate diameter, d_s, the chamber radius, R, and the target-to-substrate distance, L, are geometrical input parameters of the model. The zone volumes are then calculated as

$$V_\mathrm{I} = \pi^2 r_\mathrm{rt} l^2 \,, \tag{4.1a}$$

$$V_\mathrm{II} = \pi R^2 L - V_\mathrm{I} \,. \tag{4.1b}$$

In order to describe the transport of particles between the zones and onto the target and chamber walls, we distinguish 4 boundary surfaces (see figure 4.1): (1) the surface between Zone I and the racetrack, denoted S_t, (2) the surface between Zone I and Zone II, denoted S_b, (3) the chamber wall at $r = R$, denoted S_r and (4) the substrate position boundary at $z = L$, denoted S_z. The areas of these surfaces are calculated as

$$S_\mathrm{t} = 2\pi r_\mathrm{rt} w_\mathrm{rt} \,, \tag{4.2a}$$

$$S_\mathrm{b} = 2\pi^2 r_\mathrm{rt} l \,, \tag{4.2b}$$

$$S_\mathrm{r} = 2\pi R L \,, \tag{4.2c}$$

$$S_\mathrm{z} = \pi R^2 \,, \tag{4.2d}$$

$$S_\mathrm{s} = \pi d_\mathrm{s}^2/4 \,, \tag{4.2e}$$

where S_s is the area of the substrate, which is also included in the S_z area.

The model includes electrons, atoms and singly charged ions of both the process gas and the target material (see table 4.1). Moreover, to take into account the non-equilibrium velocity distribution of the neutral atoms, we separate them into two groups: (1) thermalized atoms with the temperature T and (2) fast atoms with a

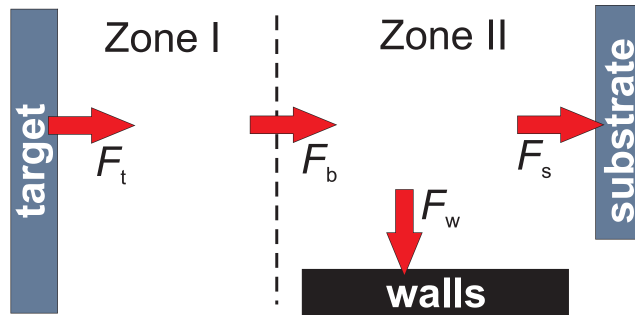

Figure 4.2: Illustration of the total particle fluxes F across zone boundaries. The arrows indicate the positive directions of the fluxes. In the text, various symbols are used instead of F for the fluxes of individual species: E and E_{f} for thermalized and fast electrons, G, G_{f} and G_{i} for thermalized, fast and ionized process gas atoms, and M, M_{f} and M_{i} for thermalized, fast and ionized target material atoms, respectively.

directed velocity u_{s}, corresponding to the average velocity of the atoms sputtered from the target (see (4.28) below). Analogously, we distinguish between thermalized electrons characterized by a selected type of the energy distribution function $g_{\mathrm{e}}(\varepsilon)$, and fast (secondary) electrons with initial energy gained in the target sheath (eU_{s}). The notation of the fluxes across zone boundaries is shown in figure 4.2.

For all species, global particle conservation equations are solved in order to obtain the time evolution of their densities in both zones. We assume that each density of a given particle type factors into a fixed spatial distribution part and a calculated time-dependent magnitude, i.e.

$$N(t, \boldsymbol{x}) = n(t)\tilde{n}(\boldsymbol{x}) \, . \tag{4.3}$$

Based on the geometry of the zones and the dominant transport phenomena for the particle species, three different spatial distribution functions are used in the model.

In Zone I, a constant density distribution function

$$\tilde{n}_{\mathrm{con}}(r, z) = 1 \tag{4.4}$$

is used for thermalized and fast electrons, thermalized atoms and ions, since the zone is relatively small. In Zone II, the thermalized process gas density is assumed to be constant as well, taking into account diffusive scattering off the walls and a preset balance between its inflow and outflow for a given working pressure. On the other hand, the spatial density distributions of charged particles and thermalized metal atoms in Zone II are the result of a diffusive transport, so they may be described by a parabolic function proposed by Hopwood (1998)

$$\tilde{n}^{\mathrm{II}}_{\mathrm{par}}(r, z) = [1 - (1 - h_{\mathrm{r}})(r/R)^2] \times [1 - (1 - h_{\mathrm{z}})(z/L)^2] \, , \tag{4.5}$$

where h_{r} and h_{z} are wall factors. For ions, they are calculated according to the

formulas of Godyak(Ashida et al., 1995; Lieberman and Lichtenberg, 2005)

$$h_{\mathrm{r,i}} = 0.8(4 + R/\bar{\lambda}_{\mathrm{i}})^{-1/2}\,, \tag{4.6a}$$

$$h_{\mathrm{z,i}} = 0.86(3 + L/\bar{\lambda}_{\mathrm{i}})^{-1/2}\,, \tag{4.6b}$$

whereas for the thermalized metal atoms, the wall factors are determined from the boundary condition for diffusion as

$$h_{\mathrm{r,m}} = [1 + 2R\gamma/(\pi\bar{\lambda}_{\mathrm{m}}(2-\gamma))]^{-1}\,, \tag{4.7a}$$

$$h_{\mathrm{z,m}} = [1 + 2L\gamma/(\pi\bar{\lambda}_{\mathrm{m}}(2-\gamma))]^{-1}\,. \tag{4.7b}$$

Here $\bar{\lambda} = \left[\sqrt{2}p\sigma/(kT)\right]^{-1}$ is the average ion or metal atom mean free path, p is the gas pressure, k is the Boltzmann constant, T is the thermodynamic temperature of the gas, γ is the corresponding sticking coefficient, and σ is the cross section of charge transfer between ions and gas atoms or the elastic scattering cross section between metal and gas atoms.

The spatial density distributions of the fast neutral atoms in Zone I ($\tilde{n}^{\mathrm{I}}_{\mathrm{exp}}$) and Zone II ($\tilde{n}^{\mathrm{II}}_{\mathrm{exp}}$) are approximated by functions

$$\tilde{n}^{\mathrm{I}}_{\mathrm{exp}}(r,z) = f(r,z)\exp\left[-\sqrt{(r-r_{\mathrm{rt}})^2+z^2}/\lambda^{\mathrm{I}}_{\mathrm{f}}\right]\,, \tag{4.8a}$$

$$\tilde{n}^{\mathrm{II}}_{\mathrm{exp}}(r,z) = f(r,z)\exp\left[-(\sqrt{(r-r_{\mathrm{rt}})^2+z^2}-l)/\lambda^{\mathrm{II}}_{\mathrm{f}}\right]\,, \tag{4.8b}$$

respectively. The function

$$f(r,z) = \int_0^{2\pi}\int_{r_{\mathrm{rt}}-\frac{w_{\mathrm{rt}}}{2}}^{r_{\mathrm{rt}}+\frac{w_{\mathrm{rt}}}{2}} \frac{3z^3 r_0 \mathrm{d}r_0 \mathrm{d}\phi}{(r^2+r_0^2-2rr_0\cos\phi+z^2)^{2.5}} \tag{4.9}$$

determines the spatial distribution of the fast atoms assuming a cosine law sputtering from the planar target racetrack and a transport without collisions. The exponential part, where $\lambda^{\mathrm{I}}_{\mathrm{f}}$ and $\lambda^{\mathrm{II}}_{\mathrm{f}}$ are the mean free paths of the fast atoms in Zone I and Zone II, respectively, accounts for the collisions which lead to depopulation of the particle flux. The assignment of spatial distribution functions for the particle species included in the model is summarized in table 4.2.

For the global conservation equations, we need the volume and surface integrals of the spatial distribution function, see (4.15) and (4.16) below. The integration of a constant function is simple; it gives the volumes of the zones and the areas of the boundary surfaces without any correction. The integrals of the parabolic function in Zone II, where it is used, can be written analytically in terms of the zone dimensions and the wall factors h_{r} and h_{z}. The results are summarized in table 4.3.

The exponential distribution functions are complicated due to the fact that the fast atoms are sputtered in various directions from the target and they are depopulated by collisions, see (4.8) and (4.9). In a steady state, the flux of fast particles from Zone I into Zone II must be equal to the flux from the target, assuming no

Zone	Electrons I	Electrons II	Gas atoms I	Gas atoms II	Metal atoms I	Metal atoms II
Thermalized	con	par	con	con	con	par
Fast	con	con	exp	exp	exp	exp
Singly ionized			con	par	con	par

Table 4.2: Assignment of spatial density distribution functions to the species included in the model; con = constant (4.4), par = parabolic (4.5), exp = exponential (4.8).

$\tilde{V}_{\mathrm{II,par}}$	$=$	$\frac{1}{6}\pi R^2 L(h_{\mathrm{z}}+2)(h_{\mathrm{r}}+1)-V_{\mathrm{I}}$
$\tilde{S}_{\mathrm{r,par}}$	$=$	$\frac{1}{3}S_{\mathrm{r}}h_{\mathrm{r}}(h_{\mathrm{z}}+2)$
$\tilde{S}_{\mathrm{z,par}}$	$=$	$\frac{1}{2}S_{\mathrm{z}}h_{\mathrm{z}}(h_{\mathrm{r}}+1)$
$\tilde{S}_{\mathrm{s,par}}$	$=$	$S_{\mathrm{s}}h_{\mathrm{z}}\left[1-\frac{1}{2}(1-h_{\mathrm{r}})\left(\frac{d_{\mathrm{s}}}{2R}\right)^2\right]$

Table 4.3: Volume and surface integrals of the parabolic spatial distribution function in Zone II.

collisions occur in Zone I. Similarly, the sum of the fluxes onto the boundary surfaces S_{r} and S_{z} equals the total flux into Zone II. We derived that the particle flux distribution at the $z = L$ plane, assuming the particles are sputtered uniformly from the target racetrack with a cosine law angular distribution, is given by

$$\Gamma_{\mathrm{z}}(r) = \frac{1}{4\pi r_{\mathrm{rt}} w_{\mathrm{rt}}}\left[\frac{-r^2+(r_{\mathrm{rt}}+0.5w_{\mathrm{rt}})^2-L^2}{[((r-r_{\mathrm{rt}}-0.5w_{\mathrm{rt}})^2+L^2)((r+r_{\mathrm{rt}}+0.5w_{\mathrm{rt}})^2+L^2)]^{0.5}}- \right.$$
$$\left. -\frac{-r^2+(r_{\mathrm{rt}}-0.5w_{\mathrm{rt}})^2-L^2}{[((r-r_{\mathrm{rt}}+0.5w_{\mathrm{rt}})^2+L^2)((r+r_{\mathrm{rt}}-0.5w_{\mathrm{rt}})^2+L^2)]^{0.5}}\right]. \quad (4.10)$$

Then the integral

$$f_{\mathrm{z}} = \int_0^R \Gamma_{\mathrm{z}}(r) 2\pi r \mathrm{d}r \quad (4.11)$$

determines the fraction of the total flux incident on the S_{z} surface and $1 - f_{\mathrm{z}}$ determines the fraction incident on the S_{r} surface, assuming no collisions occur in Zone I. Analogously, the fraction

$$f_{\mathrm{s}} = \int_0^{\frac{d_{\mathrm{s}}}{2}} \Gamma_{\mathrm{z}}(r) 2\pi r \mathrm{d}r \quad (4.12)$$

determines the fraction of the total flux incident on the substrate. In order to further simplify the integration of the exponential part of the distribution functions (4.8), we use the approximation that in Zone I, the fast atoms travel the distance l, and in Zone II, the fraction f_{z} travels the distance of L and the fraction $1 - f_{\mathrm{z}}$ travels the distance of R. The resulting volume and surface integrals are summarized in table 4.4.

$\tilde{V}_{\mathrm{I,exp}}$	$=$	$S_{\mathrm{t}}\lambda_{\mathrm{f}}^{\mathrm{I}}[1-\exp(-l/\lambda_{\mathrm{f}}^{\mathrm{I}})]$
$\tilde{S}_{\mathrm{b,exp}}$	$=$	$S_{\mathrm{t}}\exp(-l/\lambda_{\mathrm{f}}^{\mathrm{I}})$
$\tilde{V}_{\mathrm{II,exp}}$	$=$	$S_{\mathrm{b}}\lambda_{\mathrm{f}}^{\mathrm{II}}[1-(1-f_{\mathrm{z}})\exp(-R/\lambda_{\mathrm{f}}^{\mathrm{II}})-f_{\mathrm{z}}\exp(-L/\lambda_{\mathrm{f}}^{\mathrm{II}})]$
$\tilde{S}_{\mathrm{r,exp}}$	$=$	$S_{\mathrm{b}}(1-f_{\mathrm{z}})\exp(-R/\lambda_{\mathrm{f}}^{\mathrm{II}})$
$\tilde{S}_{\mathrm{z,exp}}$	$=$	$S_{\mathrm{b}}f_{\mathrm{z}}\exp(-L/\lambda_{\mathrm{f}}^{\mathrm{II}})$
$\tilde{S}_{\mathrm{s,exp}}$	$=$	$S_{\mathrm{b}}f_{\mathrm{s}}\exp(-L/\lambda_{\mathrm{f}}^{\mathrm{II}})$

Table 4.4: Volume and surface integrals of the exponential spatial distribution functions in both zones.

4.2 Conservation equations

The building block of the mathematical representation of the model is the global particle conservation equation (2.20). It is used to solve the time evolution of the time-dependent density magnitude for all particle densities in both zones, except for the thermalized electrons. Their density can be evaluated directly from the condition of quasi-neutrality

$$n_{\mathrm{e}}=n_{\mathrm{gi}}+n_{\mathrm{mi}}-n_{\mathrm{ef}}\,. \tag{4.13}$$

In the model, the global particle conservation equation is used in the form

$$\tilde{V}\frac{\mathrm{d}n(t)}{\mathrm{d}t}+\sum_i n(t)u_i(t)\tilde{S}_i=\sum_c n_{c1}(t)n_{c2}(t)K_c(t)\tilde{V}_c\,, \tag{4.14}$$

where $u_i(t)$ is an average particle velocity across the i-th boundary surface, $n_{c1}(t)$ and $n_{c2}(t)$ are the densities of particles interacting in a binary collision with the corresponding collision rate constant $K_c(t)$. In this equation, the spatial distribution function $\tilde{n}(\boldsymbol{x})$ is integrated over the zone volume and boundary surfaces, yielding the factors $\tilde{V}$ and $\tilde{S}_i$, respectively. Comparing equations (2.20) and (4.14), it follows that

$$\tilde{V} = \int_V \tilde{n}(\boldsymbol{x})\mathrm{d}\boldsymbol{x} \qquad \text{and} \tag{4.15}$$

$$\tilde{S}_i = \int_{S_i} \tilde{n}(\boldsymbol{x})\mathrm{d}\boldsymbol{x}\,, \tag{4.16}$$

where V is the zone volume and S_i is the area of the i-th boundary surface. Analogously, the reaction spatial integral $\tilde{V}_c$ is an integral of the product of spatial distribution functions corresponding to the densities of the interacting particles, i.e.

$$\tilde{V}_c=\int_V \tilde{n}_{c1}(\boldsymbol{x})\tilde{n}_{c2}(\boldsymbol{x})\mathrm{d}\boldsymbol{x}\,. \tag{4.17}$$

It is assumed that thermalized atoms and ions can be characterized by a Maxwellian velocity distribution with a constant temperature T. Only the spatially

constant temperatures of thermalized electrons are calculated for both zones from the global electron energy conservation equation, which has the form

$$\tilde{V}_{n_\mathrm{e}} \frac{\mathrm{d}w_\mathrm{e}(t)}{\mathrm{d}t} + \sum_i \mathcal{E}_i(t) = P_\mathrm{e} + \sum_c n_{c1}(t) n_{c2}(t) \mathcal{K}_c(t) \tilde{V}_c \,, \tag{4.18}$$

where $w_\mathrm{e} = 3/2 n_\mathrm{e} kT_\mathrm{e}$ is the kinetic energy density of electrons, $\mathcal{E}_i(t)$ is the total energy flux across a zone boundary, P_e is the power input due to an external electric field, $n_{c1}(t)$ and $n_{c2}(t)$ are the densities of particles interacting in a binary collision and $\mathcal{K}_c(t)$ is the corresponding rate constant for the change of energy density in the reaction. The flux of energy across zone boundaries is given by convection, i.e.

$$\mathcal{E}_i = E_i k_\mathrm{w} kT_\mathrm{e} \,, \tag{4.19}$$

where E_i is the total flux of electrons across the zone boundary and $k_\mathrm{w} kT_\mathrm{e}$ is the average energy transported across a unit area by one electron. The constant k_w depends on the electron energy distribution function (EEDF) of the thermalized electrons, which is preset for each model calculation.

The first term on the right hand side of (4.18), P_e, represents the Ohmic heating, i.e. the energy gained by electrons due to an external electric field. According to recent plasma potential measurements and calculations (Bradley et al., 2001; Bultinck and Bogaerts, 2008; Mishra et al., 2010; Rauch et al., 2012), a non-zero electric field (magnetic presheath) extends from the target sheath to a distance of several centimetres. This electric field is formed in order to maintain the quasi-neutrality of the plasma above the target racetrack by affecting the fluxes of ions and magnetized electrons. In the model, a constant electric field in Zone I is assumed (see figure 4.3). Therefore, the Ohmic heating term in Zone I can be expressed as $P_\mathrm{e}^\mathrm{I} = eE_\mathrm{b} U_\mathrm{I}$, where E_b is the total flux of electrons from Zone I to Zone II and U_I is the potential drop across Zone I. Since the quasi-neutrality condition is used directly for the calculation of electron fluxes from Zone II onto the chamber walls, and thus the plasma potential in Zone II is not needed, we set its value equal to zero. The Ohmic heating in Zone II is then neglected. The potential drop across the target sheath is calculated by the relation $U_\mathrm{s} = U_\mathrm{d} - U_\mathrm{I}$, where U_d is the discharge voltage applied to the target.

The quasi-neutrality condition for the fluxes into and out of Zone I can be written as

$$\Delta Q = G_\mathrm{i,b} - G_\mathrm{i,t} + M_\mathrm{i,b} - M_\mathrm{i,t} - E_\mathrm{b} + E_\mathrm{f,t} = 0 \,, \tag{4.20}$$

where the terms on the right-hand-side represent total charged particle fluxes corresponding to Zone I, see figure 4.2. It will be seen below from the definition of the fluxes, that this is a non-linear equation of U_I. The solution of such an equation at each time-step is not very conformable with the solution of other ordinary differential equations in Matlab, whose routines change the time-step adaptively. Therefore, the solution for the Zone I potential was rewritten in the form of an ordinary differential equation in the form

$$\frac{\mathrm{d}U_\mathrm{I}}{\mathrm{d}t} = \frac{el^2}{\epsilon_0 V_\mathrm{I}} \left(G_\mathrm{i,b} - G_\mathrm{i,t} + M_\mathrm{i,b} - M_\mathrm{i,t} - E_\mathrm{b} + E_\mathrm{f,t} \right) . \tag{4.21}$$

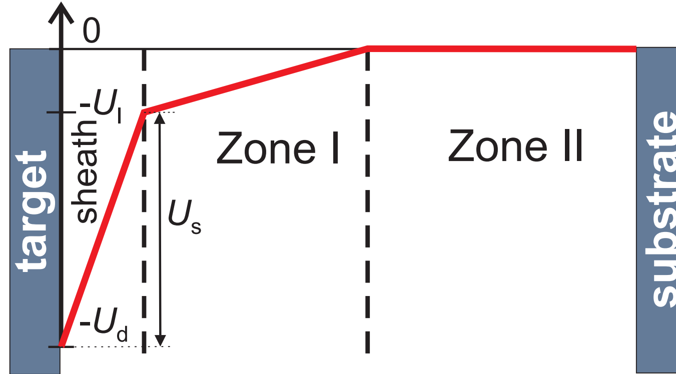

Figure 4.3: Schematic representation of the electrostatic potential in the model. The target potential is set to $-U_\mathrm{d}$. Across Zone I a voltage drop U_I is assumed. The voltage drop in the target sheath then equals $U_\mathrm{d} - U_\mathrm{I}$. In Zone II the electrostatic potential is assumed to be zero.

This equation can be solved simultaneously with other ordinary differential equations arising from the particle and energy conservation equations. Whenever the term on the right-hand side is non-zero, the value of U_I is changed accordingly. The scaling factor $el^2/(\epsilon_0 V_\mathrm{I})$ arises from the Poisson equation, taking l as the characteristic dimension of Zone I for the space derivatives. It can be calculated, that the time-scale for the change of U_I is much smaller than the time-scale for the change of the plasma density in Zone I, and thus U_I quickly converges to the equilibrium point where $\Delta Q = 0$ for the actual charged particle fluxes.

4.2.1 Particle transport

The transport of particles in the simulation volume is described by the integral fluxes into and from the zone volumes in the form

$$F_i = n(t)u_i(t)\tilde{S}_i\,, \tag{4.22}$$

see the second term in (4.14) and figure 4.2.

The diffusion coefficients which appear in the relations for the fluxes between Zone I and Zone II are generally expressed as $D = 8\lambda\bar{v}/\pi$, where λ is the mean free path for the collisions of the diffusing species and $\bar{v}$ is their thermal velocity. To prevent the diffusion coefficient from increasing ad infinitum for low pressures, we set its maximum to $D = \bar{v}l/4$ which corresponds to the thermal flux of particles. In the following paragraphs, the relations for the fluxes of all plasma species will be explained.

Target material atoms The sticking coefficient of the target material atoms is assumed to be unity, i.e. every atom incident on a surface is deposited there. The flux of thermalized target material atoms onto the target is given by the thermal

flux

$$M_{\mathrm{t}} = -\frac{1}{4} n_{\mathrm{m}}^{\mathrm{I}} \bar{v}_{\mathrm{m}} S_{\mathrm{t}} \,, \tag{4.23}$$

where $\bar{v}_{\mathrm{m}}$ is the thermal velocity of the metal atoms. The flux of fast target material atoms, i.e. the sputtered atoms, is given by

$$M_{\mathrm{f,t}} = -G_{\mathrm{i,t}} Y_{\mathrm{g}}(U_{\mathrm{s}}) - M_{\mathrm{i,t}} Y_{\mathrm{m}}(U_{\mathrm{s}}) \,, \tag{4.24}$$

where $G_{\mathrm{i,t}}$ and $M_{\mathrm{i,t}}$ are the fluxes of the process gas and the target material ions onto the target, respectively, and Y_{g} and Y_{m} are the sputtering yields induced by the process gas and target material ions, respectively, which depend on the ion energy (eU_{s}) gained in the sheath.

The flux of thermalized atoms between the zones is approximated by the diffusion equation

$$M_{\mathrm{b}} = \frac{D_{\mathrm{m}}}{l} \left(n_{\mathrm{m}}^{\mathrm{I}} - n_{\mathrm{m}}^{\mathrm{II}} \right) S_{\mathrm{b}} \,. \tag{4.25}$$

Here, the diffusion coefficient, D_{m}, is calculated using

$$\lambda_{\mathrm{m}}^{\mathrm{I}} = \left[\sqrt{2} (n_{\mathrm{g}}^{\mathrm{I}} \sigma_{\mathrm{mg}} + n_{\mathrm{m}}^{\mathrm{I}} \sigma_{\mathrm{mm}}) \right]^{-1} \,, \tag{4.26}$$

where σ_{mg} and σ_{mg} are the cross sections for elastic scattering of target material atoms on process gas and target material atoms, respectively.

The flux of fast atoms between the zones is given by the fast atom density in Zone I, the velocity of sputtered atoms, u_{s}, and the density at the boundary, which is given by the exponential spatial distribution function, see (4.8) and table 4.4. The flux can then be written as

$$M_{\mathrm{f,b}} = n_{\mathrm{mf}}^{\mathrm{I}} u_{\mathrm{s}} \tilde{S}_{\mathrm{mf,b}} = n_{\mathrm{mf}}^{\mathrm{I}} u_{\mathrm{s}} \exp\left(-l / \lambda_{\mathrm{mf}}^{\mathrm{I}} \right) S_{\mathrm{t}} \,. \tag{4.27}$$

The velocity, u_{s}, is given as the most probable velocity in the Thompson distribution of sputtered particles, which can be calculated from the surface binding energy $\varepsilon_{\mathrm{sb}}$ by the relation (Betz and Wien, 1994)

$$u_{\mathrm{s}} = \sqrt{\frac{\varepsilon_{\mathrm{sb}}}{m_{\mathrm{m}}}} \,. \tag{4.28}$$

Since the sputtered target material atoms are the main source of this particle momentum away from the target, this velocity is used in reference to all fast atoms in the model.

The fluxes of thermalized target material atoms to the walls are given by the average velocity $\bar{v}_{\mathrm{m}}/2$, see eq. 5.2.4 in Lieberman and Lichtenberg (2005), which leads to

$$M_{\mathrm{w}} = \frac{1}{2} n_{\mathrm{m}}^{\mathrm{II}} \bar{v}_{\mathrm{m}} (\tilde{S}_{\mathrm{m,r}} + \tilde{S}_{\mathrm{m,z}}) \,. \tag{4.29}$$

The flux of fast atoms onto the chamber walls is given by

$$M_{\mathrm{f,w}} = n_{\mathrm{mf}}^{\mathrm{II}} u_{\mathrm{s}} (\tilde{S}_{\mathrm{mf,r}} + \tilde{S}_{\mathrm{mf,z}}) \,. \tag{4.30}$$

The fluxes of target material atoms onto the substrate can be written analogously, i.e.

$$M_{\mathrm{s}} = \frac{1}{2} n_{\mathrm{m}}^{\mathrm{II}} \bar{v}_{\mathrm{m}} \tilde{S}_{\mathrm{m,s}} \qquad \text{and} \tag{4.31}$$

$$M_{\mathrm{f,s}} = n_{\mathrm{mf}}^{\mathrm{II}} u_{\mathrm{s}} \tilde{S}_{\mathrm{mf,s}} \, . \tag{4.32}$$

The mean free paths $\lambda_{\mathrm{mf}}^{\mathrm{I}}$ and $\lambda_{\mathrm{mf}}^{\mathrm{II}}$ can be expressed as

$$\lambda_{\mathrm{mf}} = \left[n_{\mathrm{g}} \sigma_{\mathrm{mg}} \frac{m_{\mathrm{g}}}{m_{\mathrm{g}} + m_{\mathrm{m}}} + n_{\mathrm{m}} \sigma_{\mathrm{mm}} 0.5 + n_{\mathrm{gi}} \sigma_{\mathrm{mg,ct}} + n_{\mathrm{mi}} \sigma_{\mathrm{mm,ct}} + + \frac{n_{\mathrm{e}} K_{\text{e-m,iz}} + n_{\mathrm{ef}} K_{\text{ef-m,iz}}}{u_{\mathrm{s}}} \right]^{-1} , \tag{4.33}$$

where the corresponding particle densities in either Zone I or Zone II would be used. The terms represent the losses of the fast atoms due to the thermalization by collisions with process gas and target material atoms, due to the charge transfer collision with process gas and target material ions and due to the ionization by thermalized and fast electrons, respectively. For the definition of the collision rate constants, see section 4.2.2.

Process gas atoms The process gas is assumed to have zero sticking coefficient on the target, substrate and chamber walls, so all impacting atoms are immediately reflected back into the plasma volume. In addition, it is assumed that fast atoms are thermalized on the surfaces. On the target, impacting energetic process gas ions are reflected from the target surface or implanted into the target. Since noble gas atoms are very weakly bound in materials, these implanted atoms diffuse out of the target or they are resputtered together with the target material. Little is known about the energy distribution of the process gas atoms coming from the target, which might be complicated. However, reflected atoms and also the sputtered target material atoms have high energies of several eV. Therefore, for the sake of simplicity, it is assumed that process gas atoms leave the target as fast atoms. Hence,

$$G_{\mathrm{t}} = 0 \qquad \text{and} \tag{4.34}$$

$$G_{\mathrm{f,t}} = -G_{\mathrm{i,t}} \, , \tag{4.35}$$

where $G_{\mathrm{f,t}}$ and $G_{\mathrm{i,t}}$ are the fluxes of fast process gas atoms and ions from the target, respectively. The flux of thermalized atoms between the zones is approximated by the diffusion equation

$$G_{\mathrm{b}} = \frac{D_{\mathrm{g}}}{l} \left(n_{\mathrm{g}}^{\mathrm{I}} - n_{\mathrm{g}}^{\mathrm{II}} \right) S_{\mathrm{b}} \, . \tag{4.36}$$

Here, the diffusion coefficient D_{g} is calculated using

$$\lambda_{\mathrm{g}}^{\mathrm{I}} = \left[\sqrt{2} (n_{\mathrm{g}}^{\mathrm{I}} \sigma_{\mathrm{gg}} + n_{\mathrm{m}}^{\mathrm{I}} \sigma_{\mathrm{mg}}) \right]^{-1} , \tag{4.37}$$

where σ_{gg} and σ_{mg} are the cross sections for elastic scattering of process gas atoms on process gas and target material atoms, respectively. The flux of fast atoms between the zones is given by

$$G_{\mathrm{f,b}} = n_{\mathrm{gf}}^{\mathrm{I}} u_{\mathrm{s}} \tilde{S}_{\mathrm{mf,b}} = n_{\mathrm{gf}}^{\mathrm{I}} u_{\mathrm{s}} \exp\left(-l/\lambda_{\mathrm{gf}}^{\mathrm{I}}\right) S_{\mathrm{t}} \, . \tag{4.38}$$

The flux of thermalized atoms from chamber walls includes the neutralized process gas ions and the reflected fast atoms. Only the gas atoms incident on the pumping system outlet (area S_{p}) are lost from Zone II. This loss is balanced by the gas inlet, whose flow is set to maintain the desired process gas pressure, p, under steady-state no-discharge conditions. This leads to

$$G_{\mathrm{w}} = -G_{\mathrm{i,w}} - G_{\mathrm{f,w}} + \frac{1}{4}\bar{v}_{\mathrm{g}}\left(n_{\mathrm{g}}^{\mathrm{II}} - \frac{p}{kT}\right) S_{\mathrm{p}} \, . \tag{4.39}$$

The flux of fast atoms onto the substrate and chamber walls is given by

$$G_{\mathrm{f,w}} = n_{\mathrm{gf}}^{\mathrm{II}} u_{\mathrm{s}} (\tilde{S}_{\mathrm{gf,r}} + \tilde{S}_{\mathrm{gf,z}}) \tag{4.40}$$

The mean free paths $\lambda_{\mathrm{gf}}^{\mathrm{I}}$ and $\lambda_{\mathrm{gf}}^{\mathrm{II}}$ can be expressed, analogously to the previous case of the fast target material atoms, as

$$\lambda_{\mathrm{gf}} = \left[n_{\mathrm{g}}\sigma_{\mathrm{gg}} 0.5 + n_{\mathrm{m}}\sigma_{\mathrm{mg}} \frac{m_{\mathrm{m}}}{m_{\mathrm{g}} + m_{\mathrm{m}}} + n_{\mathrm{gi}}\sigma_{\mathrm{gg,ct}} + n_{\mathrm{mi}}\sigma_{\mathrm{gm,ct}} + \right. \\ \left. + \frac{n_{\mathrm{e}} K_{\text{e-g,iz}} + n_{\mathrm{ef}} K_{\text{ef-g,iz}}}{u_{\mathrm{s}}} \right]^{-1} , \tag{4.41}$$

where the corresponding particle densities in either Zone I or Zone II would be used.

Process-gas and target-material ions The velocity of ions at a sheath edge is assumed to be the Bohm velocity

$$u_{\mathrm{B}} = k_{\mathrm{bv}} \sqrt{\frac{kT_{\mathrm{e}}}{m_{\mathrm{i}}}} \, , \tag{4.42}$$

where m_{i} is the mass of the ion and the dimensionless factor k_{bv} depends on the given EEDF through the relation of Riemann (1991)

$$k_{\mathrm{bv}} = \left[\frac{kT_{\mathrm{e}}}{2} \int_0^\infty \frac{g_{\mathrm{e}}(\varepsilon)}{\varepsilon} \mathrm{d}\varepsilon \right]^{-0.5} \, . \tag{4.43}$$

The Bohm velocity represents a necessary minimum ion velocity and this approach is commonly used in similar global models, e.g., Ashida et al. (1995) and Hjartarson et al. (2010). The flux of process gas ions onto the target is then given by

$$G_{\mathrm{i,t}} = -0.61 n_{\mathrm{gi}}^{\mathrm{I}} k_{\mathrm{bv}} \sqrt{\frac{kT_{\mathrm{e}}^{\mathrm{I}}}{m_{\mathrm{g}}}} S_{\mathrm{t}} \, , \tag{4.44}$$

where the constant 0.61 corresponds to the decrease of density across a collisionless presheath, see eq. (14.5.14) in Lieberman and Lichtenberg (2005).

The flux of the process gas ions between the zones is expressed by a drift-diffusion approximation in the form

$$G_{\mathrm{i,b}} = \frac{D_{\mathrm{gi}}}{l}\left(n_{\mathrm{gi}}^{\mathrm{I}} - n_{\mathrm{gi}}^{\mathrm{II}} - n_{\mathrm{gi}}^{\mathrm{II}}\frac{eU_{\mathrm{I}}}{kT}\right) S_{\mathrm{b}} + R_{\mathrm{gf,i}} \exp\left(-\frac{eU_{\mathrm{I}}}{m_{\mathrm{g}} u_{\mathrm{s}}^2}\right) , \tag{4.45}$$

where the influence of the potential drop across Zone I (U_{I}) is also taken into account. The last term, where $R_{\mathrm{gf,i}}$ is the generation rate of ions from the fast neutrals, represents fast ions which are able to overcome the potential barrier in Zone I. The time-dependent mean free path of the ions is evaluated according to

$$\lambda_{\mathrm{gi}}^{\mathrm{I}} = \left[\sqrt{2}(n_{\mathrm{g}}^{\mathrm{I}}\sigma_{\mathrm{mg,ct}} + n_{\mathrm{m}}^{\mathrm{I}}\sigma_{\mathrm{mm,ct}}) + \frac{\nu_{\mathrm{ii,C}}}{\bar{v}_{\mathrm{g}}}\right]^{-1} , \tag{4.46}$$

where $\sigma_{\mathrm{mg,ct}}$ and $\sigma_{\mathrm{mm,ct}}$ are the cross sections for the process-gas-ion charge transfer onto gas or target material atoms, respectively. The Coulomb collision frequency $\nu_{\mathrm{ii,C}}$ is determined from the Spitzer's formula (Callen, 2006; Horwat and Anders, 2010)

$$\nu_{\mathrm{ii,C}} = \frac{(n_{\mathrm{gi}}^{\mathrm{I}} + n_{\mathrm{mi}}^{\mathrm{I}})^{3/2} e^4 \ln\Lambda}{12\pi^{3/2}\epsilon_0^2 (n_{\mathrm{gi}}^{\mathrm{I}} m_{\mathrm{g}} + n_{\mathrm{mi}}^{\mathrm{I}} m_{\mathrm{m}})^{1/2} (kT)^{3/2}} . \tag{4.47}$$

We use $\ln\Lambda = 10$ as this value of the Coulomb logarithm is convenient for low-temperature plasmas.

The fluxes of ions onto the chamber walls and onto the substrate are given by

$$G_{\mathrm{i,w}} = n_{\mathrm{gi}}^{\mathrm{II}} k_{\mathrm{bv}} \sqrt{\frac{kT_{\mathrm{e}}^{\mathrm{II}}}{m_{\mathrm{g}}}} (\tilde{S}_{\mathrm{gi,r}} + \tilde{S}_{\mathrm{gi,z}}) . \tag{4.48}$$

All fluxes of target material ions are given analogously.

Electrons The fluxes of electrons are used to determine the convective fluxes of energy (4.19) for the energy conservation equation (4.18). The parameter k_{w} depends on the EEDF through the relation (Lieberman and Lichtenberg, 2005, chap. 18.6)

$$k_{\mathrm{w}} = \frac{\int_0^\infty \varepsilon^{1.5} g_{\mathrm{e}}(\varepsilon)\mathrm{d}\varepsilon}{kT_{\mathrm{e}} \int_0^\infty \varepsilon^{0.5} g_{\mathrm{e}}(\varepsilon)\mathrm{d}\varepsilon} . \tag{4.49}$$

During the voltage pulse, the flux of thermalized electron onto the target is zero due to the high sheath potential. After the pulse, the electrons and ions are lost from the plasma volume mainly to chamber walls, which are much larger than the target. Therefore, the flux of electrons to the target after the pulse is negligible and for simplicity, it is set to zero. The flux of fast (secondary) electrons from the target is given by

$$E_{\mathrm{ef,t}} = -(1-r)(G_{\mathrm{i,t}}\gamma_{\mathrm{g}} + M_{\mathrm{i,t}}\gamma_{\mathrm{m}}) , \tag{4.50}$$

where γ_g and γ_m are the secondary electron emission coefficients induced by the process gas and the target material ions, respectively, and r is the recapture coefficient, defining the fraction of secondary electrons, that are almost immediately reabsorbed by the target (Buyle et al., 2003).

We assume that the magnetic induction at the interface between Zone I and Zone II is roughly parallel to this interface (in agreement with the model of Buyle et al. (2004)) and thus the electrons are well confined by the magnetic field in Zone I. Then the fast electrons lose almost all of their energy in Zone I and we may set $E_\mathrm{ef,b} = 0$, which means that there are no fast electrons in Zone II. The flux of thermalized electrons from Zone I to Zone II goes perpendicularly to the magnetic field lines and thus it can be modelled by a drift-diffusion equation in the form

$$E_\mathrm{b} = \frac{D_\mathrm{e}}{l}\left(n_\mathrm{e}^\mathrm{I} - n_\mathrm{e}^\mathrm{II} + n_\mathrm{e}^\mathrm{I}\frac{eU_\mathrm{I}}{kT_\mathrm{e}^\mathrm{I}}\right)S_\mathrm{b}\,. \tag{4.51}$$

In this equation, we use a general relation for the cross-field diffusion coefficient

$$D_\mathrm{e} = \frac{1}{\omega_\mathrm{ge}\tau_\mathrm{c}}\frac{kT_\mathrm{e}^\mathrm{I}}{eB}\,, \tag{4.52}$$

where the gyration-to-collision frequency ratio $\omega_\mathrm{ge}\tau_\mathrm{c}$ is a constant input parameter of the model.

The flux of thermalized electrons onto chamber walls is calculated directly from the condition of quasi-neutrality in Zone II in the form

$$E_\mathrm{w} = G_\mathrm{i,w} + M_\mathrm{i,w} - G_\mathrm{i,b} - M_\mathrm{i,b} + E_\mathrm{b}\,. \tag{4.53}$$

4.2.2 Plasma reactions

The most important plasma reactions in magnetron discharges result from binary particle collisions, which are described by a rate $R_c = n_{c1}n_{c2}K_c\tilde{V}_c$, see the third term of (4.14). Three types of electron–atom collisions are included in the model: ionization, excitation and elastic scattering. The ionization process generates ions from both the thermalized and fast neutral atoms. Excited states are not resolved by the model, but excitation and elastic collisions are taken into account in the calculation of electron energy losses due to collisions with neutral atoms.

The collision rate constants for electron–atom collisions depend on the electron energy distribution function. In magnetron discharges, the distribution differ significantly from the equilibrium Maxwellian distribution functions due to the fast (secondary) electrons which are emitted from the target and gain a high energy in the target sheath. In the model, the thermalized and fast electrons are distinguished and a way to calculate the collision rate constants for these two groups of electrons was devised.

For the case of thermalized electrons, the rate constants are calculated classically as

$$K(T_\mathrm{e}) = \left(\frac{2e}{m_\mathrm{e}}\right)^{0.5}\int_0^\infty \varepsilon^{0.5}\sigma(\varepsilon)g_\mathrm{e}(\varepsilon, T_\mathrm{e})\mathrm{d}\varepsilon\,, \tag{4.54}$$

where $\sigma(\varepsilon)$ is the cross-section of the respective collisional process. In this way the rate constants for the ionization of the process gas and the target material, $K_{\text{e-g,iz}}$ and $K_{\text{e-m,iz}}$, are calculated. The rate constant for the electron energy loss is calculated as

$$\mathcal{K}(T_{\mathrm{e}}) = \left(\frac{2e}{m_{\mathrm{e}}}\right)^{0.5} \int_0^\infty \varepsilon^{0.5}\eta(\varepsilon)\sigma(\varepsilon)g_{\mathrm{e}}(\varepsilon, T_{\mathrm{e}})\mathrm{d}\varepsilon\,, \tag{4.55}$$

where $\eta(\varepsilon)$ is the average energy lost during the collisional process by the incident electron with energy ε. The average energy loss in inelastic processes is given by the threshold energy of the process (i.e. the ionization or the excitation energy). In the case the total excitation cross section is a sum of several cross sections corresponding to excitations to different atomic levels, the average energy loss is given by a weighted average of the excitation energies. The average energy loss in elastic scattering collisions can be expressed as

$$\eta_{\mathrm{el}}(\varepsilon) = \frac{2m_{\mathrm{e}}m_{\mathrm{g}}}{(m_{\mathrm{e}}+m_{\mathrm{g}})^2}\frac{\sigma_{\mathrm{mt}}(\varepsilon)}{\sigma_{\mathrm{el}}(\varepsilon)}\varepsilon\,, \tag{4.56}$$

where m_{e} and m_{g} are the masses of the electron and the target atom, respectively, σ_{mt} is the momentum transfer cross section and σ_{el} is the elastic scattering cross section. In the simplified case of a hard-sphere collision, the fraction $\sigma_{\mathrm{mt}}/\sigma_{\mathrm{el}} = 1$.

The total rate constants for the electron energy lost by collisions with the process gas atoms is calculated as $\mathcal{K}_{\text{e-g}} = \mathcal{K}_{\text{e-g,iz}} + \mathcal{K}_{\text{e-g,ex}} + \mathcal{K}_{\text{e-g,el}}$. The rate constant for the collisions with the target material atoms, $\mathcal{K}_{\text{e-m}}$, is calculated analogously.

For the fast electrons, a stand-alone single particle Monte Carlo simulation (similar to that of Miranda et al. (1990)) is used to calculate the collisions of a secondary electron from the time it is emitted from the target with the energy eU_{s} until its energy drops below a threshold energy $\varepsilon_{\mathrm{thr}}$. It should be noted, that all electrons generated by the initial electron during its lifetime are followed in the same way. The process is repeated for a sufficient number of electrons, so that representative average characteristics are obtained. Three important parameters are recorded: (1) the average number of ionizations done by a single secondary electron, $N_{\text{ef-g,iz}}$, (2) the average total energy of the thermalized electrons generated by a single secondary electron, $\varepsilon_{\text{ef-g,th}}$, and (3) the average product of the secondary electron lifetime and the density of the target atoms, $n_{\mathrm{g}}\tau_{\text{ef-g}}$. Here, the symbols are written for the case of collisions with process gas atoms. It can be easily derived that the lifetime of a secondary electron is inversely proportional to the density of the target atoms. Therefore, the product $n_{\mathrm{g}}\tau_{\text{ef-g}}$ is independent of this density. The recorded parameters thus depend only on the sheath voltage, U_{s}, on the cross-sections for the three electron–atom collisions considered and on the threshold energy.

The threshold energy was set to $\varepsilon_{\mathrm{thr}} = 30\,\mathrm{eV}$ as in the simulation of Musschoot et al. (2008). We believe that this is a reasonable choice. With a higher value we would underestimate the ionization efficiency of the energetic electrons by transferring them to the thermalized group too soon. On the other hand, for energies of several tens of eV, Coulomb collisions become dominant, especially for high plasma densities, and cause a fast thermalization of the electrons. Our tests showed that a

variation of the threshold energy by 10 eV does not have a significant influence on the results of the model.

It should be reminded, that during the ionization and excitation of atoms, the fast electrons lose energy until they become thermalized and that they retain some of their initial energy as thermalized electrons. That is why we need to describe three processes connected with the ionization by secondary electrons: the ionization, the thermalization and the energy transfer to thermalized electrons. We introduce the collision rate constant for the thermalization of fast electrons by the collisions with process gas atoms as

$$K_{\text{ef-g,th}} = \frac{1}{\tau_{\text{ef-g}} n_{\text{g}}} , \tag{4.57}$$

the collision rate constant for the ionization of process gas atoms by fast electrons as

$$K_{\text{ef-g,iz}} = M \frac{N_{\text{ef-g}}}{\tau_{\text{ef-g}} n_{\text{g}}} \tag{4.58}$$

and the collision rate constant for the addition of energy to the thermalized electrons as

$$\mathcal{K}_{\text{ef-g}} = M \frac{\varepsilon_{\text{ef-g,th}}}{\tau_{\text{ef-g}} n_{\text{g}}} . \tag{4.59}$$

The coefficient M accounts for an increase in the number of ions generated by a fast electron due to creation of electron–ion pairs in the sheath, see Musschoot et al. (2008). The constant itself is given by the relation $M = 1 + 1 \times s^2$, where the sheath thickness s (in mm) is calculated from the collisionless Child-Langmuir law and the fitting constant 1 was estimated by a comparison with experimental waveforms. For the target material atoms, these rate constants can be rewritten in a straightforward manner.

Two types of collisions between atoms and ions are included in the model: elastic scattering and ion–atom charge transfer. The elastic collisions are included in the rate terms for the transfer of particles between the fast and the thermalized groups. The collision rate constant for the acceleration of atoms from the thermalized to the fast group is expressed as

$$K_{\text{m-g,ac}} = \sigma_{\text{mg}} u_{\text{s}} \left(1 - \frac{m_{\text{g}}}{m_{\text{g}} + m_{\text{m}}} \right) , \tag{4.60}$$

for an exemplary collision between a target material atom with mass m_{m} and velocity u_{s} and a stationary process gas atom with mass m_{g}, where it is assumed that the average momentum fraction $m_{\text{g}}/(m_{\text{g}}+m_{\text{m}})$ is transferred onto the stationary process gas atom in a hard-sphere collision. Here, σ_{mg} is the elastic collision cross-section between the process gas and the target material atoms. Conversely, the rate constant for the thermalization of fast target material atoms in a collision with thermalized process gas atoms can be expressed as

$$K_{\text{m-g,th}} = \sigma_{\text{mg}} u_{\text{s}} \frac{m_{\text{g}}}{m_{\text{g}} + m_{\text{m}}} . \tag{4.61}$$

Reaction	Cross section	Average electron energy loss (only electron–atom collisions)
e + G → 2e + G^+	$\sigma_{\mathrm{eg,iz}}(\varepsilon)$	$\eta_{\mathrm{eg,iz}}(\varepsilon)$
e + G → e + G^*	$\sigma_{\mathrm{eg,ex}}(\varepsilon)$	$\eta_{\mathrm{eg,ex}}(\varepsilon)$
e + G → e + G	$\sigma_{\mathrm{eg,el}}(\varepsilon)$	$\eta_{\mathrm{eg,el}}(\varepsilon)$
e + M → 2e + M^+	$\sigma_{\mathrm{em,iz}}(\varepsilon)$	$\eta_{\mathrm{em,iz}}(\varepsilon)$
e + M → e + M^*	$\sigma_{\mathrm{em,ex}}(\varepsilon)$	$\eta_{\mathrm{em,ex}}(\varepsilon)$
e + M → e + M	$\sigma_{\mathrm{em,el}}(\varepsilon)$	$\eta_{\mathrm{em,el}}(\varepsilon)$
G + G → G + G	σ_{gg}	
M + G → M + G	σ_{mg}	
M + M → M + M	σ_{mm}	
G + G^+ → G^+ + G	$\sigma_{\mathrm{gg,ct}}$	
M + G^+ → M^+ + G	$\sigma_{\mathrm{mg,ct}}$	
G + M^+ → G^+ + M	$\sigma_{\mathrm{gm,ct}}$	
M + M^+ → M^+ + M	$\sigma_{\mathrm{mm,ct}}$	

Table 4.5: Reactions included in the model. In the reaction description, e = electron, G = process gas atom and M = target material atom. The cross sections are denoted by σ and the average electron energy loss functions by η. For the electron–atom collisions, σ and η are functions of the electron energy ε.

Charge transfer collisions between neutral atoms and ions play an important role especially in Zone I, where large fluxes of sputtered particles interact with a high density plasma (Anders and Oks, 2009). The collision rate constant for the charge transfer between fast target material atoms and process gas ions is calculated as

$$K_{\mathrm{m\text{-}g,ct}} = \sigma_{\mathrm{mg,ct}} u_{\mathrm{s}} \,, \tag{4.62}$$

assuming the charge transfer cross section $\sigma_{\mathrm{mg,ct}}$ is independent of velocity. All the reactions included in the model are summarized in table 4.5.

4.3 Parameters of the model

In previous sections, the model equations and the terms for the transport and collisions of the model species were presented. In this section, the input parameters of the model will be summarized.

Three parameters describe specific plasma properties related to the fluid description of plasma: the EEDF of thermalized electrons, $g(\varepsilon)$, the electron cross-field transport parameter, $\omega_{\mathrm{ge}}\tau_{\mathrm{c}}$, and the temperature of ions and thermalized atoms, T. Typically, we use the Druyvesteyn EEDF, which can be written as

$$g(\varepsilon) = 0.565 kT_{\mathrm{e}}^{-1.5} \varepsilon^{0.5} \exp\left[-0.243 \left(\frac{\varepsilon}{kT_{\mathrm{e}}}\right)^2\right] . \tag{4.63}$$

Druyvesteyn-like EEDFs were detected in HiPIMS discharges during the initial part of a voltage pulse and after the pulse end (Gudmundsson et al., 2001; Pajdarová et al., 2009). During the high-density part of the pulse the Maxwell-like EEDFs with strongly reduced high-energy tail were recorded (Pajdarová et al., 2009), which can be also approximated by the Druyvesteyn EEDF. Then the dependent transport parameters are $k_{\mathrm{bv}} = 1.17$ and $k_{\mathrm{w}} = 1.80$, using (4.43) and (4.49), respectively. If not specified otherwise, we use the value $\omega_{\mathrm{ge}}\tau_{\mathrm{c}} = 16$ which corresponds to the Bohm diffusion regime (Chen, 1984). This means that the transport of electrons across the magnetic field is faster than predicted by a classical fluid theory, which is in agreement with experimental results (Rossnagel and Kaufman, 1987; Bohlmark et al., 2004; Brenning et al., 2009). The temperature of ions and thermalized atoms is set to $T = 300\,\mathrm{K}$.

The other model parameters can be divided into two groups: process input parameters and material parameters. The process input parameters describe the technological properties that are set by the designer or operator of the HiPIMS system. The geometry of the simulation volume is determined by the chamber radius, R, the target-to-substrate distance, L, the target diameter, d_{t}, and the substrate diameter, d_{s}, see figure 4.1. The complicated magnetic field is approximated by a single value, B, which represents a mean magnetic field induction in Zone I, see equations (4.51) and (4.52). The process gas pressure, p, determines the density of the process gas at steady-state no-discharge conditions, see (4.39). Although the model is able to calculate a steady-state of a continuous high-power discharge, it is primarily intended for HiPIMS discharges, so the target voltage is expected to represent periodic pulses. Then, the voltage pulse is specified by a time-evolution of the magnetron voltage, $U_{\mathrm{d}}(t)$, for the duration of one period T. An arbitrary voltage pulse can be used, but for simplicity, an ideally rectangular voltage pulse will be used frequently, see figure 4.4. The rectangular voltage pulse is given by a target voltage during the pulse, U_{d}, by a pulse duration, t_1, and by the pulse period, T, or a repetition frequency, f_{r}.

The material parameters are related to the process gas and the target material used for a specific simulation. The necessary material data for the model are: (1) sputtering yields of the target due to the impact of process gas and target material ions, Y_{g} and Y_{m} as functions of the target sheath voltage, respectively, see (4.24); (2) secondary electron emission coefficients, γ_{g} and γ_{m}, and the recapture coefficient, r, see (4.50); (3) surface binding energy of the target material, $\varepsilon_{\mathrm{sb}}$, see (4.28); and (4) cross-sections for the included collisional processes, see table 4.5. Note, that the cross sections for electron collisions are functions of electron energy.

4.4 Implementation and numerical solution

The complete set of model equations comprise of 16 non-linear ordinary differential equations (12 particle conservation equations for the process gas and target material ions, thermalized and fast atoms in both zones, see (4.14), 1 particle conservation

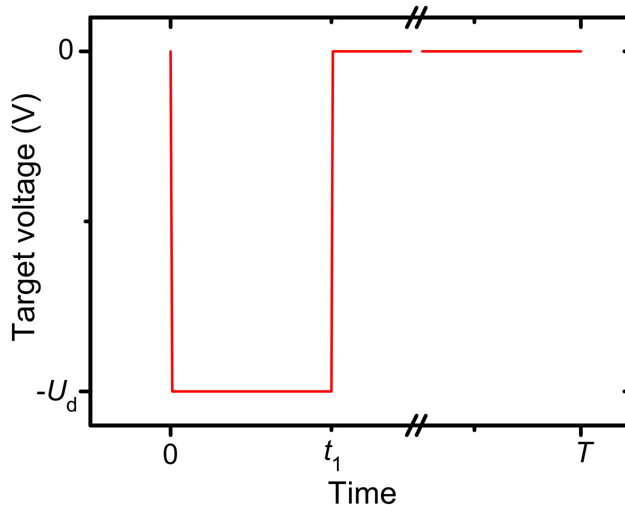

Figure 4.4: Schematic illustration of a rectangular voltage pulse which is used frequently as an input of the model. The parameters of the pulse are the target voltage, U_d, pulse length, t_1, and the pulse period, T.

equation for the fast electrons in Zone I, see (4.14), 2 energy conservation equations for thermalized electrons in both zones, see (4.18), and 1 equation for the Zone I potential, U_I, see (4.21)). The set of equations can be written in the general form

$$\frac{\mathrm{d}\boldsymbol{y}(t)}{\mathrm{d}t} = \boldsymbol{f}(t, \boldsymbol{y}(t)) \,, \tag{4.64}$$

where $\boldsymbol{y}(t) \in \mathbb{R}^{16}$ is a vector of the time-dependent model variables and $\boldsymbol{f}(t, \boldsymbol{y})$ is a vector function corresponding to the right-hand-sides of the 16 ordinary differential equations. The solution of the model is the time-evolution of the vector $\boldsymbol{y}(t)$, where $t \in \langle 0, T \rangle$. A stable discharge, which is obtained after several pulse periods, is characterized by the condition $\boldsymbol{y}(0) = \boldsymbol{y}(T)$, which is implemented as a convergence criterion

$$\max_i \frac{|y_i(T) - y_i(0)|}{|y_i(0)|} < \delta \,, \tag{4.65}$$

where y_i represents a component of the solution vector $\boldsymbol{y}$ and δ is the tolerance, which is set to 10^{-2} by default. It was tested that this tolerance is perfectly sufficient to obtain accurate and reproducible results.

The model is implemented in the Matlab 2010 environment which provides optimized routines for numerical solution of algebraic and differential equations. The solution procedure can be divided into the following steps.

1. **Load model input parameters and tables of collision rate constants**
   All input parameters for the calculation are loaded. The zone volumes, surface areas and the spatial distribution function integrals are calculated. The collision rate constants, which are calculated in advance and stored in tables, are

loaded. The collision rate constants for thermalized electrons, $K_{\text{e-g,iz}}$, $K_{\text{e-m,iz}}$, $\mathcal{K}_{\text{e-g}}$, $\mathcal{K}_{\text{e-m}}$, are tabulated as functions of the electron temperature in the range of $0 - 20\,\text{eV}$. The collision rate constants for fast electrons, $K_{\text{ef-g,th}}$, $K_{\text{ef-g,iz}}$, $\mathcal{K}_{\text{ef-g}}$ and $K_{\text{ef-m,th}}$, $K_{\text{ef-m,iz}}$, $\mathcal{K}_{\text{ef-m}}$, are tabulated as functions of the sheath voltage, U_{s}, in the range of $100 - 1500\,\text{V}$. During the solution of the model, the desired values are interpolated from these tables based on the current values of the electron temperature and the sheath voltage.

2. **Set initial conditions**
   As initial conditions $\boldsymbol{y}(0)$, we use typical plasma conditions in magnetron discharges, i.e. the initial process gas density given by the pressure, the initial plasma density of $10^{16}\,\text{m}^{-3}$ and the initial electron temperature of $2\,\text{eV}$. These initial conditions ensure that the model discharge is “ignited” when a sufficient target voltage is applied at the beginning of the first pulse. The converged results are independent of the initial conditions when those are set reasonably.

3. **Solve the model equations during one pulse period**
   The set of model equations (4.64) is solved for the duration of one period, providing the time-evolution of the solution vector $\boldsymbol{y}(t)$ in $t \in \langle 0, T \rangle$. We use the *ode15s* routine which uses a variable order solver based on numerical differentiation formulas. This solver provides the shortest computation time when compared to other solvers available in Matlab.

4. **Check convergence**
   If the convergence condition (4.65) is not satisfied, the initial state is set to the final state obtained at the end of the pulse, i.e. $\boldsymbol{y}(0) = \boldsymbol{y}(T)$, and another pulse period is solved, see step 3.

5. **Calculate discharge characteristics and save results**
   Once the convergence is reached, the time-evolution of the desired discharge characteristics are calculated from the solution $\boldsymbol{y}(t)$. These include the densities of particles in both zones, the electron temperature in both zones, target current, the fluxes of particles onto the target and substrate. From these, various time-averaged characteristics can be calculated, including the average target current in a pulse, the average target power density in a pulse and in a period, the average flux of the target material atoms and ions onto the substrate and the average deposition rate. These outputs are saved into text files which can then be processed for graphical visualisation of the results.

4.5 Discharge and deposition characteristics

After the solution of the model equations, the important discharge and deposition characteristics are calculated from the particle densities and fluxes. The quantities used frequently as the results of the model should be defined here beforehand.

The discharge current, i.e. the total current measured at the target, is given naturally by

$$I_\mathrm{d} = -e(G_\mathrm{i,t} + M_\mathrm{i,t} - E_\mathrm{f,t})\,. \tag{4.66}$$

The fraction of target material ions in the total ion flux onto the target

$$m_\mathrm{t} = \frac{M_\mathrm{i,t}}{G_\mathrm{i,t} + M_\mathrm{i,t}} \tag{4.67}$$

and the fraction of target material ions in the total ion flux onto the substrate

$$m_\mathrm{s} = \frac{M_\mathrm{i,s}}{G_\mathrm{i,s} + M_\mathrm{i,s}}\,. \tag{4.68}$$

The ionized fraction of the target material atoms in the flux onto the substrate is given by

$$\Theta = \frac{M_\mathrm{i,s}}{M_\mathrm{s} + M_\mathrm{f,s} + M_\mathrm{i,s}}\,. \tag{4.69}$$

To determine the direction of ion flow from Zone I, we define a parameter σ as the fraction of ion flux onto the target in the total ion flux leaving Zone I (see the link to the phenomenological model of Vlček and Burcalová (2010) presented in section 2.2.2), i.e.

$$\sigma_\mathrm{g} = \frac{-G_\mathrm{i,t}}{G_\mathrm{i,b} - G_\mathrm{i,t}} \quad \text{and} \tag{4.70}$$

$$\sigma_\mathrm{m} = \frac{-M_\mathrm{i,t}}{M_\mathrm{i,b} - M_\mathrm{i,t}}\,, \tag{4.71}$$

$$\tag{4.72}$$

where the signs correspond to the chosen direction convention (see figure 4.2) so that $\sigma > 0$.

To characterize the "continuous" properties of the pulsed discharge seen on the scale of many periods we average the above mentioned quantities over the pulse duration t_1 or over the period T. We define the average target current in a pulse

$$I_\mathrm{da} = \frac{1}{t_1}\int_0^{t_1} I_\mathrm{d}\mathrm{d}t\,, \tag{4.73}$$

the average target power density in a pulse

$$S_\mathrm{da} = \frac{4}{\pi d_\mathrm{t}^2 t_1}\int_0^{t_1} U_\mathrm{d} I_\mathrm{d}\mathrm{d}t\,. \tag{4.74}$$

and the average target power density in a period

$$\overline{S}_\mathrm{d} = \frac{4}{\pi d_\mathrm{t}^2 T}\int_0^{T} U_\mathrm{d} I_\mathrm{d}\mathrm{d}t\,. \tag{4.75}$$

Notice that the power densities are averaged over the whole target area. This is a common practise with experimental results where it is difficult to determine the racetrack area.

The average fraction of target material ions in the total ion flux onto the target in the pulse, m_{ta}, and in a period, $\overline{m}_{\mathrm{t}}$, is then obtained as

$$m_{\mathrm{ta}} = \frac{\int_0^{t_1} M_{\mathrm{i,t}} \mathrm{d}t}{\int_0^{t_1} (G_{\mathrm{i,t}} + M_{\mathrm{i,t}}) \mathrm{d}t} \tag{4.76}$$

and

$$\overline{m}_{\mathrm{t}} = \frac{\int_0^{T} M_{\mathrm{i,t}} \mathrm{d}t}{\int_0^{T} (G_{\mathrm{i,t}} + M_{\mathrm{i,t}}) \mathrm{d}t} \,, \tag{4.77}$$

respectively. The average values $\overline{m}_{\mathrm{s}}$, $\overline{\Theta}$, σ_{ga} and σ_{ma} are defined analogously by integrating separately the numerator and denominator of m_{s}, Θ, σ_{g} and σ_{m}, respectively, over the pulse length (σ_{ga} and σ_{ma}) or over the period ($\overline{m}_{\mathrm{s}}$ and $\overline{\Theta}$).

Finally, the average deposition rate, $\overline{a}_{\mathrm{D}}$, is defined as

$$\overline{a}_{\mathrm{D}} = \frac{1}{n_{\mathrm{f}} S_{\mathrm{s}} T} \int_0^T (M_{\mathrm{s}} + M_{\mathrm{f,s}} + M_{\mathrm{i,s}}) \mathrm{d}t \,, \tag{4.78}$$

where S_s is the substrate area and n_{f} is the atomic density of the growing film, which is assumed to be equal to the bulk density of the target material. An important quantity is the ratio $\overline{a}_{\mathrm{D}}/\overline{S}_{\mathrm{d}}$, called shortly as the *normalized deposition rate*, which measure the effectiveness of the sputtering process and enables us to compare the deposition rate of discharges with different target powers.

4.6 Material parameters for argon gas and copper target

The sputtering yields of copper induced by the impact of argon and copper ions, Y_{g} and Y_{m}, respectively, were calculated by the TRIM code (Ziegler et al., 2008) for the energy of the impacting ions in the range from 300 to 1000 eV. Analytical power law functions were then fitted to this data. Assuming that the ion energy is equal to the sheath voltage, we obtain

$$Y_{\mathrm{g}} = 0.056\, U_{\mathrm{s}}^{0.608} \,, \tag{4.79a}$$
$$Y_{\mathrm{m}} = 0.023\, U_{\mathrm{s}}^{0.724} \,, \tag{4.79b}$$

where U_{s} is in Volts.

For the secondary electron emission due to the impact of argon ions, we used the empirical formula $\gamma_{\mathrm{g}} = 0.016(E_{\mathrm{ig}} - 2E_{\mathrm{wm}})$ (Lieberman and Lichtenberg, 2005, eq. 9.3.4) where E_{ig} is the gas atom ionization energy and E_{wm} is the work function

of the target material. Taking $E_{\rm ig} = 15.82$ and $E_{\rm wm} = 4.4$ in agreement with Vlček and Burcalová (2010), we obtain

$$\gamma_{\rm g} = 0.112\,. \tag{4.80}$$

However, this empirical formula gives negative secondary electron emission coefficient for the impact of copper ions. Note that a sustained (gasless) self-sputtering of copper is possible (Posadowski, 1995; Andersson and Anders, 2008). In addition, production of doubly charged Cu^{2+} ions is very low even at high target power densities in magnetron sputtering discharges (Vlček et al., 2007a,b). Based on the work of Phelps and Petrovic (1999), we assume that the kinetic emission as well as the potential emission of highly excited Cu^{+} ions and possible Cu^{2+} ions contribute to the secondary electron emission from "technological" surfaces. Owing to the lack of data for the secondary electron emission due to the incident metallic ions in the literature, we used

$$\gamma_{\rm m} = s\gamma_{\rm g} \tag{4.81}$$

following the model of Vlček and Burcalová (2010). They showed that the values of the parameter s should be sufficiently high ($s > 0.5$) to obtain realistic results for the sputtering of copper. The influence of the parameter s on the model results will be analysed.

The effective secondary electron emission coefficients are also affected by the recapture of the fast (secondary) electrons on the target, r. This was estimated for each magnetic field configuration and pressure based on a single particle Monte Carlo simulation developed by us.

We use the copper atomic density $n_{\rm Cu} = 8.47 \times 10^{22}\,{\rm cm^{-3}}$ for the calculation of the deposition rate, see (4.78), assuming the film density is equal to the mass density of bulk copper ($8.94\,{\rm gcm^{-3}}$).

The cross sections for electron collisions with argon atoms (total excitation, ionization and elastic scattering) were taken from the compilation of Hayashi (2003). For ionization, the average energy loss is given by the ionization energy 15.82 eV. For excitation, the average energy loss is set to 12 eV. For elastic scattering, the average energy loss is calculated using (4.56).

The cross sections for electron collisions with copper atoms are taken from Bogaerts et al. (1998) (excitation and ionization) and from Trajmar et al. (1977) (elastic scattering). The total excitation cross section is a sum of 5 cross sections corresponding to excitations from the ground state to different excitation levels. Therefore the average energy loss equals to a weighted average of the corresponding excitation energies. The average energy loss during ionization is given by the ionization energy of 7.73 eV.

As mentioned in the previous section, these cross sections are used to precalculate the collision rate constants for the reactions of thermalized and fast electrons, see figure 4.5 and figure 4.6, respectively.

For the elastic scattering of argon atoms and for the charge transfer between argon atoms and ions, we used the data of Phelps (1991). Owing to the lack of data

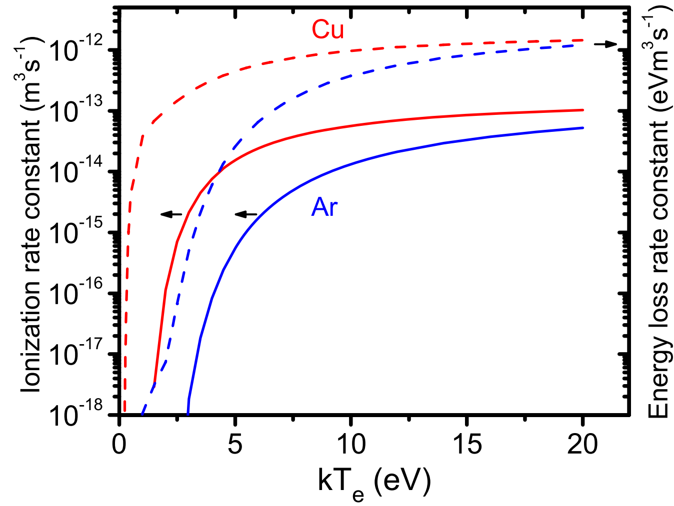

Figure 4.5: The rate constants for the ionization of argon (solid blue line) and copper (solid red line) atoms by thermalized electrons and the rate constants for the loss of energy of thermalized electrons by collisions with argon (dashed blue line) and copper (dashed red line) atoms as functions of the electron temperature.

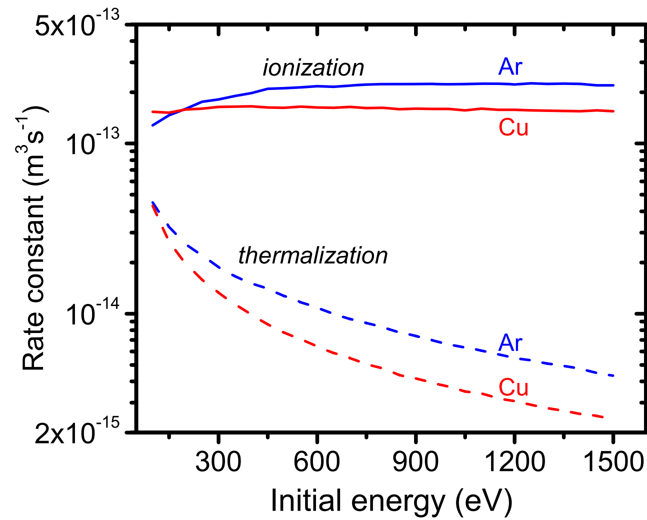

Figure 4.6: The rate constants for the ionization of argon (solid blue line) and copper (solid red line) atoms by fast electrons and the rate constants for the thermalization of fast electrons by collisions with argon (dashed blue line) and copper (dashed red line) atoms as functions of the initial energy of fast electrons.

for copper, we used the hard-sphere approximation for the elastic scattering of copper on argon atoms and between copper atoms. The cross sections for the charge transfer between argon ions and copper atoms and between copper ions and argon atoms were calculated using (3.4.31) in Lieberman and Lichtenberg (2005). The cross section for the charge transfer between copper atoms and ions was taken from Smirnov (2000). In all cases we assumed the relative energy of the colliding atoms in the order of a few eV, which is a typical energy of the sputtered target material atoms. This gives the values $\sigma_{\mathrm{gg}} = 10^{-19}\,\mathrm{m}^2$, $\sigma_{\mathrm{mg}} = 1.3 \times 10^{-19}\,\mathrm{m}^2$, $\sigma_{\mathrm{mm}} = 2.3 \times 10^{-19}\,\mathrm{m}^2$, $\sigma_{\mathrm{gg,ct}} = 6{\times}10^{-19}\,\mathrm{m}^2$, $\sigma_{\mathrm{mg,ct}} = 10{\times}10^{-19}\,\mathrm{m}^2$, $\sigma_{\mathrm{gm,ct}} = 0\,\mathrm{m}^2$ and $\sigma_{\mathrm{mm,ct}} = 16{\times}10^{-19}\,\mathrm{m}^2$.

5 Results and discussion

The results of the model are organized into 4 sections which correspond to the results published in the papers [I–IV]. The first section deals mainly with the validation of the model for two different HiPIMS systems. Target current waveforms, plasma densities and electron temperatures calculated by the model are compared with experimental measurements. In the second section, the effect of an increasing target power density achieved by increasing the target voltage is studied. The model input parameters were chosen to correspond to the system used by Anders et al. (2007) who measured the target current waveforms for a wide range of target voltages. The calculated target current waveforms are compared to experimental ones and the calculated composition of the discharge plasma is analysed. In the third section, the effect of the magnetic field strength, the voltage pulse length and shape, and the repetition frequency is studied. An emphasis is given to the relations between the process input parameters and the deposition rate and the ionized fraction of the target material atoms in the flux onto the substrate. In the final section, the results of the non-stationary model are compared to the steady-state phenomenological model of Vlček and Burcalová (2010). This comparison explains and quantifies the most important processes influencing the transport and ionization of sputtered target material atoms in a HiPIMS discharge. Especially, the effect of the magnetic field on the return of ionized target material atoms onto the target is discussed.

5.1 Validation of the model results for copper

For the validation of the model, the experimental results from two different HiPIMS systems were chosen for comparison: Pajdarová et al. (2009), denoted A, and Gudmundsson et al. (2009), denoted B. For the summary of the process parameters, see table 5.1. In both cases, time-resolved measurements of the electron density and the electron temperature were carried out at the distances from the magnetron target of 100 mm in the case A and of 80 mm in the case B. In the case A, 200 μs pulses with constant target voltages of 800 V and 560 V and a repetition frequency of 1 kHz were used. The argon pressure was fixed at 1.0 Pa. In the case B, two different pressures, 0.40 Pa and 2.67 Pa, were used. The voltage at the beginning of the pulse was 1000 V, but the power supply was unable to retain this value for the entire pulse duration, so the voltage decreased during the pulse to 250 V when the pressure was 2.67 Pa and to 400 V when the pressure was 0.40 Pa. The measured target voltage waveforms, which are not shown here, were used as an input parameter of the model.

The voltage pulse duration ranged from 80 to 90 μs (depending on the pressure) and the repetition frequency was 50 Hz.

5.1.1 Discharge current

The comparison of target current waveforms for the case A is shown in figure 5.1. Due to the constant target voltage and quite a long pulse duration, the discharge current reached a steady state during the pulse. In the left panel of figure 5.1, we show the experimental waveforms for both values of the target voltage, 560 and 800 V, and the calculated waveforms for two values of the parameter s, determining the secondary electron emission due to the impact of copper ions, see (4.81). The effect of s is strong especially for the high power case ($U_\mathrm{d} = 800\,\mathrm{V}$) which suggests that in this case there is a high fraction of copper ions in the flux to the target. When the parameter s increases, the ability of the discharge to be sustained in the self-sputtering mode is promoted and the target current evolves to a higher peak value. Comparing the shapes of the calculated and the experimental waveforms, we can conclude that the value of the parameter s lies in the range between 0.5 and 0.7.

The right panel of figure 5.1 shows the effect of the recapture coefficient r on the calculated target current while the parameter s had a fixed value of 0.6. The recapture coefficient r determines the overall effectiveness of the secondary electron emission, regardless of the composition of the ion flux to the target, see (4.50). It can be seen that a small change in r (increase by 0.05) has a significant effect on the peak target current (30% decrease). This is due to the fact that the secondary electrons have a high energy and they are the main source of ionization despite their low number compared to the thermalized ones. We can see that the shapes of the calculated waveforms are very similar to those experimentally recorded. For the

	A	B
Model volume (radius $\times$ length)	250×100 mm	225×200 mm
Target diameter	100 mm	150 mm
Target material	Cu	Cu
Argon pressure	1.0 Pa	0.40 and 2.67 Pa
Magnetic field	370 G	300 G
Target voltage	800 and 560 V	$1000 \to \sim 300$ V
Pulse length	200 μs	$80 - 90$ μs
Repetition frequency	1 kHz	50 Hz

Table 5.1: Process input parameters used for the model validation. The case A corresponds to the work of Pajdarová et al. (2009) and the case B corresponds to the work of Gudmundsson et al. (2009). In the case B, the voltage was decreasing during the pulse and the final value varied with the argon pressure.

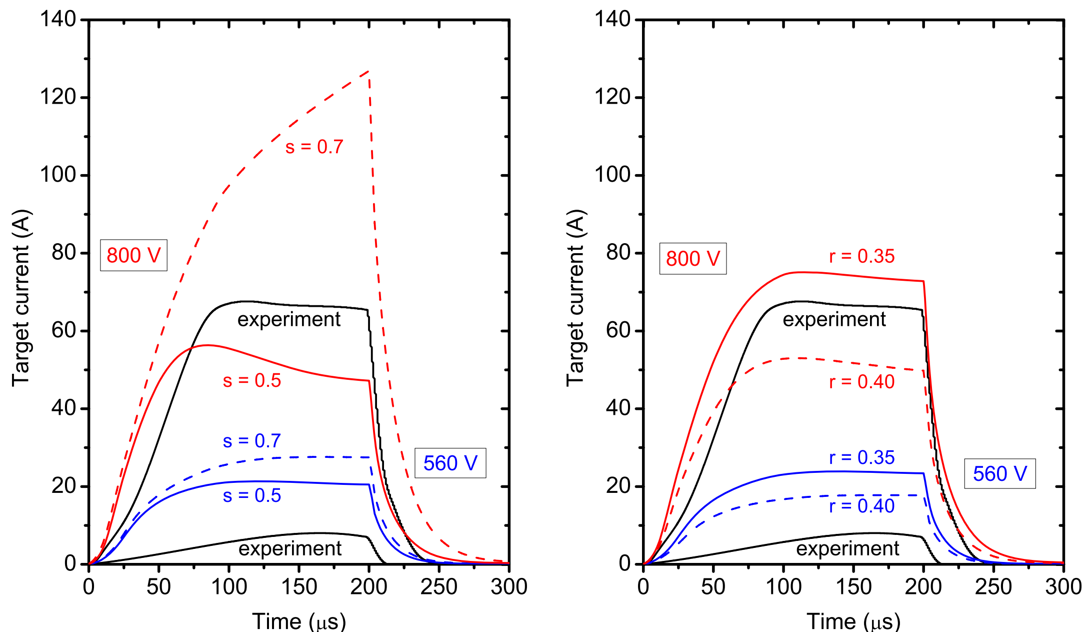

Figure 5.1: Comparison of the target current waveforms calculated by the model with the experimental results obtained by Pajdarová et al. (2009) (the case A) for the target voltages of 800 V (red lines) and 560 V (blue lines). The sensitivity of the model results to the parameter s (determining the secondary electron emission coefficient due to the impact of target material ions) with $r = 0.35$ is shown in the left panel. The sensitivity of the model results to the secondary electron recapture coefficient r with $s = 0.6$ is shown in the right panel.

high power case, the peak current estimated by the model is in a good agreement with experiment. For the low power case ($U_{\mathrm{d}} = 560\,\mathrm{V}$) the calculated peak current overestimates the real value. This is probably caused by the underestimation of the values of $r = 0.35$ and 0.40 used in our calculations for this case, when a lower plasma density above the target racetrack results in a prolongation of the electron mean free path leading to a higher recapture coefficient.

The comparison of target current waveforms for the case B is shown in figure 5.2, where also the influence of the secondary electron recapture coefficient r is shown. In this case we did not have a detailed information about the magnetic field configuration used in the experiments, so we estimated the basic values of the recapture coefficient r to be 0.15 and 0.05 for the pressure of 0.40 and 2.67 Pa, respectively. Then r is increased by 0.05 to see the sensitivity. We expect the values to be lower than in the previous case due to a larger target diameter. Also, the recapture coefficient should decrease with an increasing pressure. For both values of the argon pressure, the experimental and calculated target current waveforms follow the same trend. The target current rises at the beginning of the pulse, reaching a peak value and then decreases. This is due to the fact that the decrease of the target voltage

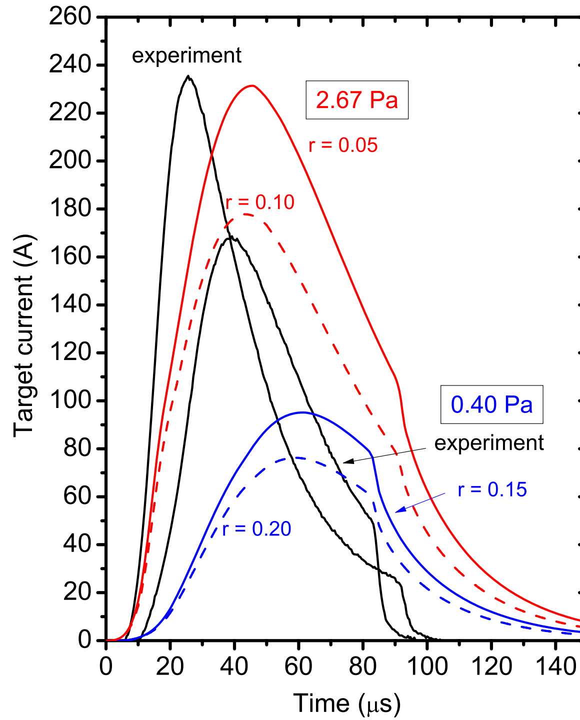

Figure 5.2: Comparison of the target current waveforms calculated by the model with the experimental results obtained by Gudmundsson et al. (2009) (the case B) for the gas pressures of 2.67 Pa (red lines) and 0.40 Pa (blue lines). The sensitivity of the model results to the recapture coefficient r is shown. The parameter $s = 0.7$.

during the pulse (as was the case for this experimental setup) does not allow to sustain the discharge in the high current regime. After an increase in the working gas pressure, the peak of the target current is higher and occurs sooner in the pulse. This trend is also predicted by the model and is explained by the higher initial argon density, which enables a faster ionization and thus an intensive sputtering of the target and an enhancement of secondary electron emission.

5.1.2 Electron density and temperature

Figure 5.3 shows the time evolution of the electron densities predicted by the model for the case A. Very high plasma densities are obtained, up to $10^{20}\,\mathrm{m}^{-3}$ for the high power case ($U_\mathrm{d} = 800\,\mathrm{V}$) and $3 \times 10^{19}\,\mathrm{m}^{-3}$ for the low power case ($U_\mathrm{d} = 560\,\mathrm{V}$), in Zone I. In the lower part of the figure, the electron densities measured at the substrate position (100 mm from the target) are compared with the electron densities predicted by the model for the same position in Zone II. As can be seen, the calculated densities, two orders of magnitude lower than those for Zone I, are in a very good agreement with the experimental data. The model also correctly predicts relatively high initial electron densities at the pulse beginning ($10^{17}\,\mathrm{m}^{-3}$ for

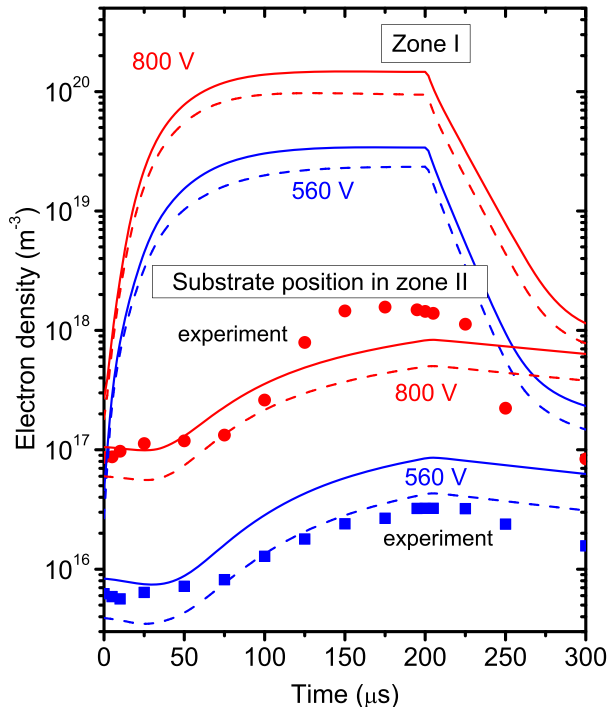

Figure 5.3: Time evolutions of the electron density in Zone I and at a substrate position (100 mm from the target) in Zone II calculated for the target voltages of 800 V (red lines) and 560 V (blue lines) under the experimental conditions of Pajdarová et al. (2009) (the case A). The experimental values measured at the substrate position are also shown for comparison. The sensitivity of the model results to the secondary electron recapture coefficient r is presented for $r = 0.35$ (solid lines) and $r = 0.40$ (dashed lines). The parameter $s = 0.6$.

$U_\mathrm{d} = 800\,\mathrm{V}$ and $10^{16}\,\mathrm{m}^{-3}$ for $U_\mathrm{d} = 560\,\mathrm{V}$), which are caused by the high repetition frequency of the voltage pulses (1 kHz in this case) preventing a significant decay of afterglow plasma.

Figure 5.4 shows the time evolution of the electron densities predicted by the model for the case B. Again, very high plasma densities in Zone I (up to $10^{20}\,\mathrm{m}^{-3}$) are obtained. Although the peak densities are comparable to the case A, the target currents in previous figures are higher due to the larger diameter of the target (150 mm in this case). In the lower part of the figure, the electron densities (measured at 80 mm from the target) are compared with the electron densities calculated by the model for the same position in Zone II. We can see a very good agreement especially during the pulse, when the density is rising. After the pulse, the calculated decrease of the electron density is slower than the measured one, which may be caused by the particle averaging over the large volume of Zone II. Nevertheless, one can notice that the decrease of the plasma density after the pulse is slightly slower for the high pressure case ($p = 2.67\,\mathrm{Pa}$). This is a direct consequence of the

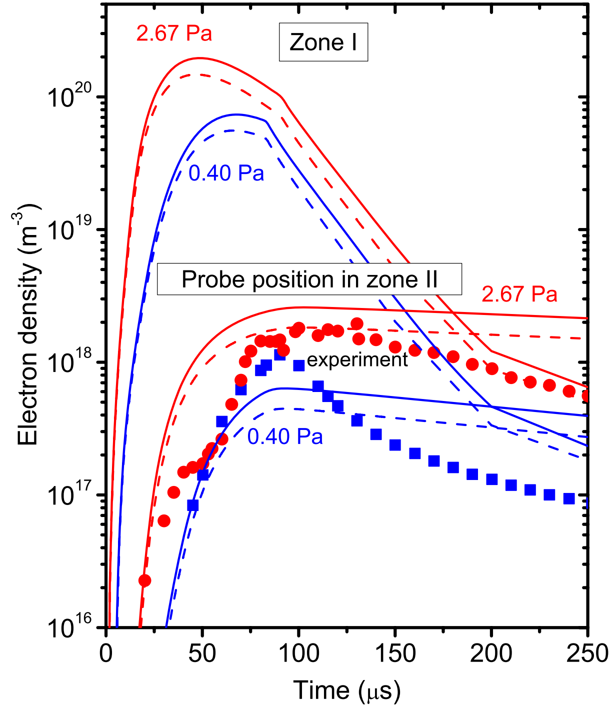

Figure 5.4: Time evolutions of the electron density in Zone I and at a probe position (80 mm from the target) in Zone II calculated for the gas pressures $p = 2.67\,\mathrm{Pa}$ (red lines) and $p = 0.40\,\mathrm{Pa}$ (blue lines) under the experimental conditions of Gudmundsson et al. (2009) (the case B). The experimental values measured at the probe position are shown for comparison. The sensitivity of the model results to the secondary electron recapture coefficient r is presented for $r = 0.05$ (solid lines) and $r = 0.10$ (dashed lines) at $p = 2.67\,\mathrm{Pa}$, and for $r = 0.15$ (solid lines) and $r = 0.20$ (dashed lines) at $p = 0.40\,\mathrm{Pa}$. The parameter $s = 0.7$.

higher pressure, when the collisions with argon gas slow down the diffusion of the plasma to the walls. In comparison with the case A, the repetition frequency is much lower (50 Hz in this case), which results in a significant decay of the electron density during the pause between the pulses, and consequently, in a relatively low electron density at the pulse beginning.

Figure 5.5 shows the calculated time evolution of the electron temperatures in both zones for the case A. The electron temperature measured at 100 mm from the target is shown for comparison as well. As can be seen, the calculated electron temperature in Zone I rises at the beginning of the pulse and then decreases to a value of 0.75 eV for the low power case ($U_\mathrm{d} = 560\,\mathrm{V}$) and to a value of 0.5 eV for the high power case ($U_\mathrm{d} = 800\,\mathrm{V}$). The lower electron temperatures obtained for the high power case can be explained by the higher density of copper atoms, which cool the electrons during frequent excitation and ionization collisions with the threshold energies of only 1.39 eV for excitation and 7.73 eV for ionization. The

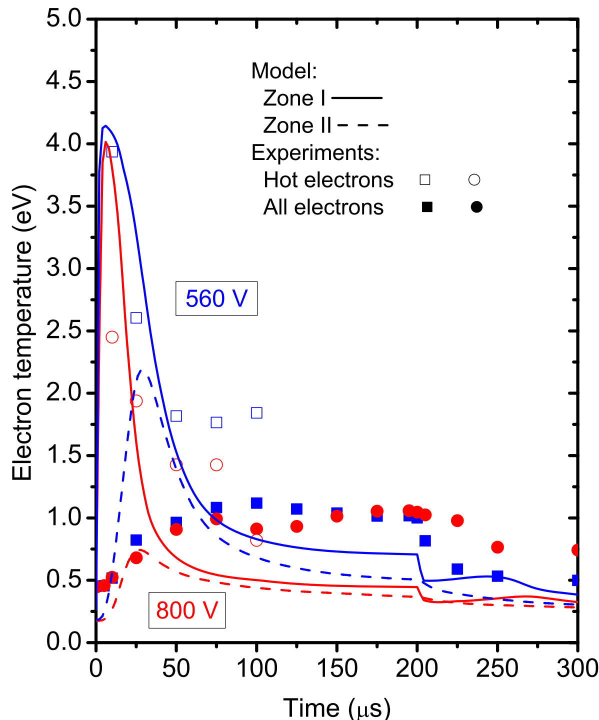

Figure 5.5: Time evolutions of the electron temperature in Zone I (solid lines) and Zone II (dashed lines) calculated for the target voltages $U = 800\,\mathrm{V}$ (red lines) and 560 V (blue lines) under the experimental conditions of Pajdarová et al. (2009) (the case A). The experimental values measured at the substrate position (100 mm from the target) are shown for comparison (the full and empty symbols represent the electron temperature and the temperature of hot electrons, respectively). The secondary electron recapture coefficient $r = 0.35$ and the parameter $s = 0.6$.

calculated temperature of thermalized electrons in Zone I corresponds well with the measured temperature of hot electrons at the beginning of the pulse. These hot electrons with very small density originate from the thermalized electrons in the target vicinity, which propagate almost without collisions along the straight magnetic field lines at the discharge axis to the substrate, where they are registered by the probe. The calculated electron temperature in Zone II follows a trend similar to the electron temperature in Zone I, but the initial peak is lower and occurs later in the pulse. As mentioned above, a relatively high density of low-temperature electrons remains in the discharge volume until the beginning of the next pulse. We suggest that their heat capacity causes the slower increase in the calculated electron temperatures in Zone II. On the other hand, the model assumes that the electron temperature is constant in Zone II for a given time, which corresponds to an immediate heat propagation over the whole zone volume. In the real discharges, the heat propagation to the probe distance (100 mm from the target) is expected to be slower, so no initial peak appears in the measured electron temperatures.

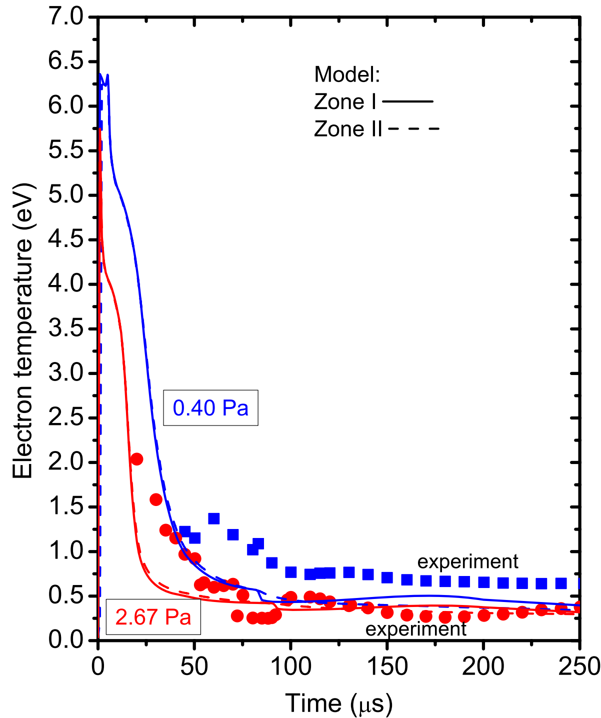

Figure 5.6: Time evolutions of the electron temperature in Zone I (solid lines) and Zone II (dashed lines) calculated under the experimental conditions of Gudmundsson et al. (2009) (the case B). The experimental values measured at the probe position (80 mm from the target) are shown for comparison. The secondary electron recapture coefficient $r = 0.05$ for the pressure $p = 2.67\,\mathrm{Pa}$ and $r = 0.15$ for the pressure $p = 0.40\,\mathrm{Pa}$. The parameter $s = 0.7$.

Figure 5.6 shows the calculated time evolution of the electron temperatures in both zones for the case B. Again, the model predicts a peak of the electron temperature at the beginning of the pulse followed by a decrease to and saturation at values below 1 eV. The model results agree well with the experimental data, where the same trend is observed. In comparison to the previous case, the electron temperatures in both zones are very close. This is explained by the fact that there are almost no electrons at the beginning of the pulse in the discharge volume (recall the low repetition frequency), so the average electron temperature in Zone II is close to the energy of electrons coming from Zone I. In this case, the electron transport dominates over the ionization.

5.1.3 Conclusions

The model results were compared with experimental data for two different HiPIMS systems. It was found that the target current is very sensitive to the secondary electron emission yields and to the secondary electron recapture coefficient. The

calculated target currents, electron densities and electron temperatures are in a good agreement with experimental results, taking into account the spatial approximations of the model. The model also correctly reproduces the trends with increasing target voltage and process gas pressure.

5.2 Effect of the target power density

We use the model to simulate the HiPIMS experiments of Anders et al. (2007) who measured target current waveforms for a wide range of target voltages. We show the comparison of the measured target current waveforms with the model calculations and analyse the effect of the increasing target power density on the plasma composition and on the composition of the particle fluxes onto the target and substrate. We discuss the role of several input parameters on the model results and confront these with known experimental results.

In agreement with the parameters of the experiment, we set the target diameter $d_\mathrm{t} = 50\,\mathrm{mm}$ and the argon pressure $p = 1.8\,\mathrm{Pa}$. We lack detailed information about the magnetic field distribution of the magnetron. However, the reported magnetic field at the centre of the target (640 G) helped us estimate the average value in Zone I used in the model, $B = 350\,\mathrm{G}$, and the recapture coefficient, $r = 0.2$. The target–substrate distance was set to the reported distance between the target and the ion collector, $L = 200\,\mathrm{mm}$. The rectangular voltage pulses were 400 μs long and the amplitude varied from 500 to 960 V. The repetition frequency was 50 Hz. We set $s = 0.7$ as the basic value in this study and we discuss the effect of a possible change of this value.

5.2.1 Target current – voltage dependences

Figure 5.7 shows the target current waveforms calculated by the model and the experimental waveforms measured by Anders et al. (2007) for the target voltages of 550 V (blue lines) and 900 V (red lines). These values were chosen to represent a discharge with a relatively low and a relatively high target voltages. The calculated

Model volume (radius × length)	150 × 200 mm
Target diameter	50 mm
Target material	Cu
Argon pressure	1.8 Pa
Magnetic field	350 G
Target voltage	$500 - 960$ V
Pulse length	400 μs
Repetition frequency	50 Hz

Table 5.2: Model process input parameters used in the study of the effect of the target power density.

target current waveforms for these two cases and for the basic set of input parameters ($\omega_{ge}\tau_c = 16$, $r = 0.2$, $s = 0.7$) are in a good agreement with the experimental waveforms. For the higher target voltage, we observe a current overshoot at the beginning of the pulse in both the model and the experimental results.

The sensitivity of the target current to the parameter $\omega_{ge}\tau_c$, determining the electron cross-field diffusion coefficient is also shown in the left panel of figure 5.7. Lowering the parameter from the Bohm value of $\omega_{ge}\tau_c = 16$ to 10 leads to a decrease in the calculated target current roughly 2 times for the target voltage of 900 V and roughly 1.3 times for the target voltage of 550 V. The decrease in $\omega_{ge}\tau_c$ means a loss in the magnetic confinement of electrons (similarly to a decrease in the magnetic induction B) which leads to the decrease of the potential drop in Zone I, U_I, determining the electric field necessary to balance the flux of electrons and ions from Zone I, see (4.21). This is in agreement with the measurements of Mishra et al. (2010). Consequently, the flux of ions from Zone I to Zone II increases and the target current decreases when the target voltage is kept constant. For the target voltage of 900 V, there are more target material ions generated from the fast sputtered atoms, whose flux to Zone II is significantly influenced by the Zone I potential, see (4.45). Therefore the decrease in target current is more pronounced for the higher voltage.

The right panel of figure 5.7 shows the sensitivity of the target current to the secondary electron recapture coefficient r and to the s parameter. A small increase in the recapture coefficient or a decrease in the parameter s results in a decrease of the target current reached in the long steady state of the discharge, which is due to the lower amount of secondary electrons able to ionize the neutral atoms. We see from figure 5.7 that for all the used input parameters, the model predicts qualitatively the same evolution of the target current, differing only in the steady-state current values which are quite sensitive to the input parameters, especially for high target voltages.

The left panel of figure 5.8 shows the target current waveforms calculated for the target voltages between 500 and 960 V with the input parameters $\omega_{ge}\tau_c = 16$, $r = 0.2$ and $s = 0.7$. The target current waveforms are in a good agreement with the experimental waveforms for the target voltages higher than 550 V. For the target voltage of 500 V, a discrepancy between the measured and calculated target current can be seen. In the work of Anders et al., a transition between a low and a high current regime of the discharge is found around a threshold value of 530 V. This behaviour is explained by a strong rarefaction of the process gas and by the inability of the target material to sustain the discharge with the sub-threshold voltage. Although the gas rarefaction is calculated by the model, the simulated discharge is sustained with a relatively high target current by the combination of argon and copper ions even for the target voltage of 500 V. We believe that a particle simulation calculating spatial details of the rarefied gas and of the target material densities, together with their effect on the ionization by secondary electrons in front of the target, is necessary to fully explain the measured behaviour.

The agreement of the steady-state current values for the target voltages higher than 550 V is also visible in the average target current–voltage characteristics shown

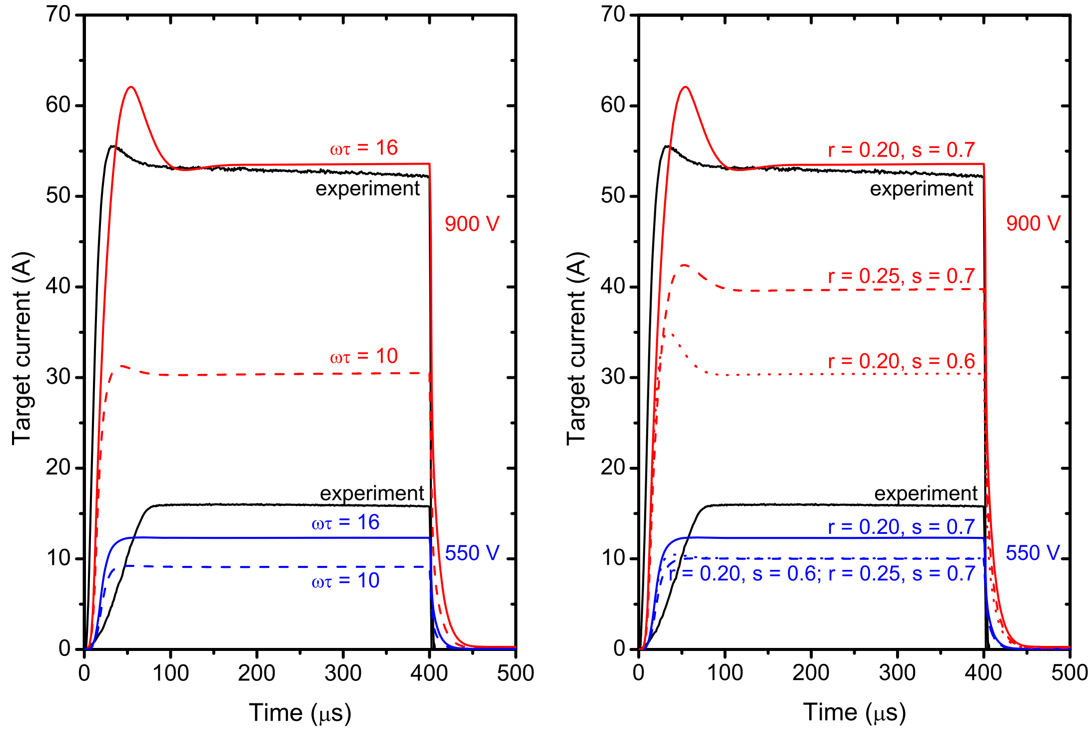

Figure 5.7: Comparison of the target current waveforms calculated by the model with the experimental waveforms obtained by Anders et al. (2007) for the target voltages of 550 V (blue lines) and 900 V (red lines). The sensitivity of the model results to the parameter $\omega_{ge}\tau_c$, determining the electron cross-field diffusion coefficient, with $r = 0.20$ and $s = 0.7$ is shown in the left panel. The sensitivity of the model results to the secondary electron recapture coefficient r and the parameter s, determining the secondary electron emission coefficient due to the impact of target material ions, with $\omega_{ge}\tau_c = 16$ is shown in the right panel.

in the right panel of figure 5.8. The experimental average current dependence exhibits a prominent step at the threshold (530 V), whereas the calculated average target current dependence follows a smooth decrease even for lower target voltages. A power law dependence of the average target current in a pulse on the target voltage was fitted to the calculated curve. We obtained the relation $I_{da} \propto U_d^{3.1}$. The calculated average target currents in a pulse and the corresponding average target power densities in a pulse are summarized in table 5.3.

5.2.2 Densities of the sputtered material and the discharge gas particles

Figure 5.9 shows the time evolution of the calculated ion and atom densities in both zones for the target voltage of 550 V, corresponding to the average target power

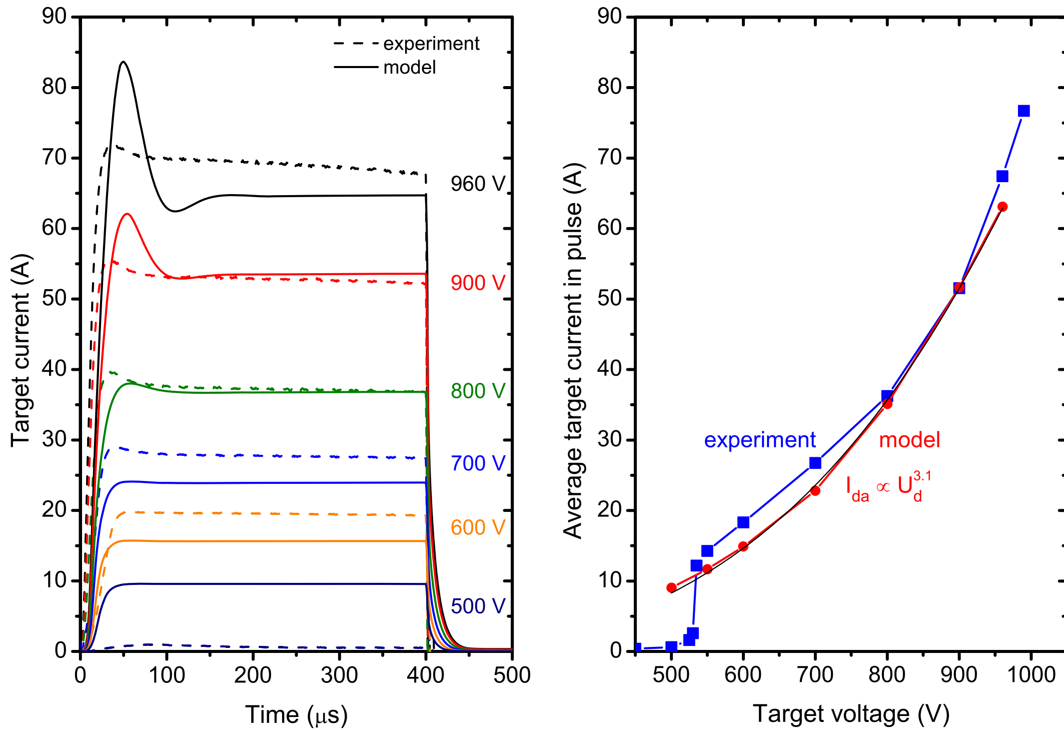

Figure 5.8: Comparison of the target current waveforms calculated by the model (left panel) and the average target currents in a pulse, I_{da}, calculated by the model (right panel) with the experimental values obtained by Anders et al. (2007). A power law relation between the target voltage and the average target current in a pulse was fitted to the calculated values. The parameter $\omega_{\mathrm{ge}}\tau_{\mathrm{c}} = 16$, the recapture coefficient $r = 0.20$ and the parameter $s = 0.7$.

density of 327 Wcm^{-2} in a pulse. In Zone I, the initial argon density corresponding to the pressure of 1.8 Pa is rarefied by the flux of the sputtered copper atoms during the pulse. Due to the low maximum target current (12 A), the sputtering of the target is not very intensive and the maximum density of the copper atoms in Zone I (1.3×10^{20} m^{-3}) is lower than the argon density. However, the density of copper ions in Zone I is slightly higher than the density of argon ions. This is caused mainly by the much lower ionization energy of copper compared to argon. In Zone II, we present two curves for each particle species, the evolution of the maximum densities corresponding to the interface between Zone I and Zone II (solid lines), and the densities at the substrate position of 200 mm from the target (dashed lines). In Zone II, the gap between the copper and argon ion density is markedly higher, which is mainly due to two processes. First, although the equations for argon and copper ions are exactly analogous, the flux of copper ions from Zone I to Zone II is larger compared to the flux of gas ions. This can be explained by the fact that there is an intensive flux of fast copper atoms sputtered from the target and a large

U (V)	I_{da} (A)	S_{da} (Wcm^{-2})
500	9.0	230
550	11.7	327
600	14.9	455
700	22.8	813
800	35.1	1430
900	51.7	2370
960	63.1	3080

Table 5.3: The calculated average target current in a pulse, I_{da}, and average target power density in a pulse, S_{da}, corresponding to the input target voltage, U_{d}.

fraction of the copper ions is created from these fast atoms. Consequently, the last term of (4.45) is higher for copper ions than for argon ions. This result is supported by the observation of Thompson-like high energy tails in the ion energy distribution functions of the metal ions (Vlček et al., 2007a; Hecimovic and Ehiasarian, 2009; Kudláček et al., 2008). Second, the charge transfer between sputtered copper atoms and argon ions contribute to the generation of copper ions at the expense of argon ions. The reverse process is highly unlikely due to the big difference in argon and copper ionization energies. In general, the evolution of copper atom density in Zone II is given by a superposition of two dependences, corresponding to the two particle groups (fast and thermalized). The contribution of the fast atoms is visible in the solid curve during the pulse duration when the flux of the fast sputtered atoms reaching Zone II is high. Due to the relatively high pressure of 1.8 Pa, most of these atoms are thermalized in Zone II by collisions with argon atoms and their contribution to the overall copper density is not visible in the dashed curve.

Figure 5.10 shows the time evolution of the calculated ion and atom densities in both zones for the target voltage of 900 V, corresponding to the average target power density of 2370 Wcm^{-2} in a pulse. In comparison to the previous case, we can see a significant increase in copper atom and ion densities corresponding to the increased sputtering flux and plasma density. Due to the high plasma density, the effect of the charge transfer collisions is very important in this case. The charge transfer between argon ions and sputtered copper atoms is the dominant process responsible for the pronounced decrease of argon ion density after the initial peak at about 30 μs. Due to the intensive ionization and thermalization of fast copper atoms in the dense plasma in Zone I, only 25 % of the sputtered copper atoms reach Zone II. Consequently, the flux of target material to Zone II is dominated by copper ions leading to the fact that the density of copper ions is higher than the density of copper atoms in Zone II (in contrast to the previous case) and the degree of ionization of the copper atoms reaches a maximum of 65 %.

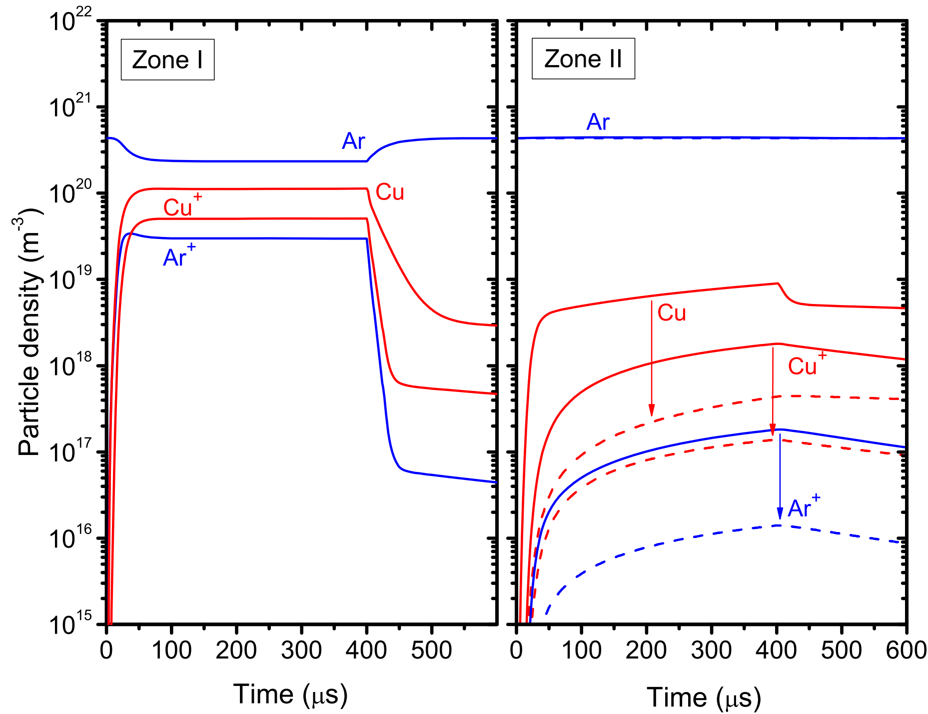

Figure 5.9: Time evolutions of the particle densities in Zone I and Zone II calculated for the target voltage of 550 V under the experimental conditions of Anders et al. (2007). The decrease in densities from the maximum values in Zone II to the values at the substrate position of 200 mm from the target is shown by arrows. The parameter $\omega_{\mathrm{ge}}\tau_{\mathrm{c}} = 16$, the recapture coefficient $r = 0.20$ and the parameter $s = 0.7$.

5.2.3 Discharge and deposition characteristics

Figure 5.11 shows time evolutions of the fractions of target material ions in the total ion fluxes onto the target and substrate, m_{t} and m_{s}, respectively, and of the ionized fraction of target material atoms in the flux onto the substrate, Θ, calculated by the model for the target voltages of 550 V and 900 V. The fraction of copper ions in the ion flux onto the target is close to zero at the beginning of the pulse because argon ions are always generated faster from the present argon atoms. As the target current increases, copper atoms are sputtered and ionized, which leads to the increase in m_{t}. Thus the role of the target material self-sputtering gradually increases during the plasma build-up phase. For the target voltage of 550 V, m_{t} saturates at 57 %. For the target voltage of 900 V, m_{t} reaches 92 %. Due to the already mentioned faster transport of copper ions into Zone II and the charge transfer from argon ions to copper ions in Zone II, the fraction of copper ions in the total ion flux onto the substrate, m_{s}, is always larger than m_{t} during the pulse. After the pulse, the ion densities in the small Zone I quickly decay to the levels of the Zone II densities, which is why m_{t} reaches the values of m_{s} after the pulse. However at this time, the

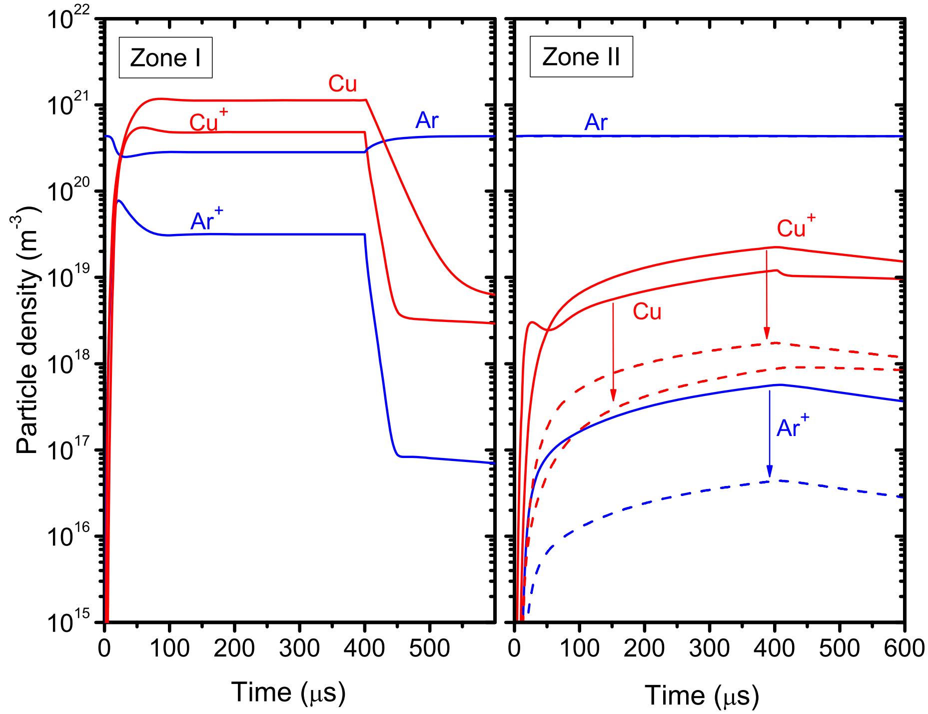

Figure 5.10: As figure 5.9, but for the target voltage of 900 V.

total ion flux to the target is very small and the target voltage is zero, therefore these high values of m_{t} have no influence on sputtering. The ionized fraction of the copper flux onto the substrate, Θ, quickly rises at the beginning of the pulse and remains almost constant during the pulse duration. After the pulse, it drops slowly, corresponding to the diffusion losses of ions and neutral atoms from Zone II. Due to the high plasma densities (high target currents and small size of the magnetron) the ionization of the sputtered copper atoms is very effective. The maximum ionized fraction of the copper flux reaches 70 % for the target voltage of 550 V and even 95 % for the target voltage of 900 V. Naturally, the average ionized fractions which can be compared to the experimental results measured by mass spectrometry are lower.

Figure 5.12 shows the time-averaged values of the discharge and deposition characteristics, $\overline{m}_{\mathrm{t}}$, $\overline{m}_{\mathrm{s}}$, $\overline{\Theta}$, σ_{ga} and σ_{ma} as functions of the target power density in a pulse calculated by the model. An increase in the target power density in the pulse leads to a gradual increase in $\overline{m}_{\mathrm{t}}$, $\overline{m}_{\mathrm{s}}$ and $\overline{\Theta}$, indicating that the plasma contains more of the target material and that it is also more ionized. For high target power densities, the role of argon ions is becoming less important and the depositing flux to the target is dominated by copper ions. For the maximum target power density of $3\,\mathrm{kWcm^{-2}}$ in a pulse, the average ionized fraction $\overline{\Theta}$ reaches 80 %. For the target power density of $539\,\mathrm{Wcm^{-2}}$ in a pulse, Vlček and Burcalová (2010) reported the

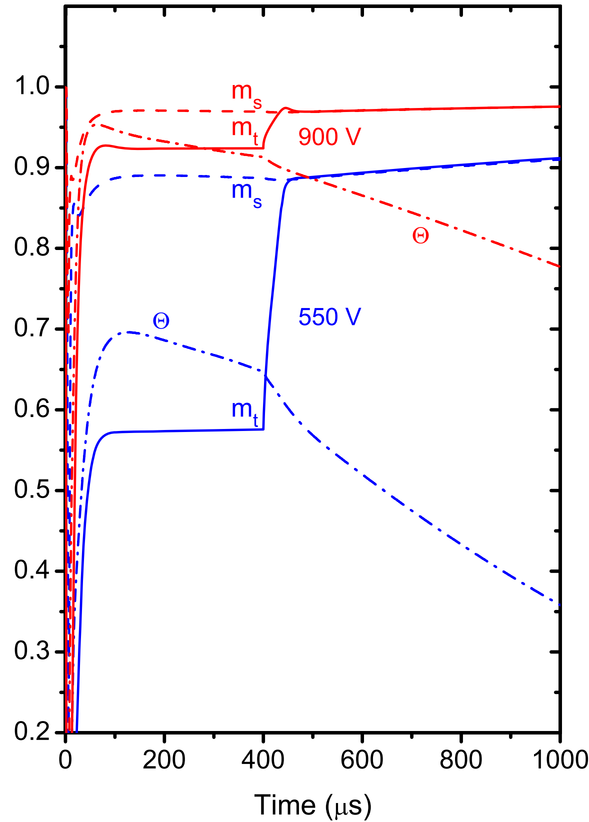

Figure 5.11: Time evolutions of the fractions of target material ions in the total ion fluxes onto the target and substrate, m_{t} and m_{s}, respectively, and of the ionized fraction of target material atoms in the flux onto the substrate, Θ, calculated by the model for the target voltages of 550 V (blue lines) and 900 V (red lines) under the experimental conditions of Anders et al. (2007). The parameter $\omega_{\mathrm{ge}}\tau_{\mathrm{c}} = 16$, the recapture coefficient $r = 0.20$ and the parameter $s = 0.7$.

experimental results of $\overline{m}_{\mathrm{s}} = 92\,\%$ and $\overline{\Theta} = 44\,\%$ obtained by mass spectroscopy which are in a very good agreement with our model results.

The average fractions of ions returning to the target during a pulse, σ_{ga} and σ_{ma}, decrease with the increasing target power density. This is caused primarily by the increasing ionization of the fast atoms which increases the flux of ions into Zone II. This relation between the target power density and the parameters σ is of critical importance because it ensures the ability of the discharge to reach a steady state. The phenomenological model of Vlček and Burcalová (2010) uses a secondary electron balance equation to calculate the ion return probability in a steady-state, see (2.25). Taking into account that the ratio of $\gamma_{\mathrm{ef}}(1-d_{\mathrm{e}})/E_{\mathrm{ef}}$ is only weakly dependent on the target power density, it is clear that an increase in the target voltage (and target power density) must be accompanied by a decrease in σ for the equality to

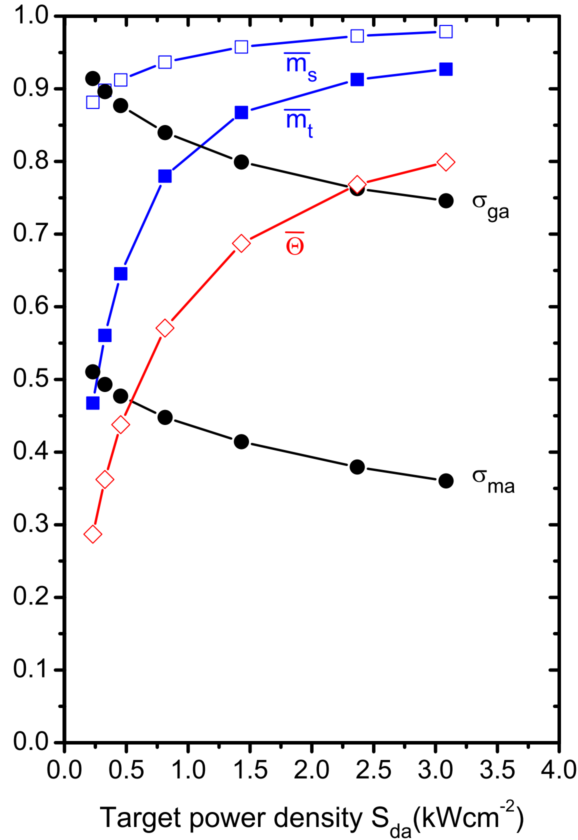

Figure 5.12: Time-averaged values of $\overline{m}_{\mathrm{t}}$, $\overline{m}_{\mathrm{s}}$, $\overline{\Theta}$, σ_{ga} and σ_{ma} as functions of the average target power density in a pulse calculated by the model for the target voltages between 500 V and 960 V under the experimental conditions of Anders et al. (2007). The parameter $\omega_{\mathrm{ge}}\tau_{\mathrm{c}} = 16$, the recapture coefficient $r = 0.20$ and the parameter $s = 0.7$.

hold. In our non-stationary model, this balance condition is naturally included in the particle conservation equations for fast electrons and ions and must be satisfied in the steady-state of the discharge. Therefore, the decrease of σ_{ga} and σ_{ma}, which are calculated from the physical assumptions for the fluxes between the zones, results in the stabilization of the target current for a wide range of applied target voltages, as was shown in figure 5.8. The model results of Vlček and Burcalová (2010) predicted a decrease of σ_{m} (for the ideal case of total self-sputtering of copper) from 0.54 to 0.32 when the target voltage increased from 600 to 1000 V. Andersson and Anders (2009) measured the average fraction σ_{ma} in the case of sustained self-sputtering of copper and obtained a similar decreasing trend (from 0.48 to 0.30 when the target voltage increased from 620 to 920 V), see figure 5.13. Both results are in a good agreement with the values of σ_{ma} calculated by this model.

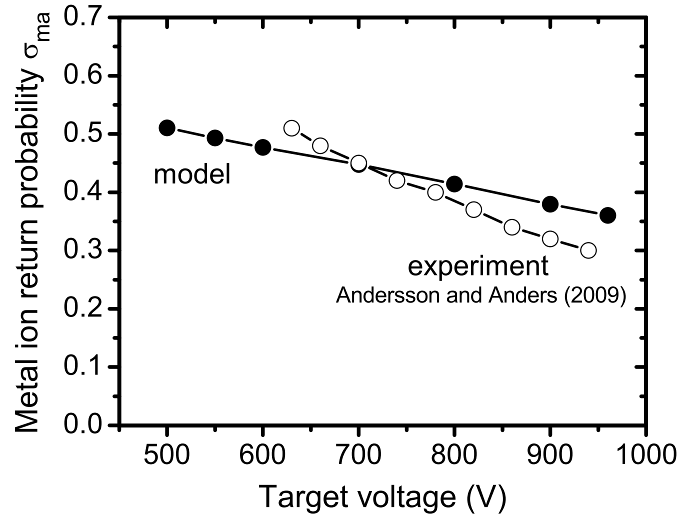

Figure 5.13: Qualitative comparison of the average metal ion return probability, σ_{ma}, calculated by the non-stationary model for the conditions of Anders et al. (2007), see table 5.2, (full symbols) with the values obtained experimentally by Andersson and Anders (2009) (empty symbols).

5.2.4 Conclusions

The calculated target current waveforms were compared to the experimental ones and the effect of several input parameters was shown. A good agreement was obtained for the target voltages higher than 550 V (above the threshold for transition to a high current regime). All target current waveforms followed the same trend – a steady state of the discharge was reached after roughly 100 μs and lasted until the end of the 400 μs pulse. The average target current in a pulse scales according to the relation $I_{\text{da}} \propto U_{\text{d}}^{3.1}$. The stabilization of the discharge and the resulting current–voltage characteristic depends not only on the ionization by secondary electrons, but also markedly on the transport of ions and electrons from the plasma ring, as it follows from the analysis of the effect of the $\omega_{\text{ge}}\tau_{\text{c}}$ parameter and the discussion concerning the role of the σ_{ma} parameter.

For the highest target power density of 3 kWcm^{-2} in a pulse, corresponding to the target voltage of 960 V, plasma densities exceeding 5×10^{20} m^{-3} above the target racetrack and 10^{18} m^{-3} at the substrate in the distance of 200 mm are predicted by the model. Then the discharge is almost entirely dominated by the target material – in average, copper ions constitute 93 % of the ion flux onto the target and 98 % of the ion flux onto the substrate. The calculated average ionized fraction of copper atoms in the flux onto the substrate is 80 %.

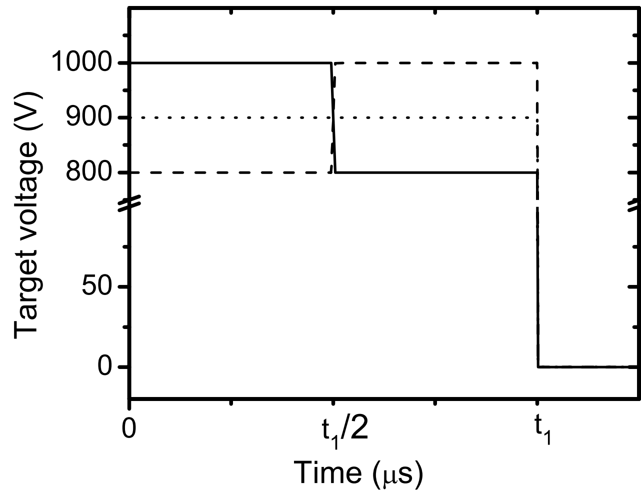

Figure 5.14: Target voltage waveforms of the constant-target-voltage pulse (dotted line) and the stepwise ascending (dashed lines) and the stepwise descending (solid line) pulses. The pulse length, t_1, was between 20 μs and 400 μs.

5.3 Effect of the voltage pulse characteristics

This study stems from the simulations done for the previous section. However, we used a more common argon pressure of 1 Pa. Again, copper was used as the target material. The target and substrate diameters were 50 mm with the target-to-substrate distance of 75 mm. The effect of the magnetic field was studied for three values of the effective magnetic field strength, 350 G, 400 G and 450 G. The voltage pulse length, t_1, varied in the range between 20 μs and 400 μs. The effect of the voltage pulse shape was studied for three different types of pulses. The constant-target-voltage pulse is a rectangular pulse with a constant amplitude of 900 V. The stepwise-target-voltage pulses are characterized by a step transition of the target voltage from 800 to 1000 V (ascending) or from 1000 to 800 V (descending) occurring in the middle of the pulse, so that the average target voltage during the pulse is again 900 V, see figure 5.14. The influence of the repetition frequency of pulses was studied for 100 Hz, 500 Hz and 2000 Hz. The secondary electron recapture coefficient was set to $r = 0.3$, taking into account the pressure of 1 Pa (lower than in the previous study). The s parameter, determining the secondary electron emission coefficient γ_{m} was set to $s = 0.65$. All the process input parameters are summarized in table 5.4.

5.3.1 Constant-target-voltage pulses

First, the effect of the magnetic field strength and the effect of the voltage pulse length for the constant-target-voltage pulses will be discussed. Figure 5.15 shows the calculated target current waveforms for the various pulse lengths ranging from 20 μs

to 400 μs and two values of the magnetic field strength. As expected, the higher magnetic field strength of 450 G results in a higher target current obtained for the same target voltage of 900 V, which is caused by an increased plasma confinement above the target racetrack. In the model, this is realized by the coefficient of electron diffusion from Zone I, see (4.52). The shape of the target current waveforms during the pulse-on time is not affected by the pulse length. This is no surprise taking into account that the applied voltage is constant and also the starting conditions (plasma density, composition and temperature) are the same for all cases due to the fact that the pulse lengths are very small compared to the pulse period $T = 10\,\mathrm{ms}$ corresponding to the repetition frequency of 100 Hz. After 100 μs, the discharge reaches a steady state with the target current of 36 A and 26 A for the higher and lower magnetic field strength, respectively. For the shorter pulse lengths of 20 μs and 50 μs, the discharge is terminated before reaching the steady state which results in "triangular" current waveforms.

Figure 5.16 shows the effect of the magnetic field strength on the fluxes of particles in the discharge for the pulse length of 400 μs. During the pulse, the copper ion return probability, σ_{m}, is practically constant and it is lower for the lower magnetic field strength of 350 G. After the pulse, the densities of ions and atoms in Zone I quickly decrease down to the densities in the larger Zone II, see the time evolutions of particle densities in figures 5.9 and 5.10. Then the ions diffuse from Zone II onto chamber walls and also into Zone I and further onto the target. The flux of the copper ions onto the target is practically the same as their flux into Zone I. Therefore, the σ_{m} parameter jumps quickly towards 1 after the pulse.

The fraction of the copper ions in the total ion flux onto the target, m_{t}, is above 90% for both cases indicating that we are in a strongly self-sputtering regime. Due to the higher target current reached for the higher magnetic field strength, which leads to a more intensive ionization of atoms in Zone I, the ionized fraction of sputtered copper atoms in the flux onto the substrate, Θ, increases faster during the pulse and it is higher during the entire period, compared to the lower magnetic field case.

Model volume (radius $\times$ length)	200×75 mm
Target diameter	50 mm
Substrate diameter	50 mm
Target material	Cu
Argon pressure	1.0 Pa
Magnetic field	350, 400, 450 G
Target voltage	900 V
Pulse length	$20 - 400$ μs
Repetition frequency	100, 500, 2000 Hz

Table 5.4: Model process input parameters used in the study of the effect of the voltage pulse characteristics.

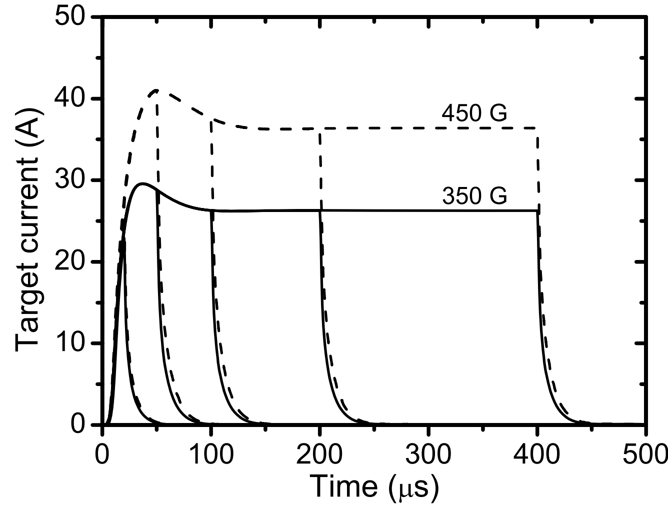

Figure 5.15: Target current waveforms calculated by the model for various pulse lengths, the magnetic field strength of 350 G and 450 G, the target voltage of 900 V and the repetition frequency of 100 Hz.

Note that the copper atoms and ions arrive at the substrate also after the pulse, even though practically no new copper atoms and hence ions are introduced into the chamber. The decay of atom and ion densities in Zone II is given by diffusion towards chamber walls.

The upper panel of figure 5.17 shows that the average target power density in a pulse, S_{da}, increases with the increasing pulse length and that it is systematically higher for the higher magnetic field strength. The S_{da} dependence on the pulse length sharply rises between $20\,\mu$s and $100\,\mu$s, i.e. during the discharge build-up phase. For longer pulses, the target current has reached the steady state. Therefore, the average target power density S_{da} tends to saturate at the maximum value of approximately $UI_{\mathrm{ss}}/S_{\mathrm{t}}$, where I_{ss} is the steady-state target current (figure 5.15).

In the lower panel of figure 5.17, the average ionized fraction of sputtered copper atoms in the flux onto the substrate, $\overline{\Theta}$, increases nearly proportionally to the average target power density in a pulse (see also figure 5.23 below). The results suggest that sufficiently long pulses which allow for a build-up of high density plasma are needed to obtain a high ionized fraction $\overline{\Theta}$. On the other hand, a very long $400\,\mu$s pulse does not give a significant improvement over a medium $100\,\mu$s pulse. The normalized deposition rate, $\overline{a}_{\mathrm{D}}/\overline{S}_{\mathrm{d}}$, is decreasing with the increasing pulse length and with the increasing magnetic field strength. The calculated trends for $\overline{\Theta}$ and $\overline{a}_{\mathrm{D}}/\overline{S}_{\mathrm{d}}$ are in qualitative agreement with the measurements of Konstantinidis et al. (2006).

The effects of the pulse length and the magnetic field strength on the $\overline{a}_{\mathrm{D}}/\overline{S}_{\mathrm{d}}$ and $\overline{\Theta}$ values, shown in figure 5.17, are connected with the degree of ionization of copper atoms in the discharge, which is clearly indicated by the $\overline{\Theta}$ dependences obtained. In our case, the target voltage is constant, thus the decrease in $\overline{a}_{\mathrm{D}}/\overline{S}_{\mathrm{d}}$

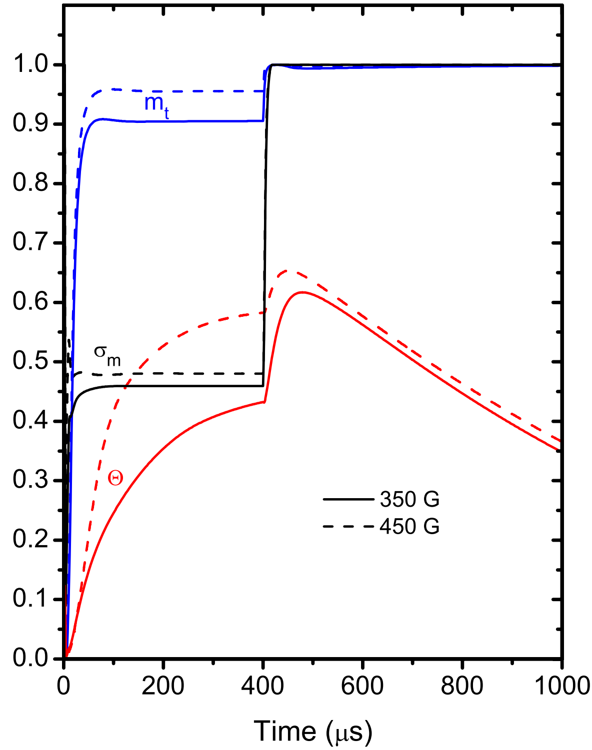

Figure 5.16: Discharge flux characteristics calculated by the model for the pulse length of 400 μs, the magnetic field strength of 350 G and 450 G, the target voltage of 900 V and the frequency of 100 Hz. Here, m_{t} is the fraction of copper ions in the total ion flux onto the target, Θ is the ionized fraction of sputtered copper atoms in the flux onto the substrate and σ_{m} is the fraction of copper ion flux onto the target in the total copper ion flux leaving Zone I.

in figure 5.17 can be caused mainly by the return of copper ions onto the target or by their higher losses, compared to the sputtered neutrals, towards chamber walls. According to our calculations, the copper ion return probability during the pulse is between 41 % and 48 % under these conditions (see 45 – 48 % in figure 5.16). As the degree of ionization of copper atoms in the discharge increases with increasing S_{da}, these returning ions represent a significant fraction of the originally sputtered copper atoms, which are not available for deposition on the substrate.

5.3.2 Stepwise-target-voltage pulses

In this section, the presented results for the constant-target-voltage pulses will be compared to the results for the stepwise-target-voltage pulses. The magnetic field strength was 400 G for these calculations. The calculated target current waveforms are shown in figure 5.18 for the pulse lengths of 400 μs and 50 μs. For the pulse length of 400 μs, there is enough time for the discharge to develop into a steady

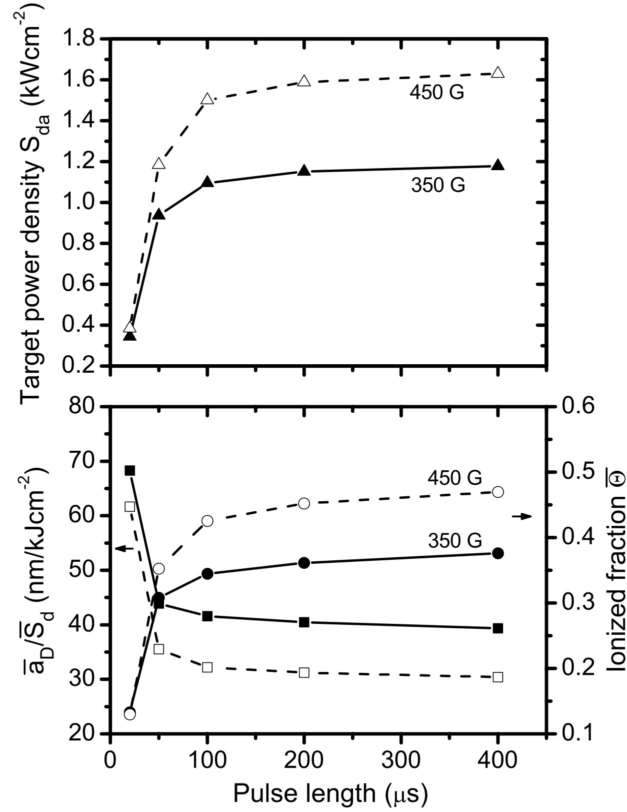

Figure 5.17: The average target power density in a pulse, S_{da}, the average ionized fraction of sputtered copper atoms in the flux onto the substrate, $\overline{\Theta}$, and the normalized deposition rate, $\overline{a}_{\mathrm{D}}/\overline{S}_{\mathrm{d}}$, calculated for various pulse lengths, the magnetic field strength of 350 G and 450 G, the target voltage of 900 V and the repetition frequency of 100 Hz.

state during each half of the stepwise-target-voltage pulses. It can be seen that the dependence of the steady-state target current on the target voltage is non-linear with a larger target current difference between 1000 V and 900 V than between 900 V and 800 V. For the pulse length of 50 μs, no steady states are reached. The highest peak target current is achieved for the ascending voltage pulse.

Figure 5.19 shows that for long pulses, the average target power density S_{da} delivered to the discharge is almost the same for the stepwise ascending and descending voltage pulses. This is because the target current reaches a steady state in each half of the voltage pulse and these two parts of the pulse are practically the same for both the ascending and descending voltage (see the target current waveforms in figure 5.18). The target power density S_{da} for the stepwise target voltage is always higher than for the constant target voltage, even though the average target voltage is the same. This is due to the non-linear and convex dependence of the average target current on the target voltage in the range between 800 V and 1000 V. For pulses shorter than 100 μs, the stepwise ascending target voltage is able to provide the highest target power density which is due to the fact that the highest target

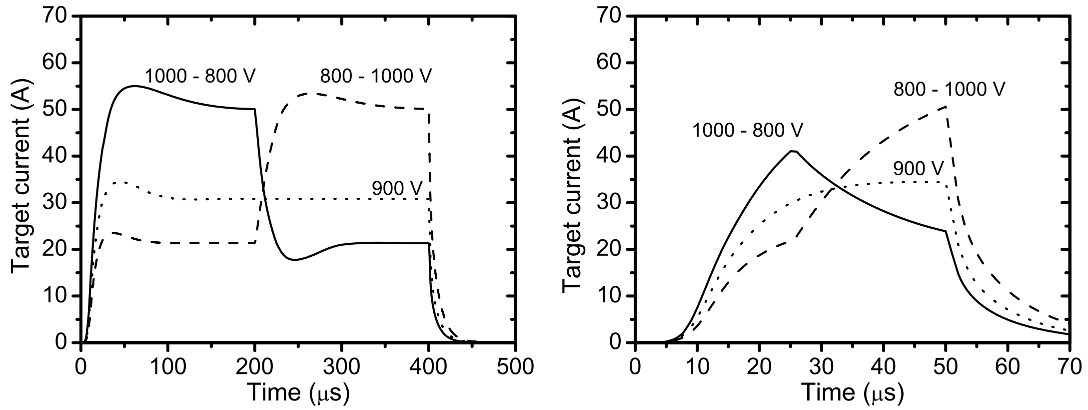

Figure 5.18: Target current waveforms calculated by the model for the target voltage of 900 V or the stepwise ascending ($800 - 1000$ V) and descending ($1000 - 800$ V) target voltages at the pulse length of 400 μs (left panel) and 50 μs (right panel), the repetition frequency of 100 Hz and the magnetic field strength of 400 G.

voltage of 1000 V is applied later in the pulse which allows the discharge to develop a higher peak target current (figure 5.18).

For the short target voltage pulses of 20 μs and 50 μs, the average ionized fraction of copper atoms in the flux onto the substrate is highest for the ascending voltage pulses. This is due to the aforementioned highest target current reached in this case leading to highest electron density and highest ionization of the sputtered atoms in front of the target. Figure 5.20 shows that Θ is higher for the ascending voltage after the pulse, which indicates that more copper ions are present in the discharge after the pulse. Because the pulses are so short, the ionized fraction Θ is relatively low during the pulse for both cases. The flux of ions after the pulse then becomes a dominant contribution to the total ion flux onto the substrate.

Surprisingly, for the long pulses of 200 μs and 400 μs, the average ionized fraction $\overline{\Theta}$ is lower for the ascending voltage pulses than for the descending pulses, although the average target power density S_{da} is practically the same. Figure 5.20 shows the time evolutions of the ionized fraction Θ for both the stepwise voltage pulses at the pulse length of 400 μs. Although the ionized fraction Θ is again higher after the pulse for the ascending target voltage, there is a significant difference in Θ during the pulse. In the first half of the pulse, Θ reaches up to 75 % for the descending voltage pulse (when the target voltage is 1000 V) and only up to 23 % for the ascending voltage pulse (when the target voltage is 800 V). In the second half of the pulse, Θ reaches up to 73 % for the ascending voltage pulse and it remains above 45 % for the descending voltage pulse. Overall, Θ is higher for the descending voltage during the pulse and since the pulses are long, this makes a dominant contribution to the total ion flux onto the substrate during the pulse period. This explains why we obtained higher average ionized fractions $\overline{\Theta}$ for the long descending voltage pulses (figure 5.19). As expected, the normalized deposition rate, $\overline{a}_{\mathrm{D}}/\overline{S}_{\mathrm{d}}$, again decreases with the increasing average ionized fraction $\overline{\Theta}$.

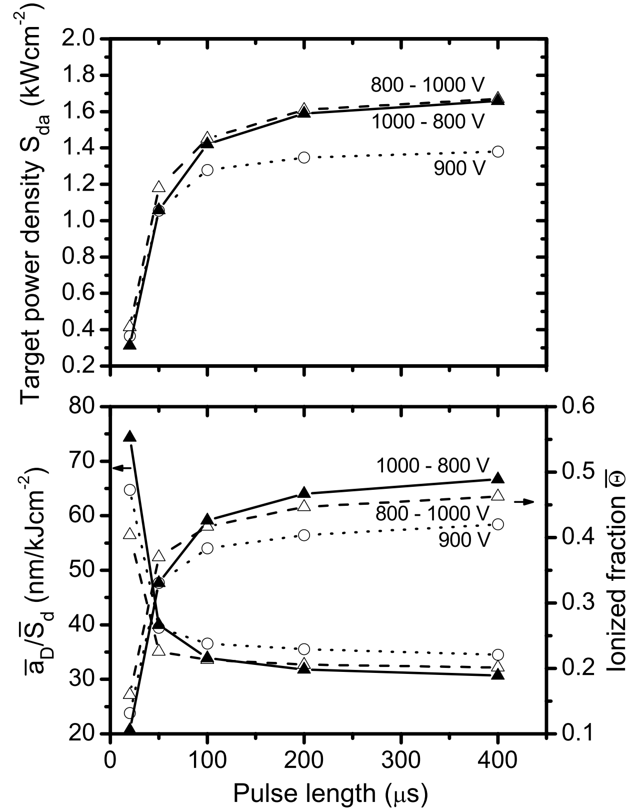

Figure 5.19: The average target power density in a pulse, S_{da}, the average ionized fraction of sputtered copper atoms in the flux onto the substrate, $\overline{\Theta}$, and the normalized deposition rate, $\overline{a}_{\mathrm{D}}/\overline{S}_{\mathrm{d}}$, calculated for various pulse lengths and the target voltage of 900 V or the stepwise ascending (800 − 1000 V) and descending (1000 − 800 V) target voltages. The repetition frequency was 100 Hz and the magnetic field strength was 400 G.

5.3.3 Influence of the repetition frequency

In this section, the effect of the repetition frequency of pulses will be discussed. We simulated the discharges with the magnetic field strength of 400 G, three repetition frequencies of 100 Hz, 500 Hz and 2000 Hz and various pulse lengths at the maximum duty cycle of 10% for each repetition frequency. Figure 5.21 shows the difference in the target current waveforms for the extreme values of 100 Hz and 2000 Hz. Only the two shortest pulse lengths (20 μs and 50 μs) are presented to distinguish the details at the beginning of the pulses. As expected, a higher repetition frequency leads to an earlier target current rise caused by the higher plasma density at the beginning of the pulse due to the previous pulse. Even for 100 Hz, the target current rises relatively quickly (10 μs after the pulse initiation). This is caused mainly by the high target voltage of 900 V and the small size of the magnetron used. Thus, the effect of the increased repetition frequency is quite small in our case.

Figure 5.22 shows an increase in the average target power density S_{da} associated

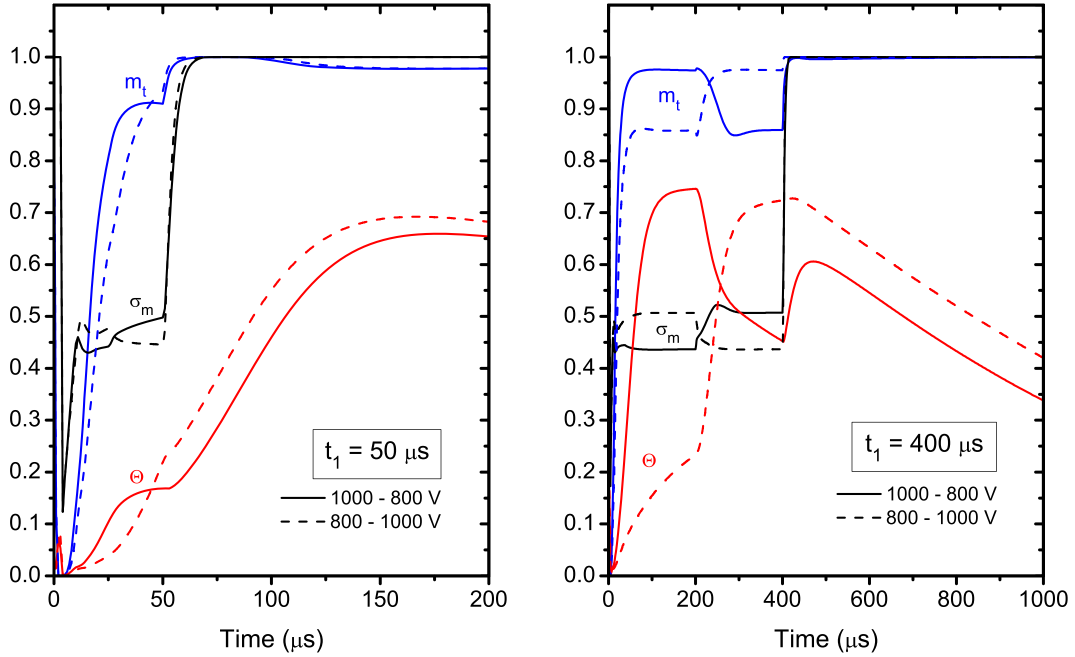

Figure 5.20: Discharge flux characteristics calculated by the model for the pulse length of 50 μs (left panel) and 400 μs (right panel), the stepwise ascending (800 − 1000 V) and descending (1000 − 800 V) target voltages, the repetition frequency of 100 Hz and the magnetic field strength of 400 G. Here, m_{t} is the fraction of copper ions in the total ion flux onto the target, Θ is the ionized fraction of sputtered copper atoms in the flux onto the substrate and σ_{m} is the fraction of copper ion flux onto the target in the total copper ion flux leaving Zone I.

with a faster rise in the target currents when the repetition frequency increases. However, this effect is significant only for the shortest pulses. As a results, the average ionized fraction $\overline{\Theta}$ is also increased only for the shortest pulse length of 20 μs, while it is almost unchanged for longer pulses.

5.3.4 Influence of the target power density in a pulse

Figure 5.23 shows a correlation between the values of $\overline{a}_{\mathrm{D}}/\overline{S}_{\mathrm{d}}$ and $\overline{\Theta}$ obtained in all our model calculations (presented in figures 5.17, 5.19 and 5.22), together with the values of m_{ta}, and the corresponding average target power density in a pulse, S_{da}. Polynomial functions are fitted to the data to emphasize the trends (dotted lines). In agreement with the previous results, the ionized fraction $\overline{\Theta}$ increases with an increasing target power density S_{da}, but the normalized deposition rate $\overline{a}_{\mathrm{D}}/\overline{S}_{\mathrm{d}}$ significantly decreases. As expected, the average fraction of copper ions in the total ion flux onto the target in a pulse, m_{ta}, increases with S_{da} (figure 5.23).

As can be seen in figure 5.23, the average target power density S_{da} is a fun-

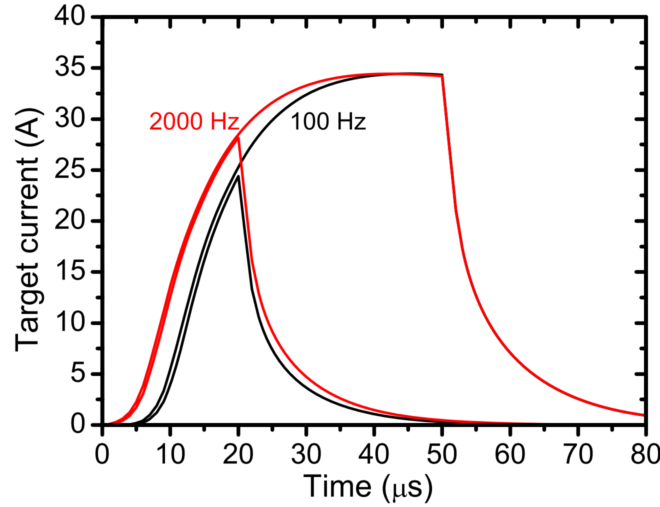

Figure 5.21: Target current waveforms calculated by the model for the voltage pulse lengths of 20 μs and 50 μs, the repetition frequency of 100 Hz and 2000 Hz, the target voltage of 900 V and the magnetic field strength of 400 G.

damental quantity determining the important deposition characteristics $\overline{a}_{\mathrm{D}}/\overline{S}_{\mathrm{d}}$ and $\overline{\Theta}$ under the conditions investigated (a constant target voltage or average target voltage during pulses). The magnetic field strength and the voltage pulse characteristics, such as the pulse length, shape and repetition frequency, result in only minor deviations from the general trends. However, it should be pointed out that a lower magnetic field strength has a positive effect of providing a higher ionized fraction $\overline{\Theta}$ and higher normalized deposition rate $\overline{a}_{\mathrm{D}}/\overline{S}_{\mathrm{d}}$ for a fixed average target power density S_{da}. This can be seen for $S_{\mathrm{da}} \simeq 1.2\,\mathrm{kWcm}^{-2}$, for which the symbols related to the magnetic field strength of 350 G (□) are systematically above those for 450 G (◊). This is in agreement with the measurements of Mishra et al. (2010).

The fundamental decrease of the normalized deposition rate is in agreement with the predictions of the phenomenological model of Vlček and Burcalová (2010), see section 2.2.2. To understand their relations obtained for $a_{\mathrm{D}}/S_{\mathrm{d}}$ and Θ, see (2.22) and (2.29), respectively, we use simplified formulas based on the assumptions that $\xi_{\mathrm{i}}/\xi_{\mathrm{n}} = 1$ and $\gamma = 0$

$$\frac{a_{\mathrm{D}}}{S_{\mathrm{d}}} = k\frac{S_{\mathrm{m}}}{S_{\mathrm{mg}}}(1-\beta\sigma)\frac{U_{\mathrm{d}}^{-0.5}}{1+\gamma_{\mathrm{ef}}} \tag{5.1}$$

and

$$\Theta = \frac{\beta(1-\sigma)}{1-\beta\sigma}\,. \tag{5.2}$$

Here, β is the probability of ionization of sputtered atoms in front of the target, σ is the probability of return of ionized sputtered atoms to the target, S_{m} and γ_{ef} are the effective sputtering yield and secondary-electron emission coefficient of the target material, respectively, considering simultaneous effects of the process gas ions and the target material ions, and S_{mg} is the sputtering yield related to the process

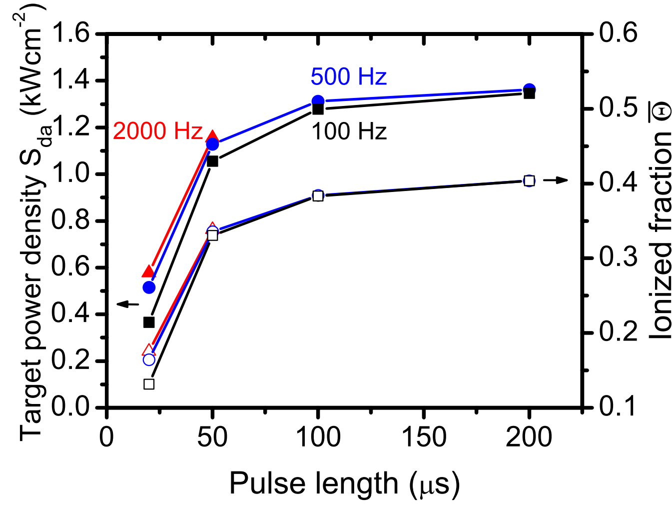

Figure 5.22: The average target power density in a pulse, S_{da}, and the average ionized fraction of sputtered copper atoms in the flux onto the substrate, $\overline{\Theta}$, calculated for various pulse lengths and the repetition frequency of 100 Hz (solid lines), 500 Hz (dotted lines) and 2000 Hz (dashed lines).

gas ions only. Using the relation $m_{\mathrm{t}} = \beta\sigma S_{\mathrm{m}}$, we obtain from (5.1) and (5.2)

$$\frac{a_{\mathrm{D}}}{S_{\mathrm{d}}} = k\frac{S_{\mathrm{m}} - m_{\mathrm{t}}}{S_{\mathrm{mg}}}\frac{U_{\mathrm{d}}^{-0.5}}{1 + \gamma_{\mathrm{ef}}} \tag{5.3}$$

and

$$\Theta = \frac{m_{\mathrm{t}}(1/\sigma - 1)}{S_{\mathrm{m}} - m_{\mathrm{t}}}\,. \tag{5.4}$$

Taking into account that the target voltage or the average target voltage in a pulse has the same value of 900 V in all the present calculations and that $\sigma \propto 1/U_{\mathrm{d}}$ and $\gamma_{\mathrm{ef}} \ll 1$, it is clearly seen from equations (5.3) and (5.4) that an increase in the average target power density S_{da}, leading to higher values of m_{ta} (figure 5.23), results in a decrease in $\overline{a}_{\mathrm{D}}/\overline{S}_{\mathrm{d}}$ and an increase in $\overline{\Theta}$, respectively. This qualitative agreement of the phenomenological model and the non-stationary model results obtained under various process conditions shows that these trends have a general validity beyond the steady-state assumption of the phenomenological model.

5.3.5 Conclusions

It was shown that sufficiently long pulses (at least 100 μs), which allow for the build-up of a high density plasma in front of the target, are necessary to achieve high target power densities in a pulse and, consequently, high degrees of ionization of the sputtered copper atoms. An increased magnetic field strength in front of the target also promotes a higher target power density at a fixed target voltage. Higher

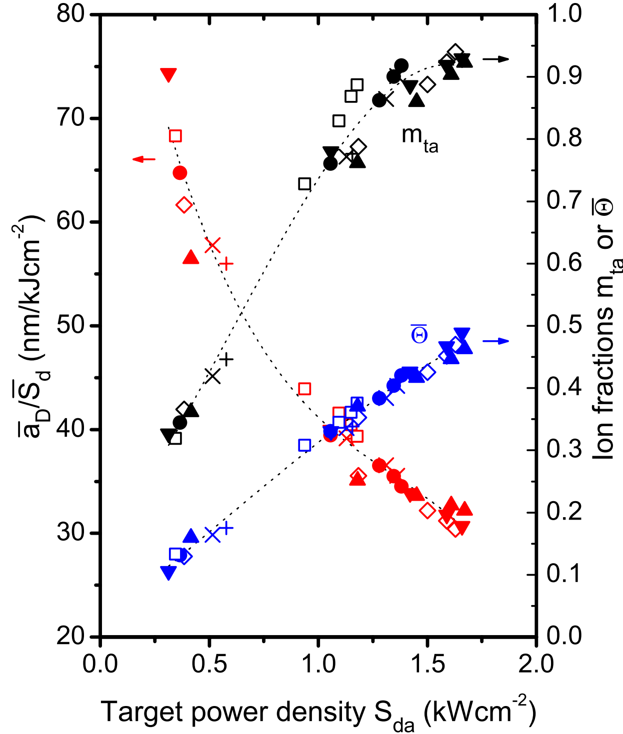

Figure 5.23: The normalized deposition rate, $\overline{a}_{\mathrm{D}}/\overline{S}_{\mathrm{d}}$, the average fraction of copper ions in the total ion flux onto the target, m_{ta}, and the average ionized fraction of sputtered copper atoms in the flux onto the substrate, $\overline{\Theta}$, in correlation to the average target power density in a pulse, S_{da}, for all the previously presented calculations including varying pulse lengths. The symbols are related to the constant-target-voltage pulses with the repetition frequency of 100 Hz and the magnetic field strength of 350 G (□), 400 G (•) and 450 G (◊), to the constant-target-voltage pulses with the magnetic field strength of 400 G and the repetition frequency of 500 Hz (×) and 2000 Hz (+), and to the stepwise-target-voltage pulses with the ascending (▲) and descending (▼) target voltages.

repetition frequencies of pulses lead also to higher target power densities, but this effect is relevant only for short pulses (less than 50 μs).

From the analysis of all model results, obtained for various process parameters, it follows that the average target power density in a pulse is, besides the target voltage, a fundamental quantity determining the average ionized fraction of copper atoms in the flux onto the substrate and the normalized deposition rate. The normalized deposition rate decreased 2.3 times when the target power density increased from 300 Wcm^{-2} to 1700 Wcm^{-2} in a pulse. It was shown that the return of ionized sputtered atoms to the target, combined with their probable higher losses compared to neutral sputtered atoms to chamber walls during transfer to the substrate, is a dominant effect responsible for this normalized deposition rate reduction under the

conditions investigated. A compromise between a high degree of ionization of the sputtered target material atoms and an acceptable deposition rate should be found by tuning the average target power density delivered in a pulse. Further optimization of the deposition process can be achieved by modification of the magnetic field used.

5.4 Transport and ionization of the sputtered target material

In the previous section, it was shown that the steady-state phenomenological model (Vlček and Burcalová, 2010), see section 2.2.2, can qualitatively explain the trends in the deposition characteristics obtained by the non-stationary two-zone model. In this section, we continue with a more detailed quantitative comparison of both models which contributes to the understanding of the mechanisms that govern the transport and ionization of the sputtered target material atoms in HiPIMS discharges.

For the comparison, we use a typical HiPIMS discharge with the input parameters similar to those used in the previous study. The radius and length of the simulation volume was 200 mm and 100 mm, respectively, at the argon pressure of 1 Pa. The sputtered target (copper) and substrate diameters were 50 mm at the target-to-substrate distance of 100 mm. The rectangular voltage pulses were 200 μs long with the amplitudes from 400 V to 1000 V (see table 5.6) at the repetition frequency of 100 Hz. The effective magnetic field strength, B, in Zone I was varied from 150 G to 700 G. The electron gyration-to-collision frequency ratio was set to $\omega_{\mathrm{ge}}\tau_{\mathrm{c}} = 16$ in the non-stationary two-zone model, and the recapture probability of secondary electrons to $r = 0.3$ and the s parameter to $s = 0.65$ in both the models used. The parameters characterizing the HiPIMS systems investigated are summarized in table 5.5.

Model volume (radius $\times$ length)	20×10 mm
Target diameter	50 mm
Substrate diameter	50 mm
Target material	Cu
Argon pressure	1.0 Pa
Magnetic field	$150 - 700$ G
Target voltage	$400 - 1000$ V
Pulse length	200 μs
Repetition frequency	100 Hz

Table 5.5: Model process input parameters used for the comparison of the non-stationary two-zone model with the steady-state phenomenological model of Vlček and Burcalová (2010).

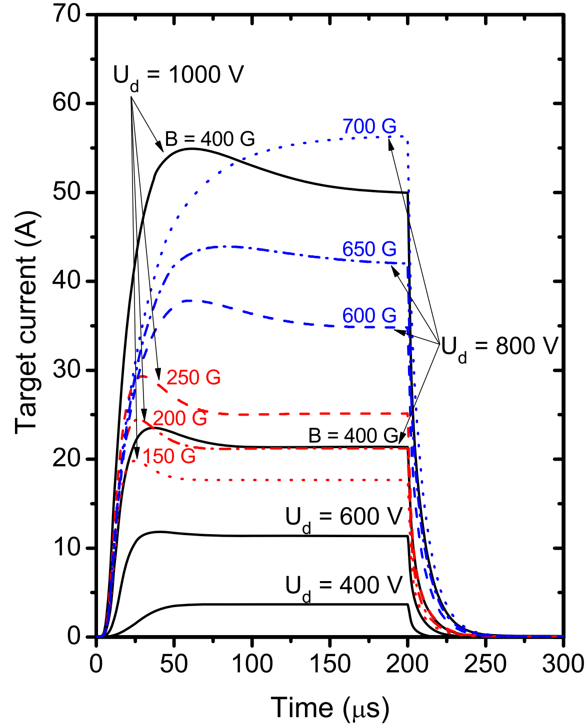

Figure 5.24: Target current waveforms calculated by the non-stationary two-zone model for the target voltages, U_{d}, between 400 V and 1000 V at the magnetic field strength $B = 400\,\mathrm{G}$, for $U_{\mathrm{d}} = 800\,\mathrm{V}$ at the magnetic field strengths between 400 G and 700 G, and for $U_{\mathrm{d}} = 1000\,\mathrm{V}$ at the magnetic field strengths between 150 G and 400 G.

Figure 5.24 shows the target current waveforms calculated by the non-stationary two-zone model. As expected, an increase in the U_{d} values at a fixed B and in the B values at a fixed U_{d} leads to higher target currents during pulses.

Discharge parameters, which are of key importance for a better understanding of the complicated processes in the HiPIMS discharges investigated, are given in table 5.6. The average fraction of target material ions in the total ion flux onto the target in a pulse, m_{ta}, calculated by the non-stationary two-zone model (equation (4.76)), was used for the value of the fundamental input parameter m_{t} of the steady-state phenomenological model, which effectively provides the dependence of m_{t} on S_{da}. Then, the probability of return of ionized sputtered atoms to the target, σ, was calculated using (2.25), where we put $d_{\mathrm{e}} = 0$, with the help of (2.26) and (2.27). In equation (2.27), the more accurate energies $E_{\mathrm{g}} = 26.9\,\mathrm{eV}$ and $E_{\mathrm{m}} = 17.8\,\mathrm{eV}$ than in Vlček and Burcalová (2010) were used. They were determined by us with the use of a Monte Carlo simulation of individual secondary electrons, taking into account their elastic, excitation and ionization collisions with neutral atoms. The probability of ionization of sputtered atoms in front of the target, β, was calculated using (2.28)

U_d(V)	B(G)	S_{da}(Wcm^{-2})	m_{ta}	σ_{ma}	σ	β
400	400	64	0.21	0.70	0.86	0.12
450	400	115	0.30	0.66	0.76	0.18
500	400	173	0.40	0.63	0.69	0.25
550	400	240	0.49	0.60	0.63	0.32
600	400	321	0.57	0.58	0.58	0.39
650	400	411	0.65	0.56	0.53	0.46
700	400	528	0.72	0.54	0.49	0.53
750	400	663	0.77	0.52	0.46	0.58
800	400	826	0.82	0.50	0.43	0.64
850	400	1050	0.87	0.49	0.41	0.69
900	400	1350	0.90	0.47	0.39	0.73
950	400	1730	0.93	0.45	0.37	0.76
1000	400	2430	0.95	0.44	0.35	0.79
800	600	1330	0.92	0.55	0.44	0.72
800	650	1560	0.94	0.56	0.44	0.73
800	700	1930	0.95	0.57	0.44	0.75
1000	150	859	0.70	0.33	0.35	0.57
1000	200	1040	0.79	0.37	0.35	0.65
1000	250	1230	0.85	0.39	0.35	0.71

Table 5.6: Discharge parameters as functions of the magnetron voltage, U_d, for various magnetic field strengths, B. Here, S_{da} is the average target power density in a pulse, m_{ta} is the average fraction of target material ions in the total ion flux onto the target in a pulse and σ_{ma} is the average return probability of the target material ions in a pulse, all calculated by the non-stationary two-zone model; σ and β is the ion return probability and the ionization probability of sputtered atoms, respectively, calculated by the steady-state phenomenological model with $m_{ta} = m_t$.

with the help of (2.24).

As shown in table 5.6, the values of m_{ta} and β increase with the increasing target power density S_{da}. Simultaneously, the values of σ, being in good agreement with σ_{ma}, decrease mainly due to the increase in the magnetron voltage U_d (equation (2.25)).

For the given magnetron voltage U_d and the already known values of $m_t = m_{ta}$, β, σ, S_m, S_{mg} and γ_{ef} and for a set of chosen values of ξ_i/ξ_n and γ, the deposition rate per average target power density $\overline{a}_D/\overline{S}_d$ was calculated using (2.22) and (2.23), and the average ionized fraction $\overline{\Theta}$ using (2.29). The constant k in (2.22) was determined by equating the value of $\overline{a}_D/\overline{S}_d$ obtained for $U_d = 400$ V with the use of the steady-state phenomenological model to that obtained for the same U_d with the use of the non-stationary two-zone model.

Figure 5.25 shows typical dependences of the deposition rate per target power

density $\overline{a}_\mathrm{D}/\overline{S}_\mathrm{d}$ and the ionized fraction $\overline{\Theta}$ on the target power density in a pulse of HiPIMS discharges. With $\xi_\mathrm{i}/\xi_\mathrm{n} = 0.5$ in the steady-state phenomenological model, we achieved an excellent agreement between both models. An additional ionization in the plasma bulk ($\gamma = 0.1$) had a small effect on the $\overline{a}_\mathrm{D}/\overline{S}_\mathrm{d}$ ratio and a significant effect on the $\overline{\Theta}$ values calculated using the phenomenological model.

The phenomenological model makes it possible to evaluate easily a role played by various individual processes in a transport and ionization of sputtered atoms in HiPIMS discharges. As can be seen in figure 5.25, a rise in S_da from $64\,\mathrm{Wcm}^{-3}$ to $2430\,\mathrm{Wcm}^{-3}$ resulted in the 2.01 times and 3.10 times lower $\overline{a}_\mathrm{D}/\overline{S}_\mathrm{d}$ values for $\xi_\mathrm{i}/\xi_\mathrm{n} = 1.0$ and 0.5, respectively. These decreases are mainly due to a less-than-linear increase of the sputtering yields with ion energy(Anders, 2010) (the $U_\mathrm{d}^{-0.5}$ factor in equation (2.22) reduced 1.58 times) and a backward flux of ionized sputtered atoms to the target for $\xi_\mathrm{i}/\xi_\mathrm{n} = 1.0$ (the terms in the square bracket in (2.23) reduced 1.24 times) or the backward flux of ionized sputtered atoms combined with higher losses of ions, compared with neutrals, to chamber walls for $\xi_\mathrm{i}/\xi_\mathrm{n} = 0.5$ (the terms in the square bracket in (2.23) reduced 1.91 times). A change of ions causing sputtering and secondary electron emission from the target resulted in only small changes of the $\overline{a}_\mathrm{D}/\overline{S}_\mathrm{d}$ values (the $S_\mathrm{m}/S_\mathrm{mg}$ ratio in (2.23) reduced 1.05 times and the $(1+\gamma_\mathrm{ef})^{-1}$ factor in (2.22) increased 1.02 times, respectively).

The non-stationary two-zone model predicts higher values of $\overline{a}_\mathrm{D}/\overline{S}_\mathrm{d}$ and $\overline{\Theta}$ (figure 5.25) for lower magnetic field strengths (and higher respective magnetron voltages) at the same S_da, being in the range from $859\,\mathrm{Wcm}^{-2}$ to $1930\,\mathrm{Wcm}^{-2}$ (table 5.6). Recently, an enhancement of deposition rates in HiPIMS discharges due to a lowering of the magnetic field strengths at a fixed target power density was proved experimentally (Ehiasarian and Vetushka, 2009; Mishra et al., 2010; Capek et al., 2012). In addition, Capek et al. (2012) have reported that the values of $\overline{\Theta}$ remain unchanged under such conditions. The observed effects of the magnetic field can be explained using the phenomenological model. From (2.25), it follows that an increase in U_d, needed to keep the same S_da, and hence $\overline{S}_\mathrm{d}$, at a decreasing magnetic field strength, leads to a decrease of the probability of return of ionized sputtered atoms to the target, σ, when the other parameters remain almost constant. As a result, the $\overline{a}_\mathrm{D}/\overline{S}_\mathrm{d}$ ratio, given by (2.22) and (2.23), and the ionized fraction $\overline{\Theta}$, given by (2.29), can increase. However, the magnetic field strength needs to be sufficiently high to avoid higher losses of electrons to chamber walls (see also the d_e fraction in (2.25)), and thus to keep the same β and $\xi_\mathrm{i}/\xi_\mathrm{n}$ values, appearing in (2.23) and (2.29), at a fixed S_da (table 5.6).

5.4.1 Conclusions

In conclusion, it was shown that the steady-state phenomenological model provides a reliable description of fundamental deposition parameters characterizing efficiency of magnetron sputtering and the transfer of target material ions to the substrate in typical HiPIMS discharges with relatively long steady-state regimes established during pulses. The model relations for the deposition rate per target power density

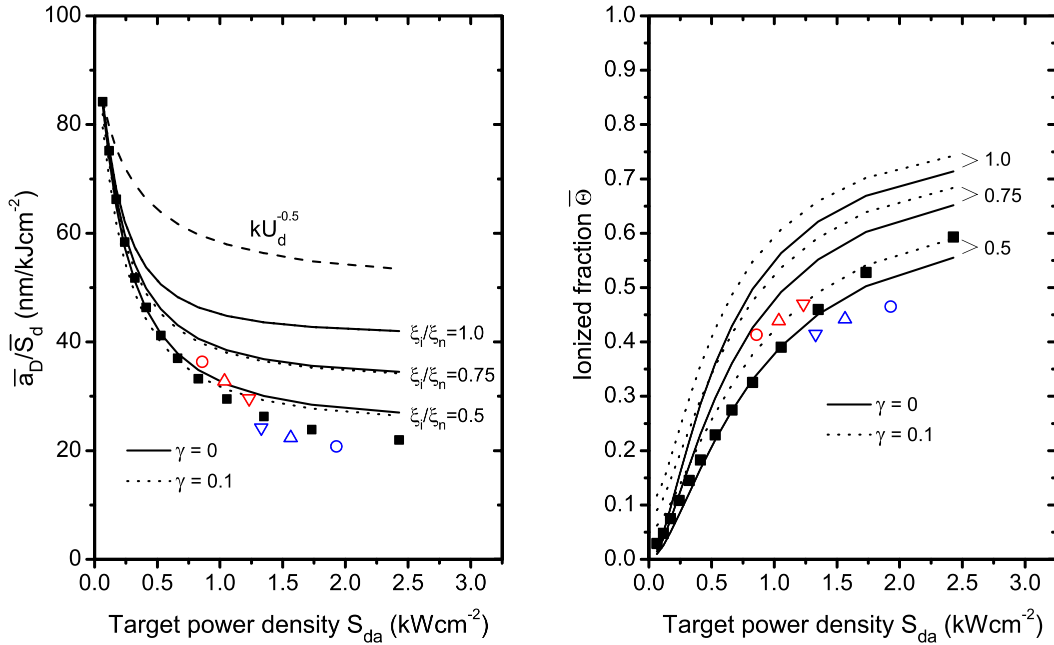

Figure 5.25: The deposition rate per average target power density in a period, $\overline{a}_D/\overline{S}_d$, and the average ionized fraction of sputtered target material atoms in the flux onto the substrate in a period, $\overline{\Theta}$, as functions of the average target power density in a pulse, S_{da}, corresponding to the U_d values ranging from 400 V to 1000 V at the magnetic field strength $B = 400$ G. The full squares are related to the calculations using the non-stationary two-zone model while the solid lines (the probability of additional ionization $\gamma = 0$) and dotted lines ($\gamma = 0.1$) are related to the calculations using the steady-state phenomenological model with the relative ion-to-atom transport factors $\xi_i/\xi_n = 0.5$, 0.75 and 1.0. For comparison, the dashed line represents the values predicted by the relation $\overline{a}_D/\overline{S}_d = kU_d^{-0.5}$, where k is a constant. Moreover, the results obtained using the non-stationary two-zone model for $U_d = 1000$ V (red open symbols) at $B = 150$ G (◯), 200 G (△) and 250 G (▽), and for $U_d = 800$ V (blue open symbols) at $B = 600$ G (▽), 650 G (△) and 700 G (◯) are also presented.

$\overline{a}_D/\overline{S}_d$ and the ionized fraction $\overline{\Theta}$ enable us to explain the effects of various individual processes on these deposition characteristics. Based on the results, we recommend to lower the magnetic field strength in a magnetron system at a fixed average target power density in a pulse (using a higher magnetron voltage) in order to enhance the deposition rate and keep or even increase the ionized fraction $\overline{\Theta}$.

6 Conclusions

All particular aims of the thesis were fulfilled.

We developed a non-stationary two-zone model for high-power impulse magnetron sputtering discharges. The model is based on a global description of plasma in the typical geometry of the magnetron discharges and it includes all the processes relevant for HiPIMS in a simplified manner. It makes it possible to calculate time evolutions of the averaged densities of the plasma species, their fluxes towards the target, substrate and chamber walls and the electron temperatures. As a consequence, it is able to evaluate complex discharge and deposition characteristics, such as the fraction of the target material ions in the total ions flux onto the target, the ionized fraction of the sputtered target material atoms in the flux onto the substrate and the deposition rate.

The model results were compared with experimental data for three different HiPIMS systems with a copper target. It was found that the target current is very sensitive to the secondary electron emission coefficients and to the secondary electron recapture coefficient. With a proper choice of these parameters, the calculated target currents are in a good agreement with experimental results and their trends with an increasing target voltage and process gas pressure are correctly reproduced (Pajdarová et al., 2009; Gudmundsson et al., 2009; Anders et al., 2007). The calculated electron densities and electron temperatures are in good agreement with experimental results for two different systems (Pajdarová et al., 2009; Gudmundsson et al., 2009). However, with the current model we were not able to reproduce exactly the target current–voltage characteristics around the threshold for runaway to a high-current discharge which is observed in the results of Anders et al. (2007).

The model was used to study general relations between the process input parameters and the important discharge and deposition characteristics. The results helps us understand the complicated behaviour of these discharges and can be used to optimize the process input parameters with respect to desired applications. The main conclusions can be summarized in the following points.

1. With an increasing target power density in a pulse, the plasma density in front of the target reaches up to $10^{20}\,\mathrm{m}^{-3}$ for average target power densities on the order of kWcm^{-2} and the plasma becomes gradually more metal-dominant and the flux of sputtered atoms onto the substrate is more ionized. However, with the presence of the process gas, the ion flux onto the target is always composed of both ions. In the case investigated, the average fraction of copper ions in the total ion flux onto the target was 66 % and 92 % for the average target power

density of 500 Wcm^{-2} and 3 $kWcm^{-2}$ in a pulse, respectively. The maximum average ionized fraction of copper atoms in the flux onto the substrate was 80 % at the target power density of 3 $kWcm^{-2}$ in a pulse.

2. Sufficiently long pulses (at least 100 μs), which allow for the build-up of a high density plasma in front of the target, are necessary to achieve high target power densities in a pulse and, consequently, high degrees of ionization of the sputtered copper atoms. An increased magnetic field strength in front of the target also promotes a higher target power density at a fixed target voltage. Higher repetition frequencies of pulses lead also to higher target power densities, but this effect is relevant only for short pulses (less than 50 μs).

3. The average target power density in a pulse is, besides the target voltage, a fundamental quantity determining the average ionized fraction of target material atoms in the flux onto the substrate and the normalized deposition rate. There is a correlation between an increase in the degree of ionization of the sputtered atoms and a decrease of the normalized deposition rate. In the case investigated, the normalized deposition rate decreased 2.3 times when the target power density increased from 300 Wcm^{-2} to 1700 Wcm^{-2} in a pulse. It was shown that this decrease is mainly due to a backward flux of ionized sputtered atoms combined with higher losses of ions to chamber walls (compared to neutrals) and due to a less-than-linear increase of the sputtering yields with ion energy (in the case of a varying target voltage). This suggests that a compromise between a high degree of ionization of the sputtered target material atoms and an acceptable deposition rate should be found by tuning the average target power density delivered in a pulse.

4. The deposition characteristics can be further optimized by a change of the magnetic field. A reasonable decrease of the magnetic field strength above the target leads to a decrease in the return probability of the ionized sputtered atoms onto the target which has a positive effect on both the ionized fraction of the sputtered atoms in the flux onto the substrate and on the deposition rate.

As a next step, we aim to extend the model for high-power impulse magnetron deposition of oxides and nitrides. The reactions of oxygen and nitrogen in the plasma and on the surfaces makes the process even much more complicated. We believe that this upgrade greatly extends the applicability of the model to a wider range of industrial applications of high-power impulse magnetron sputtering.

7 Bibliography

7.1 References

Alami, J., Sarakinos, K., Mark, G. and Wuttig, M. (2006). On the deposition rate in a high power pulsed magnetron sputtering discharge, *Appl. Phys. Lett.* **89** 154104.

Anders, A. (2008). Self-sputtering runaway in high power impulse magnetron sputtering: The role of secondary electrons and multiply charged metal ions, *Appl. Phys. Lett.* **92** 201501.

Anders, A. (2010). Deposition rates of high power impulse magnetron sputtering: Physics and economics, *J. Vac. Sci. Technol. A* **28** 783.

Anders, A. (2011). Discharge physics of high power impulse magnetron sputtering, *Surf. Coat. Technol.* **205, Supplement 2** S1.

Anders, A., Andersson, J. and Ehiasarian, A. (2007). High power impulse magnetron sputtering: Current-voltage-time characteristics indicate the onset of sustained self-sputtering, *J. Appl. Phys.* **102** 113303.

Anders, A., Ni, P. and Rauch, A. (2012). Drifting localization of ionization runaway: Unraveling the nature of anomalous transport in high power impulse magnetron sputtering, *J. Appl. Phys.* **111** 053304.

Anders, A. and Oks, E. (2009). Broad, intense, quiescent beam of singly charged metal ions obtained by extraction from self-sputtering plasma far above the runaway threshold, *J. Appl. Phys.* **106** 023306.

Andersson, J. and Anders, A. (2008). Gasless sputtering: Opportunities for ultraclean metallization, coatings in space, and propulsion, *Appl. Phys. Lett.* **92** 221503.

Andersson, J. and Anders, A. (2009). Self-Sputtering Far above the Runaway Threshold: An Extraordinary Metal-Ion Generator, *Phys. Rev. Lett.* **102** 045003.

Ashida, S., Lee, C. and Lieberman, M. A. (1995). Spatially averaged (global) model of time modulated high density argon plasmas, *J. Vac. Sci. Technol. A* **13** 2498.

Behrish, R. and Eckstein, W. (2007). *Sputtering by particle bombardment*, Springer Berlin / Heidelberg.

Betz, G. and Wien, K. (1994). Energy and angular distributions of sputtered particles, *International Journal of Mass Spectrometry and Ion Processes* **140** 1.

Birdsall, C. K. and Langdon, A. B. (1991). *Plasma Physics via Computer Simulation*, The Adam Hilger Series on Plasma Physics, IOP Publishing Ltd.

Bogaerts, A., Gijbels, R. and Carman, R. J. (1998). Collisional-radiative model for the sputtered copper atoms and ions in a direct current argon glow discharge, *Spectrochim. Acta B* **53** 1679.

Bohlmark, J., Alami, J., Christou, C., Ehiasarian, A. P. and Helmersson, U. (2005). Ionization of sputtered metals in high power pulsed magnetron sputtering, *J. Vac. Sci. Technol. A* **23** 18.

Bohlmark, J., Helmersson, U., VanZeeland, M., Axnas, I., Alami, J. and Brenning, N. (2004). Measurement of the magnetic field change in a pulsed high current magnetron discharge, *Plasma Sources Sci. Technol.* **13** 654.

Bohlmark, J., Lattemann, M., Gudmundsson, J., Ehiasarian, A., Gonzalvo, Y., Brenning, N. and Helmersson, U. (2006). The ion energy distributions and ion flux composition from a high power impulse magnetron sputtering discharge, *Thin Solid Films* **515** 1522.

Bohlmark, J., Östbye, M., Lattemann, M., Ljungcrantz, H., Rosell, T. and Helmersson, U. (2006). Guiding the deposition flux in an ionized magnetron discharge, *Thin Solid Films* **515** 1928.

Bradley, J. W., Clarke, G. C. B., Braithwaite, N. S. J., Bryant, P. M. and Kelly, P. J. (2006). Time resolved 2-D optical imaging of a pulsed unbalanced magnetron plasma, *Plasma Sources Sci. Technol.* **15** S44.

Bradley, J. W., Thompson, S. and Gonzalvo, Y. A. (2001). Measurement of the plasma potential in a magnetron discharge and the prediction of the electron drift speeds, *Plasma Sources Sci. Technol.* **10** 490.

Brenning, N., Axnäs, I., Raadu, M. A., Lundin, D. and Helmerson, U. (2008). A bulk plasma model for dc and HiPIMS magnetrons, *Plasma Sources Sci. Technol.* **17** 045009.

Brenning, N., Merlino, R. L., Lundin, D., Raadu, M. A. and Helmersson, U. (2009). Faster-than-Bohm Cross-B Electron Transport in Strongly Pulsed Plasmas, *Phys. Rev. Lett.* **103** 225003.

Bretagne, J., Delouya, G. and Puech, V. (1981). High-energy electron distribution in an electron-beam-generated argon plasma, *J. Phys. D: Appl. Phys.* **14** 1225.

Bretagne, J., Godart, J. and Puech, V. (1982). Low-energy electron distribution in an electron-beam-generated argon plasma, *J. Phys. D: Appl. Phys.* **15** 2205.

Bretagne, J., Gousset, G. and Trennepohl Jr, W. (1997). Plasma-surface interaction modelling of d.c. reactive magnetron discharges, *Surf. Coat. Technol.* **97** 611.

Bultinck, E. and Bogaerts, A. (2008). The effect of the magnetic field strength on the sheath region of a dc magnetron discharge, *J. Phys. D: Appl. Phys.* **41** 202007.

Buyle, G., Bosscher, W. D., Depla, D., Eufinger, K., Haemers, J. and Gryse, R. D. (2003). Recapture of secondary electrons by the target in a DC planar magnetron discharge, *Vacuum* **70** 29.

Buyle, G., Depla, D., Eufinger, K., Haemers, J., Bosscher, W. D. and Gryse, R. D. (2004). Simplified model for the DC planar magnetron discharge, *Vacuum* **74** 353. Selected papers revised from the Proceedings of the Seventh International Symposium on Sputtering and Plasma Processes (ISSP 2003).

Callen, J. D. (2006). *Fundamentals of Plasma Physics*, online.

Capek, J., Hala, M., Zabeida, O., Klemberg-Sapieha, J. E. and Martinu, L. (2012). Deposition rate enhancement in HiPIMS at preserved ionized fraction of the deposition flux, *J. Appl. Phys.* submitted.

Chen, F. F. (1984). *Introduction to Plasma Physics and Controlled Fusion*, Plenum Pub. Corp.

Christie, D. J. (2005). Target material pathways model for high power pulsed magnetron sputtering, *J. Vac. Sci. Technol. A* **23** 330.

Costin, C., Marques, L., Popa, G. and Gousset, G. (2005). Two-dimensional fluid approach to the dc magnetron discharge, *Plasma Sources Sci. Technol.* **14** 168.

Ehiasarian, A., New, R., Münz, W.-D., Hultman, L., Helmersson, U. and Kouznetsov, V. (2002). Influence of high power densities on the composition of pulsed magnetron plasmas, *Vacuum* **65** 147. ¡ce:title¿IUVSTA Highlights Seminar¡/ce:title¿.

Ehiasarian, A. P., Hecimovic, A., de los Arcos, T., New, R., von der Gathen, V. S., Boke, M. and Winter, J. (2012). High power impulse magnetron sputtering discharges: Instabilities and plasma self-organization, *Appl. Phys. Lett.* **100** 114101.

Ehiasarian, A. P. and Vetushka, A. (2009). Magnetron configuration to enhance deposition rate in high power impulse magnetron sputtering, *SVC 52nd Annual Technical Conference Proceedings*.

Goeckner, M. J., Goree, J. A. and Jr., T. E. S. (1991). Monte Carlo simulation of ions in a magnetron plasma, *IEEE T. Plasma. Sci.* **19** 301.

Gu, L. and Lieberman, M. A. (1988). Axial distribution of optical emission in a planar magnetron discharge, *J. Vac. Sci. Technol. A* **6** 2960.

Gudmundsson, J., Alami, J. and Helmersson, U. (2002). Spatial and temporal behavior of the plasma parameters in a pulsed magnetron discharge, *Surf. Coat. Technol.* **161** 249.

Gudmundsson, J. T., Alami, J. and Helmersson, U. (2001). Evolution of the electron energy distribution and plasma parameters in a pulsed magnetron discharge, *Appl. Phys. Lett.* **78** 3427.

Gudmundsson, J. T., Brenning, N., Lundin, D. and Helmersson, U. (2012). High power impulse magnetron sputtering discharge, *J. Vac. Sci. Technol. A* **30** 030801.

Gudmundsson, J. T., Sigurjonsson, P., Larsson, P., Lundin, D. and Helmersson, U. (2009). On the electron energy in the high power impulse magnetron sputtering discharge, *J. Appl. Phys.* **105** 123302.

Guerra, V., Sá, P. A. and Loureiro, J. (2004). Kinetic modeling of low-pressure nitrogen discharges and post-discharges, *The European Physical Journal - Applied Physics* **28** 125.

Hagelaar, G. J. M. and Pitchford, L. C. (2005). Solving the Boltzmann equation to obtain electron transport coefficients and rate coefficients for fluid models, *Plasma Sources Sci. Technol.* **14** 722.

Hala, M., Viau, N., Zabeida, O., Klemberg-Sapieha, J. E. and Martinu, L. (2010). Dynamics of reactive high-power impulse magnetron sputtering discharge studied by time- and space-resolved optical emission spectroscopy and fast imaging, *J. Appl. Phys.* **107** 043305.

Hayashi, M. (2003). Bibliography of Electron and Photon Cross Sections with Atoms and Molecules Published in the 20th Century – Argon, *NIFS-DATA* **72**.

Hecimovic, A. and Ehiasarian, A. P. (2009). Time evolution of ion energies in HIPIMS of chromium plasma discharge, *J. Phys. D: Appl. Phys.* **42** 135209.

Hecimovic, A. and Ehiasarian, A. P. (2010). Spatial and temporal evolution of ion energies in high power impulse magnetron sputtering plasma discharge, *J. Appl. Phys.* **108** 063301.

Hjartarson, A. T., Thorsteinsson, E. G. and Gudmundsson, J. T. (2010). Low pressure hydrogen discharges diluted with argon explored using a global model, *Plasma Sources Sci. Technol.* **19** 065008.

Hopwood, J. (1998). Ionized physical vapor deposition of integrated circuit interconnects, *Phys. Plasmas* **5** 1624.

Horwat, D. and Anders, A. (2010). Ion acceleration and cooling in gasless self-sputtering, *Appl. Phys. Lett.* **97** 221501.

Hosokawa, N., Tsukada, T. and Kitahara, H. (1980). Effect of discharge current and sustained self-sputtering, *Proc. 8th Int. Vacuum Congress, Le Vide, Cannes, France.*

Kadlec, S. (2007). Simulation of Neutral Particle Flow During High Power Magnetron Impulse, *Plasma Processes Polym.* **4** S419.

Kelly, P. J. and Arnell, R. D. (2000). Magnetron sputtering: a review of recent developments and applications, *Vacuum* **56** 159.

Kim, S., Lieberman, M. A., Lichtenberg, A. J. and Gudmundsson, J. T. (2006). Improved volume-averaged model for steady and pulsed-power electronegative discharges, *J. Vac. Sci. Technol. A* **24** 2025.

Kolev, I. (2007). *Particle-in-cell – Monte Carlo collisions simulations for a direct current planar magnetron discharge*, PhD thesis, University of Antwerp.

Kolev, I. and Bogaerts, A. (2004). Numerical Models of the Planar Magnetron Glow Discharges, *Contrib. Plasm. Phys.* **44** 582.

Kolev, I. and Bogaerts, A. (2006). PIC – MCC Numerical Simulation of a DC Planar Magnetron, *Plasma Processes Polym.* **3** 127.

Kondo, S. and Nanbu, K. (1999). A self-consistent numerical analysis of a planar dc magnetron discharge by the particle-in-cell/Monte Carlo method, *J. Phys. D: Appl. Phys.* **32** 1142.

Konstantinidis, S., Dauchot, J. P., Ganciu, M., Ricard, A. and Hecq, M. (2006). Influence of pulse duration on the plasma characteristics in high-power pulsed magnetron discharges, *J. Appl. Phys.* **99** 013307.

Kudláček, P., Vlček, J., Burcalová, K. and Lukáš, J. (2008). Highly ionized fluxes of sputtered titanium atoms in high-power pulsed magnetron discharges, *Plasma Sources Sci. Technol.* **17** 025010.

Kushner, M. J. (2009). Hybrid modelling of low temperature plasmas for fundamental investigations and equipment design, *J. Phys. D: Appl. Phys.* **42** 194013.

Lazar, J., Vlček, J. and Rezek, J. (2010). Ion flux characteristics and efficiency of the deposition processes in high power impulse magnetron sputtering of zirconium, *J. Appl. Phys.* **108** 063307.

Levchenko, I., Keidar, M. and Ostrikov, K. (2009). Electron transport across magnetic field in low-temperature plasmas: An alternative approach for obtaining evidence of Bohm mechanism, *Phys. Lett. A* **373** 1140.

Lichtenberg, A. J. and Lieberman, M. A. (2000). Modeling a metal-vapor buffer-gas hollow cathode discharge, *J. Appl. Phys.* **87** 7191.

Lieberman, M. A. and Lichtenberg, A. J. (2005). *Principles of Plasma Discharges and Materials Processing, Second Edition*, Wiley.

Longo, S. (2000). Monte Carlo models of electron and ion transport in non-equilibrium plasmas, *Plasma Sources Sci. Technol.* **9** 468.

Lu, J. and Kushner, M. J. (2000). Effect of sputter heating in ionized metal physical vapor deposition reactors, *J. Appl. Phys.* **87** 7198.

Lundin, D., Helmersson, U., Kirkpatrick, S. K., Rohde, S. and Brenning, N. (2008). Anomalous electron transport in high power impulse magnetron sputtering, *Plasma Sources Sci. Technol.* **17** 025007.

Lundin, D., Larsson, P., Wallin, E., Lattemann, M., Brenning, N. and Helmersson, U. (2008). Cross-field ion transport during high power impulse magnetron sputtering, *Plasma Sources Sci. Technol.* **17** 035021.

Lundin, D. and Sarakinos, K. (2012). An introduction to thin film processing using high-power impulse magnetron sputtering, *J. Mater. Res.* **27** 780.

Martines, E., Zuin, M., Antoni, V., Cavazzana, R., Serianni, G., Spolaore, M. and Nakashima, C. (2004). Experimental investigation of low-frequency waves propagating in a direct current planar magnetron plasma, *Phys. Plasmas* **11** 1938.

Matyash, K., Schneider, R., Taccogna, F., Hatayama, A., Longo, S., Capitelli, M., Tskhakaya, D. and Bronold, F. X. (2007). Particle in Cell Simulation of Low Temperature Laboratory Plasmas, *Contrib. Plasm. Phys.* **47** 595.

Miranda, J. E., Goeckner, M. J., Goree, J. and Sheridan, T. E. (1990). Monte Carlo simulation of ionization in a magnetron plasma, *J. Vac. Sci. Technol. A* **8** 1627.

Mishra, A., Kelly, P. J. and Bradley, J. W. (2010). The evolution of the plasma potential in a HiPIMS discharge and its relationship to deposition rate, *Plasma Sources Sci. Technol.* **19** 045014.

Mishra, A., Kelly, P. J. and Bradley, J. W. (2011). The 2D plasma potential distribution in a HiPIMS discharge, *J. Phys. D: Appl. Phys.* **44** 425201.

Musil, J. (1998). Low-pressure magnetron sputtering, *Vacuum* **50** 363.

Musschoot, J., Depla, D., Buyle, G., Haemers, J. and Gryse, R. D. (2008). Investigation of the sustaining mechanisms of dc magnetron discharges and consequences for I-V characteristics, *J. Phys. D: Appl. Phys.* **41** 015209.

Olsson, M. K. and Macák, K. (2000). Mechanisms for reactive DC magnetron sputtering of elements with different atomic masses: large area coatings of Al oxide and W oxide, *Thin Solid Films* **371** 86.

Pajdarová, A. D., Vlček, J., Kudláček, P. and Lukáš, J. (2009). Electron energy distributions and plasma parameters in high-power pulsed magnetron sputtering discharges, *Plasma Sources Sci. Technol.* **18** 025008.

Petrov, P. K., Volpyas, V. A. and Chakalov, R. A. (1999). Three-dimensional Monte Carlo simulation of sputtered atom transport in the process of ion-plasma sputter deposition of multicomponent thin films, *Vacuum* **52** 427.

Phelps, A. V. (1991). Cross Sections and Swarm Coefficients for Nitrogen Ions and Neutrals in N[sub 2] and Argon Ions and Neutrals in Ar for Energies from 0.1 eV to 10 keV, *J. Phys. Chem. Ref. Data* **20** 557.

Phelps, A. V. and Petrovic, Z. L. (1999). Cold-cathode discharges and breakdown in argon: surface and gas phase production of secondary electrons, *Plasma Sources Sci. Technol.* **8** R21.

Poolcharuansin, P. and Bradley, J. W. (2010). Short- and long-term plasma phenomena in a HiPIMS discharge, *Plasma Sources Sci. Technol.* **19** 025010.

Poolcharuansin, P., Liebig, B. and Bradley, J. W. (2012). More evidence for azimuthal ion spin in HiPIMS discharges, *Plasma Sources Sci. Technol.* **21** 015001.

Porokhova, I. A., Golubovskii, Y. B., Bretagne, J., Tichy, M. and Behnke, J. F. (2001). Kinetic simulation model of magnetron discharges, *Phys. Rev. E* **63** 056408.

Posadowski, W. (1995). Sustained self sputtering of different materials using dc magnetron, *Vacuum* **46** 1017.

Rauch, A., Mendelsberg, R. J., Sanders, J. M. and Anders, A. (2012). Plasma potential mapping of high power impulse magnetron sputtering discharges, *J. Appl. Phys.* **111** 083302.

Riemann, K. U. (1991). The Bohm criterion and sheath formation, *J. Phys. D: Appl. Phys.* **24** 493.

Riemann, K.-U. (1995). The Bohm criterion and boundary conditions for a multicomponent system, *Plasma Science, IEEE Transactions on* **23** 709.

Rossnagel, S. M. and Kaufman, H. R. (1987). Induced drift currents in circular planar magnetrons, *J. Vac. Sci. Technol. A* **5** 88.

Samuelsson, M., Lundin, D., Jensen, J., Raadu, M. A., Gudmundsson, J. T. and Helmersson, U. (2010). On the film density using high power impulse magnetron sputtering, *Surf. Coat. Technol.* **205** 591.

Samukawa, S., Hori, M., Rauf, S., Tachibana, K., Bruggeman, P., Kroesen, G., Whitehead, J. C., Murphy, A. B., Gutsol, A. F., Starikovskaia, S., Kortshagen, U., Boeuf, J.-P., Sommerer, T. J., Kushner, M. J., Czarnetzki, U. and Mason, N. (2012). The 2012 Plasma Roadmap, *J. Phys. D: Appl. Phys.* **45** 253001.

Sarakinos, K., Alami, J. and Konstantinidis, S. (2010). High power pulsed magnetron sputtering: A review on scientific and engineering state of the art, *Surf. Coat. Technol.* **204** 1661.

Sheridan, T. E., Goeckner, M. J. and Goree, J. (1990). Model of energetic electron transport in magnetron discharges, *J. Vac. Sci. Technol. A* **8** 30.

Shidoji, E. and Makabe, T. (2003). Magnetron plasma structure with strong magnetic field, *Thin Solid Films* **442** 27. Selected papers from the 4th International Conference on Coatings on Glass.

Shidoji, E., Nakano, N. and Makabe, T. (1999). Numerical simulation of the discharge in d.c. magnetron sputtering, *Thin Solid Films* **351** 37.

Smirnov, B. M. (2000). Tables for Cross Sections of the Resonant Charge Exchange Process, *Phys. Scr.* **61** 595.

Sobbia, R., Browning, P. K. and Bradley, J. W. (2008). Numerical investigation via three-dimensional Monte Carlo modeling of sputtering and deposition processes in a direct current unbalanced magnetron discharge, *J. Vac. Sci. Technol. A* **26** 103.

Thorsteinsson, E. G. and Gudmundsson, J. T. (2010). A global (volume averaged) model of a chlorine discharge, *Plasma Sources Sci. Technol.* **19** 015001.

Trajmar, S., Williams, W. and Srivastava, S. K. (1977). Electron-impact cross sections for Cu atoms, *Journal of Physics B: Atomic and Molecular Physics* **10** 3323.

van der Straaten, T. A., Cramer, N. F., Falconer, I. S. and James, B. W. (1998). The cylindrical DC magnetron discharge: I. Particle-in-cell simulation, *J. Phys. D: Appl. Phys.* **31** 177.

Vasenkov, A. V. and Shizgal, B. D. (2002). Numerical study of a direct current plasma sheath based on kinetic theory, *Phys. Plasmas* **9** 691.

Vetushka, A. and Ehiasarian, A. P. (2008). Plasma dynamic in chromium and titanium HIPIMS discharges, *J. Phys. D: Appl. Phys.* **41** 015204.

Vlček, J. and Burcalová, K. (2010). A phenomenological equilibrium model applicable to high-power pulsed magnetron sputtering, *Plasma Sources Sci. Technol.* **19** 065010.

Vlček, J., Kudláček, P., Burcalová, K. and Musil, J. (2007a). High-power pulsed sputtering using a magnetron with enhanced plasma confinement, *J. Vac. Sci. Technol. A* **25** 42.

Vlček, J., Kudláček, P., Burcalová, K. and Musil, J. (2007b). Ion flux characteristics in high-power pulsed magnetron sputtering discharges, *Europhys. Lett.* **77** 45002.

Vlček, J., Pajdarová, A. D. and Musil, J. (2004). Pulsed dc Magnetron Discharges and their Utilization in Plasma Surface Engineering, *Contrib. Plasm. Phys.* **44** 426.

Warner, B. E., Persson, K. B. and Collins, G. J. (1979). Metal-vapor production by sputtering in a hollow-cathode discharge: Theory and experiment, *J. Appl. Phys.* **50** 5694.

Ziegler, J. F., Ziegler, M. D. and Biersack, J. P. (2008). SRIM - The stopping and range of ions in matter (computer program), available from http://www.srim.org.

7.2 Publications of the candidate

Refereed journal papers

[I] Kozák, T. and Pajdarová, A.D. A non-stationary model for high power impulse magnetron sputtering discharges, *J. Appl. Phys.* **110** 103303 (2011).

[II] Kozák, T. Effect of the target power density on high-power impulse magnetron sputtering of copper, *Plasma Sources Sci. Technol.* **21** 025012 (2012).

[III] Kozák, T. and Vlček, J. Effect of the voltage pulse characteristics on high-power impulse magnetron sputtering of copper, accepted by *Plasma Sources Sci. Technol.* (2012).

[IV] Kozák, T., Vlček, J. and Kos, Š. Transport and ionization of sputtered atoms in high-power impulse magnetron sputtering discharges, submitted to *J. Phys. D: Appl. Phys.* (2012).

Conference papers

[V] Kozák, T. and Pajdarová, A.D. A two-zone model for high power pulsed magnetron sputtering discharges (poster), *12th International Conference on Plasma Surface Engineering*, September 11–17, 2010, Garmisch-Partenkirchen, Germany.

[VI] Baroch, P., Kozák, T. and Musil, J. Effect of substrate material on surface morphology of thin films prepared by nonreactive magnetron sputtering (poster), *12th International Conference on Plasma Surface Engineering*, September 11–17, 2010, Garmisch-Partenkirchen, Germany.

[VII] Kozák, T. and Pajdarová, A.D. A two-zone model for high power pulsed magnetron sputtering discharges (oral), *38th International Conference on Metallurgical Coatings and Thin Films*, May 2–6, 2011, San Diego, California.

[VIII] Kozák, T. and Pajdarová, A.D. A non-stationary model for high power pulsed magnetron sputtering discharges (oral), *Second International Conference on Fundamentals and Industrial Application of HIPIMS*, June 28–29, 2011, Braunschweig, Germany.

[IX] Vlček, J. and Kozák, T. Modeling of high power impulse magnetron sputtering (oral), *10th International Conference on Reactive Sputter Deposition*, December 7–9, 2011, Linkoeping, Sweden.

[X] Kozák, T. Effect of the target power density on high-power impulse magnetron sputtering of copper (oral), *10th International Conference on Reactive Sputter Deposition*, December 7–9, 2011, Linkoeping, Sweden.

[XI] Kozák, T. Modeling of high power impulse magnetron sputtering of copper (oral, Student Sponsorship Award), *SVC TechCon 2012*, April 28 – May 3, 2012, Santa Clara, California.

[XII] Kozák, T. Understanding the deposition characteristics of high-power impulse magnetron sputtering discharges from quantitative modelling studies (oral), *11th International Conference on Reactive Sputter Deposition*, December 13–14, 2012, Gent, Belgium.

7.3 Abstract

Vysokovýkonové pulzní magnetronové naprašování (HiPIMS) je novým technologickým procesem, který v několika směrech překonává konvenční magnetronové naprašování. Hlavním cílem této práce je vývoj nestacionárního modelu tohoto depozičního procesu a jeho detailní objasnění.

Uvedený model vychází z existujících globálních modelů plazmatu. Umožňuje konzistentní a rychlý výpočet výbojových a depozičních charakteristik při různých procesních podmínkách. Oproti dřívějším globálním modelům přináší několik inovací: (1) rozdělení simulovaného objemu do dvou zón, (2) zahrnutí rychlých (sekundárních) elektronů a rychlých atomů rozprášených z terče, (3) zavedení a výpočet potenciálu plazmatu v magnetickém poli před terčem magnetronu a (4) nezávislý výpočet výbojového proudu.

Porovnání výsledků modelu s experimenty dává dobrou shodu, vezmeme-li v úvahu prostorová zjednodušení zahrnutá v modelu. Ukazuje se, že vývoj vysokovýkonového magnetronového výboje během pulzu je obzvláště citlivý na parametry určující sekundární emisi elektronů z terče.

Model je použit k výpočtu složení plazmatu v pulzním výboji s měděným terčem při rostoucí hustotě výkonu na terči. Bylo určeno, že dochází k postupnému přechodu k plazmatu dominovanému rozprášeným materiálem. Pro nejvyšší hustotu výkonu 3 kWcm^{-2} v pulzu představují ionty Cu^{+} 93 % iontů v celkovém toku iontů na terč a 80 % v celkovém toku částic mědi na substrát.

Analýza vlivu délky pulzu ukazuje, že k dosažení vysoké výkonové hustoty na terči a následně i vysokého stupně ionizace atomů rozprášeného materiálu ve výboji je potřeba použít dostatečně dlouhé pulzy (alespoň 100 μs). Modelové výpočty ukazují na korelaci mezi stupněm ionizace atomů rozprášeného materiálu a depoziční rychlostí vztaženou ke střednímu výkonu dodanému v širokém rozsahu vstupních podmínek. Je evidentní, že pokles depoziční rychlosti vztažené ke střednímu výkonu závisí na středním výkonu dodaném do výboje během pulzu. Tento pokles je způsoben zejména návratem iontů rozprášeného materiálu zpět na terč, jejich vyššími ztrátami ke stěnám komory (v porovnání s neutrálními atomy) a pomalejší než lineární závislostí rozprašovacího výtěžku materiálu terče na kinetické energii iontů bombardujících terč.

High-power impulse magnetron sputtering (HiPIMS) is a recent development of the well-established magnetron sputtering technique. The main aim of this thesis is to develop a non-stationary model of this process and to explain their details.

The presented model is based on a global description of plasma which allows for self-consistent and very fast calculations of the discharge and deposition characteristics under various process conditions. The new features of this model with respect to previous global plasma models are (1) the division of the simulated volume into two zones, (2) an incorporation of fast (secondary) electrons and fast sputtered target material atoms, (3) an introduction of a calculated potential drop (magnetic presheath) near the target and (4) a self-consistent calculation of the target current.

The comparison of the model results with experiments shows a good agreement, taking into account the spatial approximations of the model. It was found that the evolution of a HiPIMS discharge during a pulse is sensitive particularly to the parameters determining the secondary electron emission from the target.

The model is used to calculate the composition of the discharge plasma for HiPIMS of copper with an increasing target power density, showing a gradual transition to a metal dominated discharge with an increasing degree of ionization of the sputtered material atoms. For the highest target power density of $3\,\mathrm{kWcm^{-2}}$, we obtained in average $93\,\%$ of copper ions in the total ion flux onto the target and $80\,\%$ of copper ions in the total flux of copper particles onto the substrate.

The analysis of the effect of the voltage pulse length shows that sufficiently long pulses (at least $100\,\mu\mathrm{s}$) are needed to obtain high target power densities in a pulse and, consequently, high degree of ionization of the sputtered target material atoms. Furthermore, we show a correlation between the degrees of ionization of the target material atoms and the deposition rate per average target power density in a period for a wide range of process conditions. From the model results it is evident that the decrease of the deposition rate per average target power density in a pulse depends fundamentally on the target power density delivered into the pulse. This is mainly due to a backward flux of ionized sputtered atoms combined with higher losses of ions to chamber walls (compared to neutrals) and a less-than-linear increase of the sputtering yields of the target material with ion energy.